

MODELING MONOSTATIC SEA CLUTTER AT LOW GRAZING ANGLES  
BY USING METHOD OF MOMENTS

A THESIS SUBMITTED TO  
THE GRADUATE SCHOOL OF NATURAL AND APPLIED SCIENCES  
OF  
MIDDLE EAST TECHNICAL UNIVERSITY

BY

EMRE ÖZBAŞ

IN PARTIAL FULFILLMENT OF THE REQUIREMENTS  
FOR  
THE DEGREE OF MASTER OF SCIENCE  
IN  
ELECTRICAL AND ELECTRONIC ENGINEERING

FEBRUARY 2021



Approval of the thesis:

**MODELING MONOSTATIC SEA CLUTTER AT LOW GRAZING  
ANGLES BY USING METHOD OF MOMENTS**

submitted by **EMRE ÖZBAŞ** in partial fulfillment of the requirements for the degree  
of **Master of Science in Electrical and Electronic Engineering, Middle East  
Technical University** by,

Prof. Dr. Halil Kalıpçılar  
Dean, Graduate School of **Natural and Applied Sciences** \_\_\_\_\_

Prof. Dr. İlkey Ulusoy  
Head of the Department, **Electrical and Electronics Eng.** \_\_\_\_\_

Prof. Dr. Mustafa Kuzuoğlu  
Supervisor, **Electrical and Electronics Engineering, METU** \_\_\_\_\_

**Examining Committee Members:**

Prof. Dr. Gönül Turhan Sayan  
**Electrical and Electronics Engineering, METU** \_\_\_\_\_

Prof. Dr. Mustafa Kuzuoğlu  
**Electrical and Electronics Engineering, METU** \_\_\_\_\_

Prof. Dr. Gülbin Dural Ünver  
**Electrical and Electronics Engineering, METU** \_\_\_\_\_

Prof. Dr. Özlem Özgün  
**Electrical and Electronics Eng., Hacettepe University** \_\_\_\_\_

Prof. Dr. Asım Egemen Yılmaz  
**Electrical and Electronics Engineering, Ankara University** \_\_\_\_\_

Date: 15.02.2021

**I hereby declare that all information in this document has been obtained and presented in accordance with academic rules and ethical conduct. I also declare that, as required by these rules and conduct, I have fully cited and referenced all material and results that are not original to this work.**

Name, Last name : Emre Özbaş

Signature :

## **ABSTRACT**

### **MODELING MONOSTATIC SEA CLUTTER AT LOW GRAZING ANGLES BY USING METHOD OF MOMENTS**

Özbaş, Emre  
Master of Science, Electrical and Electronic Engineering  
Supervisor: Prof. Dr. Mustafa Kuzuoğlu

February 2021, 106 pages

Scattering of electromagnetic waves from rough surfaces such as sea surface is an important problem for radar engineers, since a radar device should discriminate returns from the desired object (target) from those scattered by the undesired object, which is rough sea surface studied in this work. Since the sea surface is randomly changing with time for varying wind speeds, sea clutter problem becomes a stochastic problem. The main goal of this thesis is obtaining a model to calculate the backscattered power from rough sea surfaces at different environmental conditions for different radar parameters by using the Method of Moments (MoM) and Monte Carlo method. In the Monte Carlo approach, a set of randomly generated two-dimensional sea surfaces from two types of sea surface spectrums are used. Then, backscatter power calculations are obtained for each sea surface to calculate statistical results. Finally, by using the results obtained from this model, a comparative analysis with the empirical and statistical models in literature is carried out. It is concluded that an accurate and flexible sea clutter model for amplitude characterization is obtained which has a good agreement with the existing models.

Keywords: Sea clutter, Method of Moments, Monte Carlo Method, Radar Cross Section, NRL model, Weibull Distribution

## ÖZ

### MOMENT METHODUNU KULLANARAK DÜŞÜK SİYİRMA AÇILARINDA DENİZ KARGAŞASI BENZETİMİ

Özbaş, Emre  
Yüksek Lisans, Elektrik ve Elektronik Mühendisliği  
Tez Yöneticisi: Prof. Dr. Mustafa Kuzuoğlu

Şubat 2021, 106 sayfa

Bu çalışmada araştırılan deniz yüzeyi gibi pürüzlü yüzeylerden geri yansıyan elektromanyetik dalgalar radar mühendisleri için hedef cismi, istenmeyen cisimlerden ayırmak konusunda büyük problemler yaratabilmektedir. Pürüzlü deniz yüzeyinin farklı rüzgâr hızları için zamanla birlikte sürekli ve rastgele olarak değişmesi, problemi olasılıksal bir problem haline getirmektedir. Bu sebeple, bu tezin amacı Moment Metodu ve Monte Carlo metodunu kullanarak farklı çevre koşulları ve farklı radar parametreleri için yüksek doğrulukta bir deniz kargaşası benzetimi sunmaktır. Monte Carlo yaklaşımında bir dizi rastgele iki boyutlu deniz yüzeyi iki farklı deniz yüzeyi tayfı kullanılarak oluşturulmuştur. Daha sonra oluşan deniz yüzeylerinden geri yansıyan elektromanyetik dalgaların gücü Moment Metodu kullanılarak her bir deniz yüzeyi için ayrı ayrı hesaplanıp, sonuçlar literatürde bulunan benzetimlerle karşılaştırılmıştır. Sonuç olarak esnek ve yüksek başarımlı bir model elde edilmiş olup, tezde verilen diğer modellerle uyumluluğu doğrulanmıştır.

Anahtar Kelimeler: Deniz Kargaşası, Moment Metodu, Monte Carlo Metodu,  
Radar Kesit Alanı, NRL benzetimi, Weibull Dağıtımı

To my family and the love of my life

## ACKNOWLEDGMENTS

I would like to express my deepest gratitude to my supervisor Prof. Dr. Mustafa Kuzuođlu for his guidance, advice, criticism, encouragements, and insight throughout the research.

I would also thank my colleagues Hakan Korkmaz, Göl Yesa Altun, Tolunay Aydın, and Burak Söker for their comments, and technical suggestions.

In addition, I would like to thank my parents who are Mehmet Özbaş, Güzide Özbaş, and Enver Özbaş for their wise counsel, support, and love.

Finally, I could not have completed this thesis without the support of my love Gizem Yardımcı who provided stimulating discussions as well as happy distractions to rest my mind outside of my research.

## TABLE OF CONTENTS

ABSTRACT.....	v
ÖZ.....	vi
ACKNOWLEDGMENTS.....	viii
TABLE OF CONTENTS.....	ix
LIST OF TABLES .....	xiii
LIST OF FIGURES .....	xiv
LIST OF ABBREVIATIONS .....	xviii
CHAPTERS	
1 INTRODUCTION .....	1
1.1 A Brief Introduction to Radar.....	5
1.2 Radar clutter.....	8
1.2.1 Sea Clutter.....	8
2 1D SEA SURFACE GENERATION.....	13
2.1 Basic concepts about sea surface generation .....	13
2.2 Sea surface generation .....	16
2.2.1 Pierson Moskowitz Spectrum.....	18
2.2.2 Elfouhaily Spectrum.....	20
2.2.3 Examples of randomly generated sea surfaces by using Pierson Moskowitz and Elfouhaily Spectrum .....	24
3 Method of Moments.....	27
3.1 Maxwell's Equations .....	28
3.2 Electromagnetic Boundary Conditions.....	29
3.3 Reduced Wave Equations.....	30

3.4	Auxiliary Potentials.....	31
3.5	Surface Integral Equations.....	33
3.5.1	Transverse Magnetic Electric Field Integral Equation (TM-EFIE) ..	35
3.5.2	Transverse Electric Magnetic Field Integral Equation (TE-MFIE) ..	37
3.6	Method of Moments .....	39
3.6.1	Pulse basis function.....	41
3.6.2	Point Matching.....	42
3.7	Solutions of surface integral equations by using Method of Moments....	43
3.7.1	MoM solution of TM-EFIE and Postprocessing.....	44
3.7.2	MoM solution of TE-MFIE and Postprocessing.....	48
3.8	Incident Field Tapering.....	51
4	EMPIRICAL AND STATISTICAL SEA CLUTTER MODELS .....	53
4.1	Empirical Sea Clutter Models .....	53
4.1.1	GIT Model.....	55
4.1.2	The Hybrid Model.....	56
4.1.3	The TSC Model.....	57
4.1.4	The NRL Model.....	58
4.1.5	Modified NRL Model.....	60
4.2	Statistical Sea Clutter Models .....	61
4.2.1	Rayleigh distribution .....	62
4.2.2	Log-Normal Distribution .....	63
4.2.3	Weibull Distribution.....	63
5	PROPOSED SEA CLUTTER MODEL AND SIMULATION RESULTS....	65
5.1	Simulation results for <b>TMz</b> case with ensemble sampling .....	67

5.1.1	<b><i>TMz</i></b> case simulation results for the mean amplitude of sea clutter with ensemble sampling .....	68
5.1.2	<b><i>TMz</i></b> case simulation results for amplitude distribution of sea clutter with ensemble sampling .....	71
5.2	Simulation results for <b><i>TMz</i></b> case with space sampling .....	74
5.2.1	<b><i>TMz</i></b> case simulation results for the mean amplitude of sea clutter with space sampling .....	74
5.2.2	<b><i>TMz</i></b> case simulation results for amplitude distribution of sea clutter with space sampling .....	76
5.3	Simulation results for <b><i>TEz</i></b> case with ensemble sampling .....	79
5.3.1	<b><i>TEz</i></b> case simulation results for the mean amplitude of sea clutter with ensemble sampling .....	80
5.3.2	<b><i>TEz</i></b> case simulation results for amplitude distribution of sea clutter with ensemble sampling .....	83
5.4	Simulation results for <b><i>TEz</i></b> case with space sampling .....	87
5.4.1	<b><i>TEz</i></b> case simulation results for the mean amplitude of sea clutter with space sampling .....	87
5.4.2	<b><i>TEz</i></b> case simulation results for amplitude distribution of sea clutter with space sampling .....	89
6	CONCLUSIONS .....	93
6.1	Future Work .....	95
	REFERENCES .....	97
	APPENDICES .....	101
A.	Discrete Fourier Transform Theory .....	101
B.	Vector Identities .....	103

C.	Two-Dimensional Green's Functions .....	105
----	---	-----

## LIST OF TABLES

### TABLES

Table 2.1 Douglas Sea State [23].....	15
Table 2.2 WMO sea state.....	15
Table 4.1 NRCS in dB for 500MHz (UHF) from Nathanson Tables .....	54
Table 4.2 Parameters for the NRL clutter model .....	59
Table 4.3 Comparison of Models for 0.3° grazing angle.....	59
Table 4.4 Parameters for the Modified NRL clutter model .....	60
Table 4.5 Comparison of Models for 10° grazing angle .....	60

## LIST OF FIGURES

### FIGURES

Figure 1.1. Monostatic Radar Block Diagram.....	6
Figure 1.2. RCS of some common objects [21].....	7
Figure 1.3. Clutter Illuminated Patch Size [23].....	9
Figure 1.4. NRCS vs Grazing angle graph for I band and 15kn wind speed [12] ..	10
Figure 2.1. Pierson Moskowitz spectrum versus spatial frequency for wind speeds from 10m/s up to 20 m/s with 2m/s increments.....	19
Figure 2.2. Elfouhaily Model High Frequency and Low Frequency Curvature Spectrum for Sea States 1 to 7 .....	23
Figure 2.3. Elfouhaily spectrum versus spatial frequency for Sea States 1 to 7 .....	23
Figure 2.4. Single Surface Realization by using PM spectrum at Sea State 5.....	25
Figure 2.5. Single Surface Realization by using Elfouhaily spectrum at Sea State 5 .....	25
Figure 3.1. Interface between two media with different electrical parameters.....	29
Figure 3.2. PEC Scatterer illuminated by an incident wave .....	33
Figure 3.3. Surface Equivalence Principle .....	34
Figure 3.4. $TM_z$ case sea surface scattering.....	36
Figure 3.5. $TE_z$ case sea surface scattering.....	37
Figure 3.6. Pulse Basis Function .....	42
Figure 3.7. Point Matching Function .....	42
Figure 3.8. Sea surface domain discretization .....	43
Figure 3.9. Representation of 3-Point Simpson's rule on sea surface .....	46
Figure 3.10. The geometry and the fields along the scattering surface.....	49
Figure 3.11. Illustration of incident field tapering .....	52
Figure 4.1. NRCS vs. Grazing angle graph for $TE_z$ polarization at 100MHz.....	61
Figure 4.2. NRCS vs. Grazing angle graph for $TM_z$ polarization at 100MHz.....	61
Figure 5.1. Algorithm of the proposed model .....	65

Figure 5.2. <i>TMz</i> case mean NRCS vs. grazing angle graph for 500MHz, 60 meters length and sea states 1,3 and 5 by using Elfouhaily spectrum with Ensemble sampling .....	68
Figure 5.3. <i>TMz</i> case mean NRCS vs. grazing angle graphs of simulation results, the modified NRL model and Nathanson's Table for 500 MHz, 60 meter length, Sea State 2 by using Elfouhaily spectrum with Ensemble sampling .....	69
Figure 5.4. <i>TMz</i> case mean NRCS vs. Grazing angle graph for 100MHz, 300MHz and 500MHz at Sea State 4 by using Elfouhaily spectrum with Ensemble sampling .....	69
Figure 5.5 <i>TMz</i> case mean NRCS vs. grazing angle graph for Sea State 5 by using Pierson-Moskowitz spectrum and Elfouhaily spectrum with Ensemble sampling .	70
Figure 5.6. <i>TMz</i> case Elfouhaily spectrum Histograms and Weibull distributions of NRCS at 500MHz for Sea State 1 with Ensemble sampling .....	71
Figure 5.7. <i>TMz</i> case Elfouhaily spectrum Histograms and Weibull distributions of NRCS at 500MHz for Sea State 6 with Ensemble sampling .....	72
Figure 5.8. <i>TMz</i> case Elfouhaily spectrum Histograms and Weibull distributions of NRCS at 300MHz and 10° grazing angle for Sea States 1 to 6 with Ensemble sampling .....	73
Figure 5.9. <i>TMz</i> case PM spectrum Histograms and Log-normal distributions of NRCS at 500MHz for Sea State 6 with Ensemble sampling .....	73
Figure 5.10. <i>TMz</i> case mean NRCS vs. grazing angle graph for 500MHz, 60meter length and sea states 1,3 and 5 by using Elfouhaily spectrum with Space sampling, Ensemble sampling and the Modified NRL model.....	74
Figure 5.11. <i>TMz</i> case mean NRCS vs. grazing angle graph for Sea State 5 by using Pierson-Moskowitz spectrum and Elfouhaily spectrum with Space sampling .....	75
Figure 5.12. <i>TMz</i> case Elfouhaily spectrum Histograms and Weibull distributions of NRCS at 500MHz for Sea State 1 with Space sampling .....	76

Figure 5.13. <i>TMz</i> case Elfouhaily spectrum Histograms and Weibull and Lognormal distributions of NRCS at 500MHz for Sea State 6 with Space sampling .....	77
Figure 5.14. <i>TMz</i> case Elfouhaily spectrum Histograms and Weibull distributions of NRCS at 300MHz and 10° grazing angle for Sea States 1 to 6 with Space sampling .....	78
Figure 5.15. <i>TMz</i> case PM spectrum Histograms and Log-normal distributions of NRCS at 500MHz for Sea State 6 with Space sampling .....	79
Figure 5.16. <i>TEz</i> case and <i>TMz</i> case mean NRCS vs. grazing angle graph for 100MHz, 150 meters length and sea states 1,3 and 5 by using Elfouhaily spectrum with Ensemble sampling.....	80
Figure 5.17. <i>TEz</i> case mean NRCS vs. grazing angle graphs of simulation results, the modified NRL model and Nathanson's Table for 500MHz, 60meter length, Sea State 2 by using Elfouhaily spectrum with Ensemble sampling .....	81
Figure 5.18. <i>TEz</i> case mean NRCS vs. Grazing angle graph for 100MHz, 300MHz and 500MHz at Sea State 3 by using Elfouhaily spectrum with Ensemble sampling .....	82
Figure 5.19. <i>TEz</i> case mean NRCS vs. grazing angle graph for Sea State 5 by using Pierson-Moskowitz spectrum and Elfouhaily spectrum with Ensemble sampling.	83
Figure 5.20. <i>TEz</i> case Elfouhaily spectrum Histograms and Weibull distributions of NRCS at 500MHz for Sea State 1 with Ensemble sampling .....	84
Figure 5.21. <i>TEz</i> case Elfouhaily spectrum Histograms and Weibull distributions of NRCS at 500MHz for Sea State 6 with Ensemble sampling .....	85
Figure 5.22. <i>TEz</i> case Elfouhaily spectrum Histograms and Weibull distributions of NRCS at 300MHz and 0.3° grazing angle for Sea States 1 to 6 with Ensemble sampling .....	85
Figure 5.23. <i>TEz</i> case Pierson Moskowitz spectrum Histograms and Weibull distributions of NRCS at 500MHz for Sea State 6 with Ensemble sampling .....	86

Figure 5.24. *TEz* case mean NRCS vs. grazing angle graph for 100MHz, 150meter length and sea states 1,3 and 5 by using Elfouhaily spectrum with Space sampling and Ensemble sampling .....87

Figure 5.25. *TEz* case mean NRCS vs. grazing angle graph for Sea State 5 by using Pierson-Moskowitz spectrum and Elfouhaily spectrum with Space sampling .....88

Figure 5.26. *TEz* case Elfouhaily spectrum Histograms and Weibull distributions of NRCS at 500MHz for Sea State 1 with Space sampling .....89

Figure 5.27. *TEz* case Elfouhaily spectrum Histograms and Weibull distributions of NRCS at 500MHz for Sea State 6 with Space sampling .....90

Figure 5.28. *TEz* case Elfouhaily spectrum Histograms and Weibull distributions of NRCS at 300MHz and  $0.3^\circ$  grazing angle for Sea States 1 to 6 with Space sampling .....90

Figure 5.29. *TEz* case Pierson Moskowitz spectrum Histograms and Weibull distributions of NRCS at 500MHz for Sea State 6 with Space sampling.....91

## LIST OF ABBREVIATIONS

### ABBREVIATIONS

RADAR	Radio Detection and Ranging
RCS	Radar Cross Section
NRCS	Normalized Radar Cross Section
MoM	Method of Moments
1D	One dimensional
2D	Two dimensional
3D	Three dimensional
$TE_z$	Transverse Electric Field to z-coordinate
$TM_z$	Transverse Magnetic Field to z-coordinate
TM-EFIE	Transverse Magnetic-Electric Field Integral Equation
TE-MFIE	Transverse Electric-Magnetic Field Integral Equation
GIT	Georgia Institute of Technology
NRL	Naval Research Laboratory
TSC	Technology Service Corporation
PEC	Perfect Electrical Conductor
PM	Pierson Moskowitz
WMO	World Meteorological Organization
RMS	Root mean square
FFT/IFFT	Fast Fourier Transform/Inverse Fast Fourier Transform
PSD	Power spectral density

PDF	Probability density functions
JONSWAP	Joint North Sea Wave Project
FEM	Finite Element Method
FDM	Finite Difference Method
FDTD	Finite Difference Time Domain Method
EM	Electromagnetic
STD	Standard Deviation
SWH	Significant Wave Height



## CHAPTER 1

### INTRODUCTION

Sea clutter has been studied extensively since the development of airborne surveillance and naval radars in World War 2 [1]. For decades, modeling the backscattered electromagnetic field from rough sea surfaces has attracted the attention of researchers for many applications such as, low-altitude target detection and tracking, imaging and remote sensing, radar surveillance, etc. The main reason of accurate sea clutter modeling is to distinguish between returns (i.e., scattered field) from target object and rough sea surface and estimate the performance of the radar device. Since sea surface changes with time, understanding the nature of environmental conditions and radar principles is crucial. These topics are examined in Chapter 2.

In addition to echoes from the rough sea surface, radial motion of these surfaces creates doppler shifts in radar clutter. Therefore, sea clutter analysis is divided into two parts, which are amplitude characterization and doppler characterization. Since motion of the sea surface is a complex hydrodynamical problem, only amplitude characterization will be examined in this thesis. For the amplitude characterization, the most common figure of merit is the reflectivity of sea clutter, or Normalized Radar Cross Section (NRCS),  $\sigma_0$ . NRCS is a function of parameters like radar wavelength, grazing angle, polarization, and environmental parameters. Because many applications such as shipborne radar working on the sea surface suffers from sea clutter at low grazing angles, grazing angles from  $0.1^\circ$  to  $30^\circ$  is included in this thesis. Moreover, sea surface is assumed to be Perfect Electrical Conductor (PEC) especially for low radar frequencies and low grazing angles.

In literature there are many works, such as experimental results, empirical and statistical models dedicated to the amplitude characteristics of sea clutter at low grazing angles. Nathanson Tables [2] can be considered as a reference source among these models. These tables are extracted from various types of measurement results collected from 60 different sources and these results are averaged for specific frequencies, grazing angles, sea states and polarizations. Therefore, they are still useful for radar engineers to understand the nature of sea clutter. However, if sea clutter modeling is required for a specific case, empirical models derived from measurements may be used. In this sense, researchers have published several empirical models such as GIT Model[3], Hybrid Model[4], TSC Model[5], NRL Model[6], Modified NRL Model[7] and statistical models using Rayleigh Distribution[8], Log-normal Distribution[9], Weibull Distribution[10] to complete the lack of information in Nathanson Tables. Although empirical models provide valuable information about amplitude characterization of sea clutter, they are not valid below 100MHz.

Since monostatic sea clutter is a rough surface backscattering problem, it is also possible to find the direct solution by using Maxwell's Equations. However, EM solution of this problem, which is usually an electrically large problem, may be time consuming compared to the empirical models. Therefore, an efficient way of modeling of the rough surface scattering problem is necessary. In literature, there are many examples of analytical solutions such as the Small Perturbation Method[11], Kirchhoff approximation and Composite Model[12], and there are many numerical solutions such as Finite Element Domain Decomposition Method[13], Forward-Backward Method[14], Finite Difference Time Domain[15], Sub-Domain Decomposition Iterative Method [16] and Method of Moments[17]. Among these methods, Method of Moments is preferred because of reasons discussed in Chapter 3.

The most challenging part of numerical modeling is the computational load of the rough surface scattering problem. It is quite hard to compute 3D rough surface scattering problem even for today's computers. However, it is possible to

approximate the 3D problem by a 2D problem where any arbitrary field can be expressed as the sum of TE and TM fields. By this way, sea surface scattering problem can be expressed in two modes and this provides two scalar formulations.

Before solving the rough surface scattering problem, generation of realistic sea surfaces is required. There are many empirically obtained techniques to describe sea surfaces in the literature. The most commonly used ones are Pierson-Moskowitz Spectrum [18] and Elfouhaily spectrum [19]. Due to random nature of sea surfaces, sea clutter modeling requires statistical and stochastic techniques [20]. To achieve this, Monte Carlo method is one of the possible options to make ensemble sampling. In this method, a set of random sea surface can be generated by using sea surface generation techniques. Then, NRCS can be computed for each surface by using a numerical technique. Results are collected and represented as a random field as a function of space coordinates.[20] Collected results can be analyzed in terms of mean, variance, and histogram. Another method for sea clutter modeling is space sampling. In this case, a single sea surface is generated and divided into a set of small pieces. Then, the NRCS of each piece are computed to find the statistical properties of sea clutter.

In this thesis, a semi-empirical model is proposed to model amplitude characterization of sea clutter depending on frequency, polarization, environmental effects, and grazing angle. To achieve that, empirical sea surfaces are generated and NRCS is calculated numerically for each surface by using an Integral Equation technique which is named as the Method of Moments. Then, the results are collected and analyzed by using ensemble and space sampling techniques. Results are compared with the measurement results and statistical models in the literature. Note that, since the generated sea surfaces are empirical, the proposed model is called a semi-empirical model.

A brief outline of the thesis is given below for the sake of completeness.

In Chapter 1 basic concepts related to radar and clutter are introduced. The working principle of radar is given in Section 1.1. In Section 1.2. radar clutter and especially

sea clutter is explained. In addition, the parameter NRCS, which is the measure of sea clutter amplitude, the parameters affecting the NRCS are given.

In Chapter 2, background information required to generate realistic sea surfaces is given in Section 2.1. Moreover, environmental parameters related to sea clutter are presented in this section. Then, the method is given for 1D sea surface realizations by using PM and Elfouhaily Spectrums in Section 2.2. In addition, properties of these spectrums and sea surface examples generated with them are given.

In Chapter 3, starting with the well known Maxwell's Equations in Section 3.1, two surface integral equations, namely, TM-EFIE and TE-MFIE are derived up to the end of Section 3.5. Then, Method of Moments is described in Section 3.6 with pulse basis function and point matching. Finally, surface current densities are obtained by solving surface integral equations by using MoM and NRCS is found at the postprocessing phase from surface current densities. In addition to these solutions, incident wave tapering method is presented to get rid of abrupt changes in current densities at the edges of sea surface.

Chapter 4 is devoted to Empirical and Statistical models of sea clutter at low grazing angles in the literature. First, empirical models for average sea clutter reflectivity  $\langle\sigma_0\rangle$  and their comparisons are examined in Section 4.1. Then, the statistical distributions of NRCS and their properties are given in Section 4.2. The main purpose of this section is comparing and validating the proposed model in this work.

In Chapter 5, the algorithm running behind the proposed model is given and simulation results are presented for four main scenarios. These scenarios include two types of polarizations, two types of sea surface spectrums given in Chapter 2, and two types of sampling techniques to obtain randomly generated sea surfaces. Furthermore, the differences and similarities between these scenarios and the other models are discussed in terms of mean backscatter power and statistical distributions.

In Chapter 6, a brief conclusion has been drawn in the light of the simulation results and discussions in Chapter 5. Then, from these discussions and conclusion, future studies regarding the sea clutter modeling are listed.

## **1.1 A Brief Introduction to Radar**

RADAR (Radio Detection and Ranging) is an electromagnetic system consisting of a transmitter and a receiver. The transmitter generates a signal which is radiated as an electromagnetic wave through its antenna and the receiver detects the echoes of transmitted signal. Thus, from the received signal, information about the ambiance causing echoes can be extracted including range, velocity, and the size of the target objects.

Currently radar systems have many application areas such as Electronic Warfare, Remote Sensing, Air Traffic Control, Meteorological Monitoring, Geological Observations, Marine RADARs etc. Depending on the application area there are two types of radar structures, which are monostatic radar and bistatic radar, respectively. Main difference between these two types of radars is the location of the antennas. If the transmitter and the receiver antenna are the same or at the same location, then this type is called monostatic radar. If the receiver antenna and transmitted antenna are at two different locations, then it is called bistatic radar. In this thesis, we focus on clutter modeling for the monostatic radar.

The basic working principles of monostatic radar can be summarized as follows:

- In the waveform generator a short pulse modulated signal is generated.
- The generated signal is amplified at Power Amplifier in transmitter passed through a T/R switch or Duplexer.
- Amplified signal is transmitted through the antenna in desired directions. If it is an omni-directional antenna, signal is radiated in all directions.
- Radiated waves are intercepted by objects in the environment and scattered in all directions including the direction of receiving antenna.

- Echoes in the direction of receiving antenna are intercepted by the antenna and directed to the receiver.
- Received signal is demodulated, sampled and converted to a digital signal at the Analog to Digital Converter.
- The converted digital signal is processed using signal processing techniques and desired information is obtained.
- Then resulting information is shown on display for users.

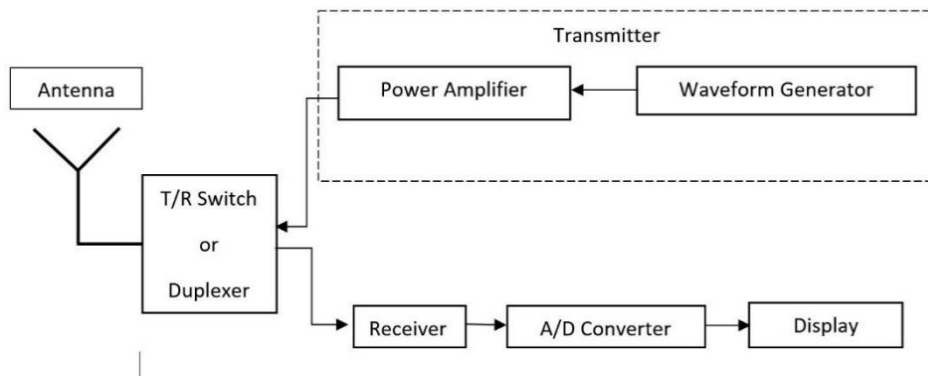


Figure 1.1. Monostatic Radar Block Diagram

Figure 1.1 shows a basic monostatic radar block diagram. Depending on the type of the application, T/R switch or Duplexer which is combination of the two filters can be used. If transmit and receiving operation must be handled at the same time Duplexer should be preferred.

Power of Radar echoes can be calculated by using a well-known formula called Radar Equation which is,

$$P_r = \frac{P_t G \sigma A_e}{(4\pi)^2 R^4} \quad (1.1)$$

where,

$P_t$ : Power transmitted from the transmitter (units of Watts)

$G$ : Gain of the antenna. It is equal to 1 for omni-directional or isotropic antennas(dimensionless)

$\sigma$ : Radar Cross Section of Radar echoes (units of area  $m^2$ )

$A_e$ : Effective Area of the Antenna (units of area  $m^2$ )

$R$ : The distance between antenna and target (units of meters)

$P_r$ : Power received at the receiver side (units of Watts)

Radar Equation can be converted to the Radar Range Equation form by using the minimum detectable signal  $S_{min}$  which is related to the modulation type of the system and required Signal to Noise Ratio of the receiver.

$$R_{max} = \left[ \frac{P_t G \sigma A_e}{(4\pi)^2 S_{min}} \right]^{\frac{1}{4}} \quad (1.2)$$

$R_{max}$  is the maximum distance which can achieved and it is one of the performance metrics of a radar application.

Moreover, the radar cross section is directly related to the size of the target object. A few RCS examples of objects is given in Figure 1.2.

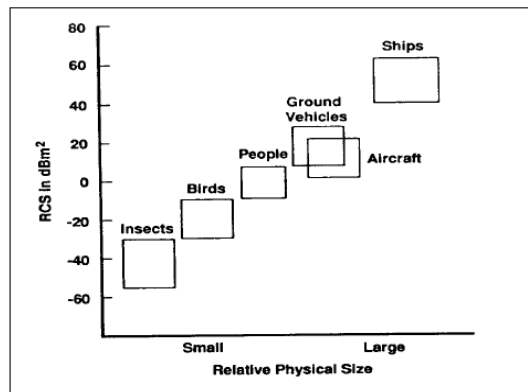


Figure 1.2. RCS of some common objects [21]

From Equation 1.1, it is seen that received power and RCS are directly proportional. RCS depends on parameters such as size, shape, material composition, polarization, frequency.

## **1.2 Radar clutter**

Clutter may be defined as any unwanted radar echo [22]. Since clutter will arise from reflections other than the targeted object, clutter causes degradation of radar performance. To differentiate radar echoes from targeted object and clutter, we need to characterize the properties of clutter.

The source of clutter can be ground, sea, rain, chaff, buildings, birds, ground traffic etc. Since the largest part of the Earth's surface is covered by sea surfaces, sea clutter is very important especially for radars located on sea vehicles over sea surfaces. In this thesis sea clutter modeling is studied extensively.

### **1.2.1 Sea Clutter**

Sea Clutter depends on Environmental Parameters, as well as Radar System Parameters. Wind strength or velocity, duration and direction of the wind can be classified as Environmental Parameters. Radar frequency or wavelength, antenna polarization, grazing angle and radar look angle can be classified as radar system parameters. Since the sea surface is dynamically changing with time and waves have velocity in certain directions, sea clutter amplitude and phase characteristics are changing with time.

Echoes from land and sea are known as surface clutter [22]. Thus, to understand the sea clutter properties, geometry of the problem should be investigated. The amplitude characterization of sea clutter can be computed by means of the radar equation as follows:

$$C = \frac{P_t G \sigma_c A_e}{(4\pi)^2 R^4} \quad (1.3)$$

where  $\sigma_c$  is the sea clutter RCS. In other words,  $\sigma_c$  can be described as the sea clutter reflectivity.

As mentioned in the radar introduction, pulse modulated signal is used for radars. Therefore, clutter illuminated patch size for low grazing angle geometries can be described in Figure 1.3. as follows

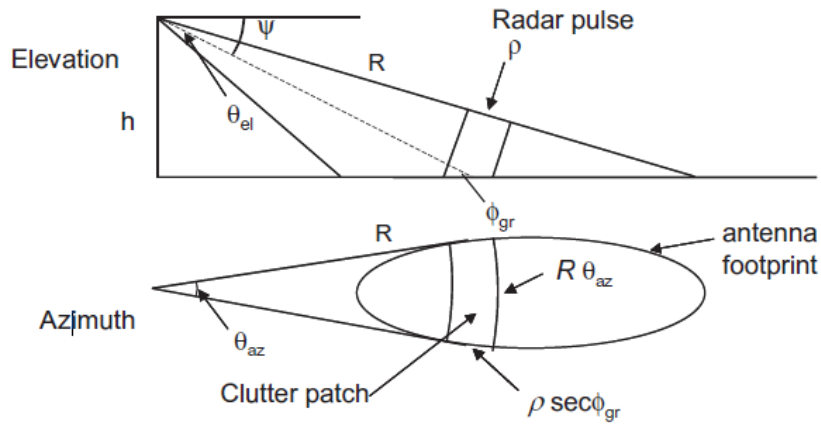


Figure 1.3. Clutter Illuminated Patch Size [23]

From Figure 1.3, clutter illuminated patch size can be computed as follows:

$$A_c = \alpha R \theta_{az} \rho \sec(\phi_{gr}) \quad (1.4)$$

where  $\theta_{az}$  antenna azimuth beamwidth,  $\phi_{gr}$  is the grazing angle which is the angle between incoming wave and surface,  $\rho$  is the range resolution which can also be represented as  $\rho = \frac{c}{2B}$  where  $c$  is the velocity of light and  $B$  is the radar pulse bandwidth, and  $\alpha$  is the factor determined by the pulse shape. For example, for rectangular pulses  $\alpha = 1$  and for gaussian shaped beams,  $\alpha = 0.753$ .

In the first figure in Figure 1.3. the illuminated length can be written as,

$$L_c = \alpha \rho \sec(\phi_{gr}) \quad (1.5)$$

In the second figure in Figure 1.3, illuminated width can be written as,

$$W_c = R\theta_{az} \quad (1.6)$$

Consequently, the illuminated patch size can also be written in terms of the illuminated length and width as follows,

$$A_c = L_c W_c \quad (1.7)$$

In the sea clutter amplitude characterizations, normalized RCS is used to eliminate the dependence on illuminated patch size for various applications. Therefore, NRCS( $\sigma_0$ ) can be defined as

$$\sigma_0 = \frac{\sigma_c}{A_c} \quad (1.8)$$

Note that NRCS is dimensionless ( $m^2/m^2$ ) and can also be described as the sea clutter reflectivity.

In this study, analysis of NRCS for sea clutter is carried out as a function of grazing angle, wind speed or sea state, radar wavelength or frequency, and polarization. To show grazing angle and polarization dependence of NRCS, an example of grazing angle versus NRCS graph is given in Figure 1.4.

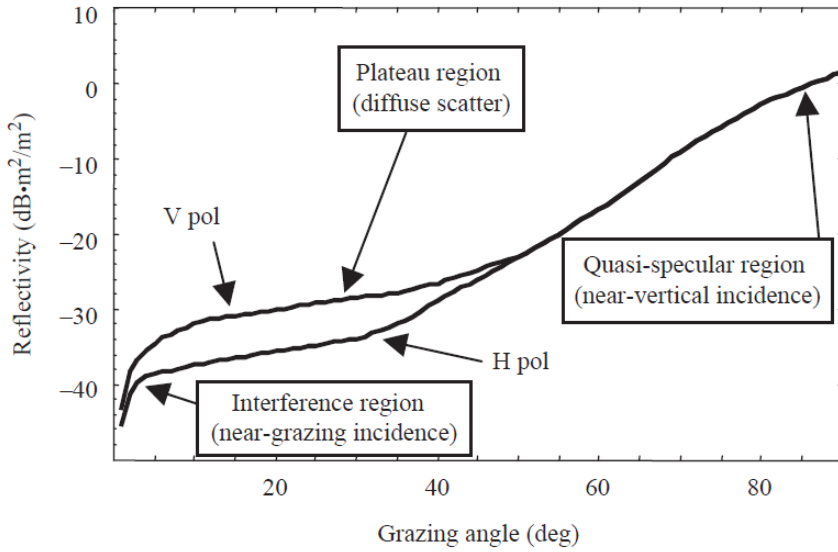


Figure 1.4. NRCS vs Grazing angle graph for I band and 15kn wind speed [12]

In Figure 1.4, Reflectivity reduces rapidly with smaller grazing angles due to shadowing and multipath interference at low grazing angles. At medium grazing angles, reflectivity shows a weaker dependence on grazing angle, and this region is called plateau region. At high grazing angles backscatter is quite large and, reflectivity increases rapidly with higher grazing angles. Moreover, up to 50 degrees, vertical polarization has greater reflectivity than horizontal polarization. In this thesis, interference region which is approximately up to 15 degrees is studied.

In addition to grazing angle and polarization, wind speed is another important factor affecting the NRCS of sea surface. Since, surface roughness is increased with the increasing wind speed, NRCS should also increase with the increasing wind speed. A comparative analysis is handled in this study for various wind speeds.

Radar frequency or wavelength is specified according to the application area. Although there are many articles devoted to this topic, still information is lacking for HF-UHF bands. By using the versatility of Method of Moments at these frequencies, a model is proposed for sea clutter reflectivity at low grazing angles and Radar frequency covering 100MHz to 500MHz.

Even though sea clutter is a 3D scattering problem, it is modeled as a 2D problem due to computational limitations. Since the resulting parameter is NRCS for the model, it is expected that the 2D model and 3D models are similar because both of them are normalized by the illuminated length and area, respectively.



## CHAPTER 2

### 1D SEA SURFACE GENERATION

In this chapter, basic concepts related to the sea surface and generation of sea surface models will be discussed. Since roughness of the sea surface is strongly related to the environmental conditions, basic definitions related to this topic are given in Section 2.1. Then, a general approach to generate rough sea surfaces will be described in Section 2.2. Moreover, two of the widely used empirical models which are Pierson-Moskowitz and Elfouhaily spectra are presented. Finally, examples of generated sea surfaces by using these models are given.

#### 2.1 Basic concepts about sea surface generation

Before discussing sea surface generation, the terminology that is used in empirical sea surface generation techniques and sea clutter modeling is given below [2][23].

**Sea state:** The numerical or written description of ocean-surface roughness. Douglas sea state which is the scale that is used in Nathanson Tables and Empirical amplitude characterization of sea clutter and World Meteorological Organization (WMO) sea state are widely used to define sea surface height profile in the literature. Douglas sea state and WMO sea state are shown in Table 2.1 and Table 2.2, respectively. Note that, sea state and sea scale are different parameters, and they should not be confused.

**Significant wave height:** The average of the heights of the one-third of the highest waves. It is also related with the sea state. It is denoted by  $H_{1/3}$ . The significant wave height can be written by using the formula given below.

$$H_{\frac{1}{3}} = \frac{1}{\frac{N}{3}} \sum_{i=1}^{N/3} H_i \quad (2.1)$$

**RMS wave height:** The root mean square of the height above the mean surface level. It is denoted by  $\sigma_h$ . A general approximation is used to relate  $H_{1/3}$  and  $\sigma_h$ , which is given below.

$$H_{\frac{1}{3}} \approx 4\sigma_h \quad (2.2)$$

**Average wave height:** It is denoted by  $h_a$ . It can be calculated by using the RMS wave height by using the formula below.

$$h_a = \sqrt{2\pi}\sigma_h \quad (2.3)$$

**Length:** Length of the spatial period of a single ocean wave is the distance from one crest to the next one. It is denoted by  $L_w$

**Spatial wavenumber:** It is defined in terms of the length of an ocean wave by using the expression below and is denoted by  $k$ .

$$k = \frac{2\pi}{L_w} \quad (2.4)$$

**Wind wave:** A wave caused by the wind blowing over the water surface.

**Gravity wave:** A wave caused by the restoring force of the gravity. Generally, waves having length greater than 1.73cm can be classified as gravity waves.

**Capillary wave:** A wave caused by the restoring force of the surface tension of water. Generally, a wave with length less than 1.73cm can be classified as capillary wave.

**Fetch:** Area on the sea surface over which wind with constant direction and speed blows. It is also called generating area.

**Duration:** The amount of time of wind blowing over the fetch.

**Fully developed sea:** A sea state produced by winds blowing over sea surface during a long period of time over a large fetch. Therefore, it can be considered as an equilibrium state reached for constant wind speed over a sufficiently large fetch and duration.

Table 2.1 Douglas Sea State [23]

Douglas Sea state	Description	SWH(ft)	Wind speed(knots)	Fetch(km)	Duration(h)
1	Smooth	0-1	0-6		
2	Slight	1-3	6-12	92.6	5
3	Moderate	3-5	12-15	222.24	20
4	Rough	5-8	15-20	227.8	23
5	Very Rough	8-12	20-25	370.4	25
6	High	12-20	25-30	555.6	27
7	Very High	20-40	30-50	926	30

Table 2.2 WMO sea state

Sea state	SWH (ft)	Description
0	0	Calm, glassy
1	0-1/3	Calm, rippled
2	1/3-2	Smooth, wavelets
3	2-4	Slight
4	4-8	Moderate
5	8-13	Rough
6	13-20	Very rough
7	20-30	High
8	30-45	Very high
9	>45	Phenomenal

Since the direct relationship between wind speed and sea state is given in Douglas sea state, it is more convenient to use it in this thesis. Moreover, using Douglas sea state which is used in Nathanson Tables and empirical models allows a comparison between proposed model and empirical models. Wind speed should be a constant parameter for a specific sea state. Thus, a relationship between wind speed and the Douglas Sea state can be defined by using the following formula.[1]

$$V_w = 3.16SS^{0.8} \quad (2.5)$$

where  $V_w$  is the wind speed in m/s and SS is the Douglas Sea State.

## 2.2 Sea surface generation

Due to complex hydrodynamical nature of sea surfaces, analysis of sea surface requires some statistical techniques. One way to do that is expressing the surface height profile as a sum of complex exponentials weighted by random coefficients by using Fourier's Theory [24]. One dimensional sea surface can be defined over a spatial region with length  $L$  e.g.  $0 < x < L$  or  $-L/2 < x < L/2$  by using the following expression. In this notation the rough surfaces are denoted in the x-y plane and y-coordinate indicates surface height.

$$y(x) = \sum_{n=-\infty}^{\infty} c_n e^{jk_n x} \quad (2.6)$$

where  $k_n = 2\pi n/L$  is the angular wavenumber of the  $n^{th}$  wave.  $c_n$ 's are the random coefficients which are usually assumed to be Gaussian distributed, are obtained by sampling the power spectral density function of the distribution [24]. In Equation 2.6., non-linear interactions between waves are neglected. In other words, the components of the complex exponentials are pairwise orthogonal. Thus, wave components are independent. Power spectral density is the Fourier Transform of the autocorrelation function. By using this property, random coefficients are filtered with the autocorrelation function. Then, taking the inverse Fourier Transform of the

filtered autocorrelation function and scaling the results gives the surface height profile of the randomly generated sea surface. [25]

By using the assumptions above, a random sea surface generation procedure is explained step by step. [26]

1. **Choosing a domain size:** It is denoted by  $L$ . In this work, the domain size is determined according to the clutter geometry presented in Chapter 1. The illuminated length is described in Equation 1.5. Thus, the domain size is related with the radar parameters such as pulse shape, radar resolution cell and grazing angle.
2. **Choosing the number of points for FFT:** It is denoted by  $N$ . It is also number of samples of the power spectrum.  $N$  should be a power of two because, in the following step inverse FFT will be calculated. Moreover,  $N$  determines the spatial grid resolution  $\Delta x$  by using the following expression.

$$\Delta x = \frac{L}{N} \quad (2.7)$$

$\Delta x$  has a great importance at the numerical simulation part of this study. It determines the domain discretization resolution of the numerical approach.

3. **Choosing a power spectral density function:** In this study, Pierson-Moskowitz spectrum and Elfouhaily spectrum are used in the sea surface generation.
4. **Choosing a wind speed:** Since the PSD functions of the empirical models are defined in terms of the wind speed, it should be specified for each sea surface generation. It is also possible to start with the Douglas sea state and convert it to the wind speed.
5. **Creating random amplitudes:** Due to the random nature of the sea surface, random numbers which are usually normally distributed with zero mean and variance chosen from the power spectrum are required.

6. **Filtering the power spectral density function with random amplitudes and taking the inverse FFT:** At this point, Fourier amplitudes are converted to the physical surface height profile.
7. **Scaling surface height profile:** Using FFT/IFFT requires scaling a factor of  $N$ . [27]

Further information related to Discrete Fourier Transform theory can be found in Appendix A.

### 2.2.1 Pierson Moskowitz Spectrum

Pierson and Moskowitz obtained a wind-dependent spectrum by using the measurement results on North Atlantic in 1963 [18]. These measurements are taken in between 20-40 knots/sec wind speed 19.5 meters above the sea surface. Moreover, this model assumes a fully developed sea. The formulated PSD in terms of the angular spatial frequency  $k$  is given below.

$$S_{PM}(k) = \frac{\alpha}{2k^3} \exp \left[ -\beta \left( \frac{g}{k} \right)^2 \frac{1}{U_{19.5}^4} \right] \left[ \frac{m^2}{\frac{rad}{m}} \right] \quad (2.8)$$

where  $\alpha = 0.0081$ ,  $\beta = 0.74$ ,  $g = 9.82 \text{ m/s}^2$  is the acceleration of gravity,  $U_{19.5}$  is the wind speed in m/s obtained from 19.5 meters above the sea surface and  $k$  is the angular spatial frequency in rad/m.  $U_{19.5}$  can be converted to  $U_{10}$  which is wind speed 10 meters above the sea surface by using the following approximate formula.

$$U_{10} \approx 1.026 U_{19.5} \quad (2.9)$$

Integrating Equation 2.8 over  $k$  gives the variance of the surface height profile. [25]

$$\sigma_h^2 = \int_0^{\infty} S_{PM}(k) dk = \frac{\alpha}{4\beta} \frac{U_{19.5}^4}{g^2} = 0.00274 \frac{U_{19.5}^4}{g^2} \quad (2.10)$$

And by using Equation 2.2, SWH can be written by using the following formula.

$$H_{\frac{1}{3}} \approx 4\sigma_h = 0.2094 \frac{U_{19.5}^2}{g} \quad (2.11)$$

Although, PM spectrum is reasonably accurate and simple to implement, one of its major drawbacks is that for increasing wind speeds capillary waves are neglected. Moreover, it is used in the literature for wind speeds below 20 knots/s, but measurements taken between 20-40 knots/s are fitted for this range of wind speeds. Therefore, using wind speeds between 20-40 knots/s would give more realistic results. Converting knots to meter, converts the wind range of 20-40 knots/s to 10-20 m/s approximately.

The PSD functions for wind speeds from 10m/s up to 20 m/s with 2m/s step are given in Figure 2.1 as follows.

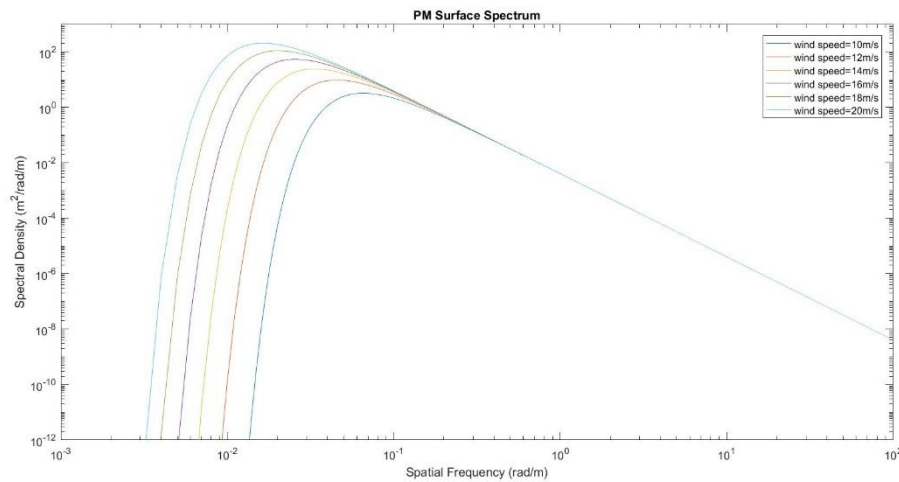


Figure 2.1. Pierson Moskowitz spectrum versus spatial frequency for wind speeds from 10m/s up to 20 m/s with 2m/s increments

As a starting point of this study, PM spectrum is chosen to generate sea surfaces. Because of the lack of information below 10m/s wind speed, and underestimated high frequency components in this spectrum, a necessity arises for a modified model which includes both high and low frequency components. In this sense, many other models such as Bjerkaas and Riedel spectrum (1979), Donelan and Pierson spectrum (1987), Apel spectrum (1994), Elfouhaily spectrum (1997) are used which are

relatively new and capable of modeling both capillary and gravity waves. Moreover, fully developed sea assumption is no longer valid for these models. Thus, fetch size is another parameter that determines the PSD. Next section is devoted to the formulation of Elfouhaily spectrum and explanation of this model.

## 2.2.2 Elfouhaily Spectrum

El fouhaily spectrum is a model which is valid over high and low spatial frequency components [19]. To accomplish this, Elfouhaily spectrum is composed of two spectra regimes which are denoted by  $B_l$  and  $B_h$ . In this notation,  $l$  and  $h$  stand for low and high frequencies and  $B$  represents the curvature spectrum ( $B(k) = k^3 S(k)$ ).  $B_l$  is formulated based on the measurements taken by Hasselmann et al. during the Joint North Sea Wave Project (JONSWAP) [28] and  $B_h$  is formulated based on the work of Phillips [28] and Kitaigorodskii [30]. The composite model which is constructed by Elfouhaily et al. is given by Heron [31] as presented below.

$$S_{Elf}(k) = k^{-3}(B_l + B_h) \quad (2.12)$$

The low frequency term  $B_l$  in Equation 2.12 is defined as

$$B_l = \frac{\alpha_p c_p}{2} L_{PM} J_p \exp \left[ -\frac{\Omega}{\sqrt{10}} \left( \sqrt{\frac{k}{k_p}} - 1 \right) \right] \quad (2.13)$$

where  $\alpha_p$  is the Phillips-Kitaigorodskii equilibrium range parameter and formulated as

$$\alpha_p = 0.006 \sqrt{\Omega} \quad (2.14)$$

where  $\Omega$  in Equation 2.14 stands for dimensionless inverse wave age parameter defined as

$$\Omega = 0.84 \tanh^{-0.75} \left( \frac{X}{X_0} \right)^{0.4} \quad (2.15)$$

$X_0 = 22000$  is fetch constant and  $X = gx/U_{10}^2$  is the non-dimensional fetch where  $x$  is the dimensional fetch in meters.

$c_p$  in Equation 2.13 is the wave speed at the peak of the low frequency wave spectrum and is written as follows.

$$c_p = \left(\frac{g}{k_p}\right)^{0.5} \quad (2.16a)$$

$$k_p = \frac{g}{U_{10}^2} \Omega^2 \quad (2.16b)$$

where  $k_p$  is the peak wavenumber and similarly  $c = \left(\frac{g}{k}\right)^{0.5}$  is the wave speed.

The PM spectral shape  $L_{PM}$  can be written in terms of  $k_p$  and  $k$  as follows,

$$L_{PM} = \exp\left[-\frac{5}{4}\left(\frac{k_p}{k}\right)^2\right] \quad (2.17)$$

$J_p$  in Equation 2.13, represents the JONSWAP peak enhancement factor and formulated below [29]. By using this factor, the wave spectrum is assumed not to be fully developed.

$$J_p = \gamma^\Gamma \quad (2.18a)$$

$$\gamma = 1.7 \text{ for } 0.84 < \Omega < 1 \quad (2.18b)$$

$$\gamma = 1.7 + 6 \ln \Omega \text{ for } 1 < \Omega < 1 \quad (2.18c)$$

$$\Gamma = \exp\left[\frac{-\left(\sqrt{\frac{k}{k_p}} - 1\right)^2}{2\sigma_E^2}\right] \quad (2.18d)$$

$$\sigma_E = 0.08(1 + 4\Omega^{-3}) \quad (2.18e)$$

The high frequency term  $B_h$  in Equation 2.12 is defined as

$$B_h = \frac{\alpha_m c_m}{2c} \exp \left[ -\frac{1}{4} \left( \frac{k}{k_m} - 1 \right)^2 \right] \quad (2.20)$$

$c_m$  is the capillary peak wave speed and  $k_m$  is the capillary peak wave number both having constant values which are 0.23m/sec and 361.4/m, respectively.

In Equation 2.20,  $\alpha_m$  term is the analogous to the  $\alpha_p$  in Equation 2.13, and can be computed by using the formulation below.

$$\alpha_m = 0.01 \left[ 1 + \ln \left( \frac{u^*}{c_m} \right) \right] \text{ for } u^* < c_m \quad (2.21a)$$

$$\alpha_m = 0.01 \left[ 1 + 3 \ln \left( \frac{u^*}{c_m} \right) \right] \text{ for } u^* > c_m \quad (2.21b)$$

where  $u^*$  is the friction velocity and described as,

$$u^* = \frac{0.42 U_{10}}{\ln \left( \frac{10}{z_0} \right)} \quad (2.21c)$$

And  $z_0$  is the roughness length which is corrected [25] from the original paper [31] as given below.

$$z_0 = 3.17 \cdot 10^{-5} \left( \frac{U_{10}^2}{g} \right) \left( \frac{U_{10}}{c_p} \right) \quad (2.21d)$$

By using the above formulation, Elfouhaily spectrum can be obtained for different wind speeds and fetch sizes. It is also possible to use the Douglas Sea State parameters by using Equation 2.5. and Table 2.1.

In addition, Elfouhaily spectrum and its low and high frequency curvature components are plotted with respect to spatial frequency for sea states 1 to 7 and shown in Figure 2.2 and Figure 2.3.

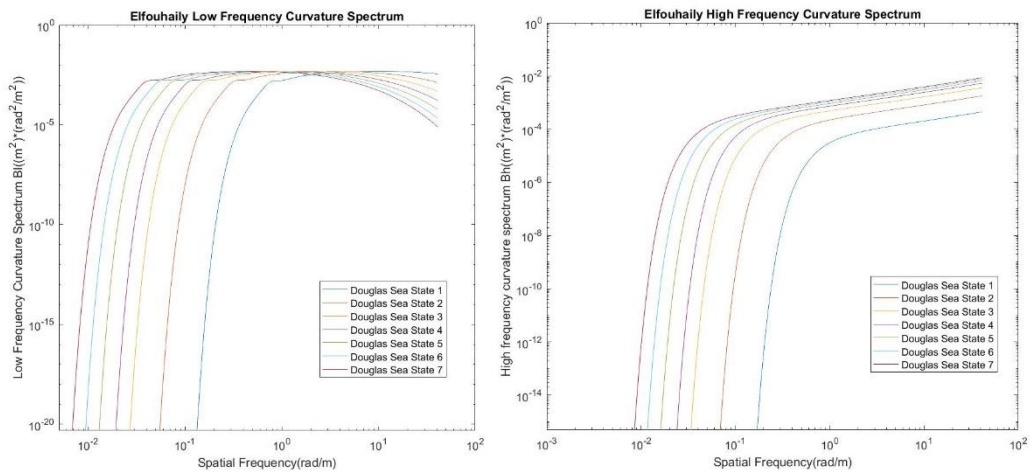


Figure 2.2. Elfouhaily Model High Frequency and Low Frequency Curvature Spectrum for Sea States 1 to 7

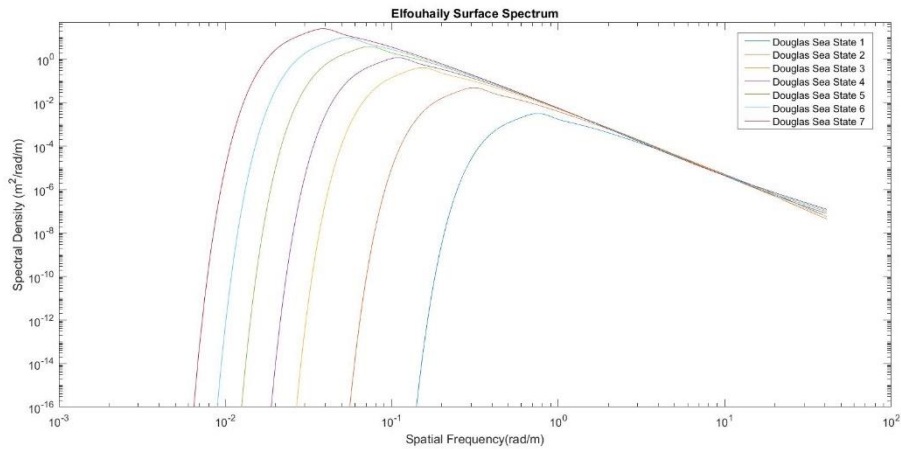


Figure 2.3. Elfouhaily spectrum versus spatial frequency for Sea States 1 to 7

Since Elfouhaily spectrum is valid over wider range of wind speeds than those in the Pierson Moskowitz spectrum and includes both low and high frequency components, Elfouhaily spectrum is used in this work to increase the accuracy of the simulation.

### 2.2.3 Examples of randomly generated sea surfaces by using Pierson Moskowitz and Elfouhaily Spectrum

In this section, parameters required for sea surface generation by PM spectrum and Elfouhaily spectrum are specified. Then, by using these parameters, examples of both models are presented.

As a first step, domain size should be specified. As it was previously explained, grazing angle, radar resolution cell and pulse compression parameter are required to determine the domain size i.e., 1D length of the sea surface. In Nathanson Data, pulse length is specified as  $0.5\mu\text{sec}$  to  $10\mu\text{sec}$  and grazing angles are up to 30 degrees. There is an uncertainty about the pulse compression parameter, but it is assumed that the pulse is uncoded, in other words  $\alpha = 1$ . In the light of these information about Nathanson Table, domain size is in between 75m and 1732m. Increasing the domain size increases the computational load of the simulation. Consequently, for the sake of feasible simulation time, domain size is chosen in between 60m and 150m.

Then, the number of points for FFT should be specified. Since N should be a power of 2, N=1024 is a reasonable choice for computational load of the problem such that, spatial grid resolution is approximately equal to the segment size of the numerical analysis. For example, for 100MHz radar frequency, wavelength is 3m and the spatial grid resolution is  $\Delta x = 0.098m = \lambda/30.72$ . Although the segment size is not equal to the spatial grid resolution, it gives an estimation about the segment size. Segment size can be calculated by using the following formula.

$$\Delta C = \sqrt{\Delta x^2 + \Delta y^2} \quad (2.22)$$

where  $\Delta C$  is segment size and  $\Delta y$  is the surface height difference in one segment.

For an accurate numerical simulation, the segment size should be less than  $\frac{\lambda}{10}$ . Increasing the surface roughness for a fixed domain size yields an increase in the segment size. For this reason, segment size should be checked for large wind speeds.

One other parameter needed for generating the sea surface is wind speed. Fetch size is also another parameter for Elfouhaily model which is also related to the wind speed. Using the Douglas Sea State is another option which both defines the Fetch size in Table 2.1 and wind speed in Equation 2.5. The wind generated sea surface examples by using both models and the specified parameters above, are shown in Figure 2.4 and Figure 2.5 below.

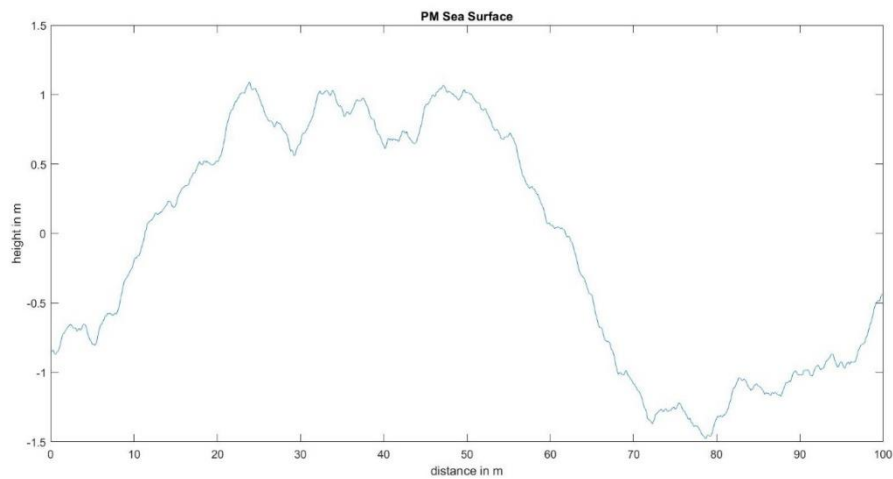


Figure 2.4. Single Surface Realization by using PM spectrum at Sea State 5

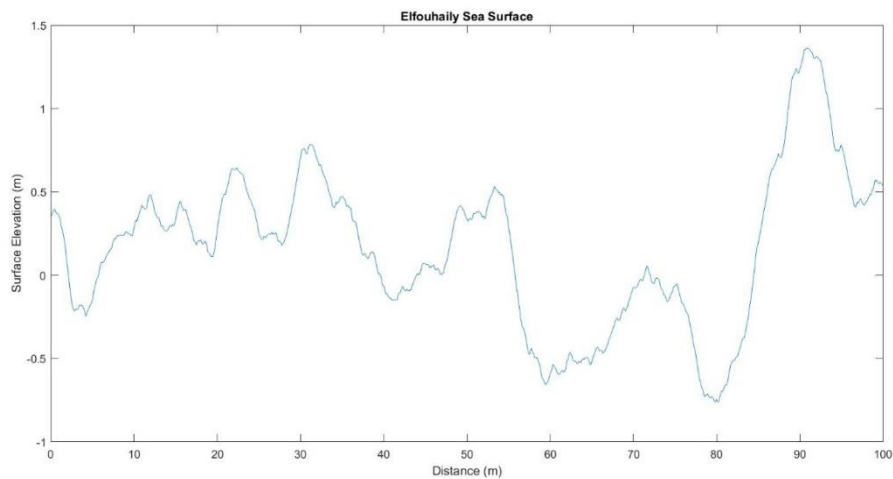


Figure 2.5. Single Surface Realization by using Elfouhaily spectrum at Sea State 5

Sea state 5 is chosen for single surface realization corresponding to 11.4m/s wind speed which is in between the range specified in the PM model. Although, as it can

be seen from Figure 2.4 and Figure 2.5, there is not much difference between the generated sea surfaces, amplitude characteristics differ from each other. Since, Elfouhaily model includes capillary wave components, these waves might be important for small wind speeds and low frequencies.

Moreover, it is also possible to generate a relatively long surface and applying the space sampling to obtain amplitude characterization. Therefore, parameters like  $L$  and  $N$  might be different for space sampling and ensemble sampling techniques as presented in Chapter 5.

It is noted that accurate sea surface generation is a difficult task due to complex hydrodynamical nature of sea surface. Thus, further analysis about sea surface generation is beyond of the scope of this thesis.

## CHAPTER 3

### Method of Moments

In scattering problems, integral and/or differential form of Maxwell's Equations are the governing equations. Direct solution of these equations, which are called analytical solutions may not be possible for several scattering problems. Scattering problems such as sea clutter calculation is obviously electrically large, complex, and rough surface scattering problem. As compared to very restrictive analytical solutions of rough surface scattering problem, more accurate solutions can be obtained due to the divide and conquer strategy of numerical techniques.

By using some approximations and divide and conquer strategy, computational burden of the problem is lightened. In addition, increased computational capability of the computers enables fast and accurate solution of EM problems. Finite Element Method (FEM), Method of Moments (MoM), Finite Difference Method (FDM) and Finite Difference Time Domain Method (FDTD) are most frequently used four methods in the literature.

Depending on the application, each method has both advantages and disadvantages against each other. MoM is an integral equation-based method and others are Differential Equation approaches. Integral equation approach has an advantage in free space but extremely difficult in non-homogenous media. In this study, sea surface at low grazing angles is assumed to be Perfect Electric Conductor (PEC). Therefore, there will be only two homogenous media which are free space and PEC. Moreover, MoM is preferable for boundaries like Figure 2.4 and Figure 2.5 based on the Surface Equivalence Principle. MoM has another advantage for conducting objects. The integral equation is defined over a curve in 2D, which means that problem dimension is reduced by one. However, for dielectric objects the computational load is quite high. In addition, MoM and FEM are more accurate than

FD and FDTD for irregular geometries due to staircasing errors occurring in FD and FDTD. However, applying MoM results in a full matrix equation. In other words, every point on the surface is related to every other point via Green's function and consequently MoM suffers from heavy computational load [39]. To sum up, MoM is chosen due to suitability for PEC, and complex boundaries like sea surface, but a special care must be taken to apply MoM to avoid long computation time.

MoM is a technique used to solve electromagnetic boundary or volume integral equations in the frequency domain [32]. Sea clutter scattering problem can be represented in terms of electromagnetic boundary integral equations. In this sense, a derivation for integral equations starting from Maxwell's Equations is presented below.

### 3.1 Maxwell's Equations

In a homogenous medium, Maxwell's Equations in frequency domain are expressed as follows [32]

$$\nabla \times \bar{E} = -\bar{M} - j\omega\mu\bar{H} \quad (3.1)$$

$$\nabla \times \bar{H} = \bar{J} + j\omega\varepsilon\bar{E} \quad (3.2)$$

$$\nabla \cdot \bar{D} = q_e \quad (3.3)$$

$$\nabla \cdot \bar{B} = q_m \quad (3.4)$$

where  $\bar{E}$  and  $\bar{H}$  are electric and magnetic field intensity vectors,  $\bar{D}$  and  $\bar{B}$  are electric and magnetic flux density vectors,  $\bar{J}$  and  $\bar{M}$  are electric and magnetic current density vectors,  $q_e$  and  $q_m$  are electric and magnetic volume charge densities,  $\mu$  is permeability,  $\varepsilon$  is permittivity,  $\omega$  is angular frequency. Although, magnetic charge and magnetic current are not observed in nature, they are used in the formulation of scattering problem as equivalent sources.

$\bar{D}$  and  $\bar{B}$  are related to  $\bar{E}$  and  $\bar{H}$  by using the constitutive relations given in Equations 3.5 and 3.6.

$$\bar{D} = \varepsilon \bar{E} \quad (3.5)$$

$$\bar{B} = \mu \bar{H} \quad (3.6)$$

Permittivity and permeability can be written in terms of free space permittivity  $\varepsilon_0$  and permeability  $\mu_0$  and relative permittivity  $\varepsilon_r$  and permeability  $\mu_r$  coefficients as shown below.

$$\varepsilon = \varepsilon_0 \varepsilon_r \quad (3.7)$$

$$\mu = \mu_0 \mu_r \quad (3.8)$$

Time dependence  $e^{j\omega t}$  is used and suppressed in this study.

### 3.2 Electromagnetic Boundary Conditions

As it can be seen from Figure 3.1., at the interface between two homogenous media with different electrical parameters, boundary conditions in Equations 3.9-3.12 should be satisfied.

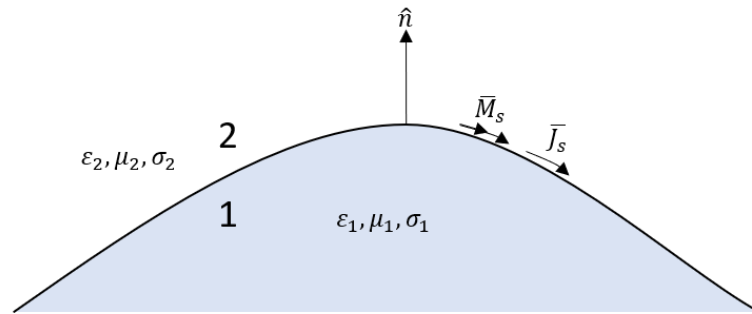


Figure 3.1. Interface between two media with different electrical parameters

$$-\hat{n} \times (\bar{E}_2 - \bar{E}_1) = \bar{M}_s \quad (3.9)$$

$$\hat{n} \times (\bar{H}_2 - \bar{H}_1) = \bar{J}_s \quad (3.10)$$

$$\hat{n} \cdot (\bar{D}_2 - \bar{D}_1) = q_e \quad (3.11)$$

$$\hat{n} \cdot (\overline{B}_2 - \overline{B}_1) = q_m \quad (3.12)$$

where  $\hat{n}$  is the unit normal vector to the surface,  $\overline{M}_S$  and  $\overline{J}_S$  are the surface magnetic and electric current density vectors, respectively.

As stated before, in this work Region 1 is assumed to be PEC. Since the tangential Electric Field is zero on the surface of PEC,  $\overline{M}_S$  and  $q_m$  vanishes. And inside the PEC the field is zero. Therefore, boundary conditions for PEC can be simplified as,

$$-\hat{n} \times \overline{E}_2 = 0 \quad (3.13)$$

$$\hat{n} \times \overline{H}_2 = \overline{J}_S \quad (3.14)$$

$$\hat{n} \cdot \overline{D}_2 = q_e \quad (3.15)$$

$$\hat{n} \cdot \overline{B}_2 = 0 \quad (3.16)$$

### 3.3 Reduced Wave Equations

2D EM scattering problems can be considered as 3D problems where the geometry and fields do not change as a function of one of the Cartesian coordinates. In addition, any arbitrary field can be expressed as the sum of transverse electric and transverse magnetic field components. Thus, 2D scattering problem can be solved for two polarizations, namely  $TM_z$  and  $TE_z$ , in which there is no variation in z-coordinate. In z direction the cross sectional geometry does not change. For  $TM_z$  waves only  $E_z, H_y, H_x$  are non-zero and for  $TE_z$  waves there are only  $H_z, E_y, E_x$  field components.

In a region where only electric current density  $\overline{J}$  exists, Equation 3.1 and 3.2 can be modified as,

$$\nabla \times \overline{E} = -j\omega\mu\overline{H} \quad (3.17)$$

$$\nabla \times \overline{H} = j\omega\varepsilon\overline{E} + \overline{J} \quad (3.18)$$

By taking the curl of Equation 3.17 and inserting Equation 3.18 into it, wave equation for  $TM_z$  case is obtained as shown below.

$$\nabla \times \nabla \times \bar{E} = -j\omega\mu\nabla \times \bar{H} \quad (3.19)$$

$$\nabla \times \nabla \times \bar{E} - k^2\bar{E} = -j\omega\mu\bar{J} \quad (3.20)$$

where  $k = \omega\sqrt{\mu\varepsilon} = \frac{2\pi}{\lambda}$  is wave number and  $\lambda$  is the wavelength.

In  $TM_z$  case evaluating curl-curl operator on  $\bar{E} = \hat{a}_z E_z(x, y)$  results in Equation 3.21 which is called the reduced wave equation or Helmholtz equation.

$$\left( \frac{\partial^2 E_z}{\partial x^2} + \frac{\partial^2 E_z}{\partial y^2} \right) + k^2 E_z = j\omega\mu J_z \quad (3.21)$$

In a similar way, reduced wave equation for  $TE_z$  case, can be obtained by taking the curl of Equation 3.18 and inserting Equation 3.17 into it.

$$\nabla \times \nabla \times \bar{H} = j\omega\varepsilon\nabla \times \bar{E} + \nabla \times \bar{J} \quad (3.22)$$

$$\nabla \times \nabla \times \bar{H} - k^2\bar{H} = \nabla \times \bar{J} \quad (3.23)$$

Evaluating the curl-curl operator on  $\bar{H} = \hat{a}_z H_z(x, y)$  in Equation 3.23 yields

$$\left( \frac{\partial^2 H_z}{\partial x^2} + \frac{\partial^2 H_z}{\partial y^2} \right) + k^2 H_z \hat{a}_z = -\nabla \times \bar{J}_S \quad (3.24)$$

Since the left-hand side of Equation 3.24 has only the z component, the electric current density in right-hand side should only have x and y components. Thus,  $\bar{J}_S$  denotes electric current density transverse to z plane.

### 3.4 Auxiliary Potentials

Although auxiliary potentials are not physically measurable quantities, they are mathematical tools to solve scattering problems. Both magnetic and electric vector potentials can be used for the solution of scattering problems, but in this study only the magnetic vector potential approach is presented.

These auxiliary potentials are denoted as  $V$ , electric scalar potential and  $\bar{A}$ , magnetic vector potentials. These arbitrary potentials must satisfy the curl and divergence equations given below.

$$\nabla \times \nabla V = 0 \quad (3.25)$$

$$\nabla \cdot \nabla \times \bar{A} = 0 \quad (3.26)$$

For homogenous and source-free region, the magnetic field  $\bar{H}$  is always solenoidal. Therefore, it can be written in term of a magnetic vector potential  $\bar{A}$  given in Equation 3.28.

$$\bar{B} = \nabla \times \bar{A} \quad (3.27)$$

$$\bar{H} = \frac{1}{\mu} \nabla \times \bar{A} \quad (3.28)$$

Substituting Equation 3.28 into Equation 3.1, we get

$$-\nabla \times (\bar{E} + j\omega\bar{A}) = 0 \quad (3.29)$$

And by using the property in Equation 3.26, Equation 3.29 is modified below.

$$\bar{E} = -\nabla V - j\omega\bar{A} \quad (3.30)$$

If electric scalar potential and magnetic vector potential in Equation 3.30 can be found, then electric and magnetic field intensity vectors are obtained easily. To do this, curl of both sides of Equation 3.28 are evaluated, and vector identity in Appendix B is applied.

$$\mu\nabla \times \bar{H} = \nabla(\nabla \cdot \bar{A}) - \nabla^2 \bar{A} \quad (3.31)$$

And combining and rearranging Equation 3.2, 3.30 and 3.31, we get

$$\nabla^2 \bar{A} + k^2 \bar{A} = -\mu\bar{J} + \nabla(\nabla \cdot \bar{A} + j\omega\mu\varepsilon V) \quad (3.32)$$

If the divergence of  $\bar{A}$  is defined as in Equation 3.33, Equation 3.32 becomes an inhomogeneous Helmholtz equation in Equation 3.34. The Equation 3.33 is also called Lorentz gauge.

$$\nabla \cdot \bar{A} = -j\omega\mu\epsilon V \quad (3.33)$$

$$\nabla^2 \bar{A} + k^2 \bar{A} = -\mu \bar{J} \quad (3.34)$$

The solution of Helmholtz equation in 2D can be obtained via 2D Green's function as given in Appendix C.

$$\bar{A} = \frac{-j\mu}{4} \int_{S'} \bar{J}(\bar{r}') H_0^{(2)}(k|\bar{r} - \bar{r}'|) d\bar{S}' \quad (3.35)$$

where  $\bar{r} = \hat{a}_x x + \hat{a}_y y$  is observation point,  $\bar{r}' = \hat{a}_x x' + \hat{a}_y y'$  is the source point,  $H_0^{(2)}(\cdot)$  is the Hankel function of the second kind of order zero.

### 3.5 Surface Integral Equations

In this section, surface integral equations are derived by using Equation 3.34 and Equation 3.21 in the presence of a 2D PEC scatterer. Surface integral equations are namely the Electric Field Integral Equation (EFIE) and Magnetic Field Integral Equation (MFIE). The EFIE and MFIE are obtained by imposing boundary conditions on the surface of PEC in Equation 3.13 and 3.14, respectively. Another way to obtain EFIE and MFIE is using surface equivalence principle i.e., Huygens' principle [33]. Using the surface equivalence principle, the scatterer can be replaced by equivalent electric currents radiating in free space. To illustrate the equivalent problem, consider a PEC scatterer which is illuminated by an incident wave in Figure 3.2.

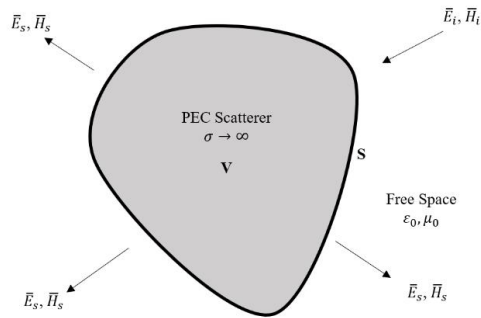


Figure 3.2. PEC Scatterer illuminated by an incident wave

In Figure 3.2, incident field is denoted by  $\vec{E}_i, \vec{H}_i$  and the scattered field is denoted by  $\vec{E}_s, \vec{H}_s$ . Replacing the object with free space and placing the equivalent electric and magnetic current densities on the surface, the total field does not change. Then, equivalent problem can be constructed by using the Surface Equivalence Principle in Figure 3.3.

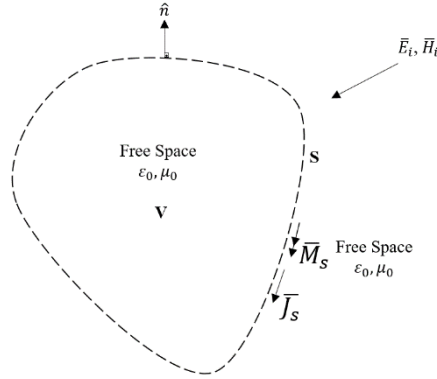


Figure 3.3. Surface Equivalence Principle

The surface electric and magnetic current densities are obtained as follows.

$$\vec{J}_s = \hat{n} \times \vec{H}_t \quad (3.36)$$

$$\vec{M}_s = \vec{E}_t \times \hat{n} = 0 \quad (3.37)$$

where electric and magnetic total field on the surface of the PEC surface is denoted by  $\vec{E}_t, \vec{H}_t$  respectively.

Since the tangential electric field on PEC surface is zero, the magnetic current density is also equal to zero in Equation 3.37. Note that, these equations are only applicable outside the object.

Once EFIE or MFIE is obtained by using Surface Equivalence Principle, it is possible to calculate the surface current density on the surface. Then, scattered electric field or magnetic field intensities can be found from the surface current density as radiation integrals. Moreover, far field quantities like RCS and NRCS can be calculated.

According to C. Balanis [34], for TM case EFIE and for TE case MFIE are convenient integral equation forms. Thus, TM-EFIE and TE-MFIE are preferred for the sake of simplicity and computational load.

### 3.5.1 Transverse Magnetic Electric Field Integral Equation (TM-EFIE)

The TM-EFIE is based on the boundary condition that is specified in Equation 3.37. TM-EFIE may be derived by using either magnetic vector potential or directly from the reduced wave equation in Equation 3.21. In this study, direct derivation of TM-EFIE by using Equation 3.21 is presented below.

The scattered electric field can be formulated by using the integral expression given in Equation 3.21. It is formed by using the 2D Green's Function in Equation 3.38.[35]

$$E_z^s(\bar{r}) = \frac{-k\eta_0}{4} \int_{C'} J_z(\bar{r}') H_0^{(2)}(k|\bar{r} - \bar{r}'|) dl' \quad (3.38)$$

where  $\eta_0 \approx 120\pi \Omega$  is the intrinsic impedance of free space,  $\bar{r} = \hat{a}_x x + \hat{a}_y y$  is observation point,  $\bar{r}' = \hat{a}_x x' + \hat{a}_y y'$  is the source point,  $H_0^{(2)}(.)$  is the Hankel function of the second kind of order zero.

To depict  $TM_z$  scattering problem as sea surface scattering problem, Figure 3.4. is shown below.

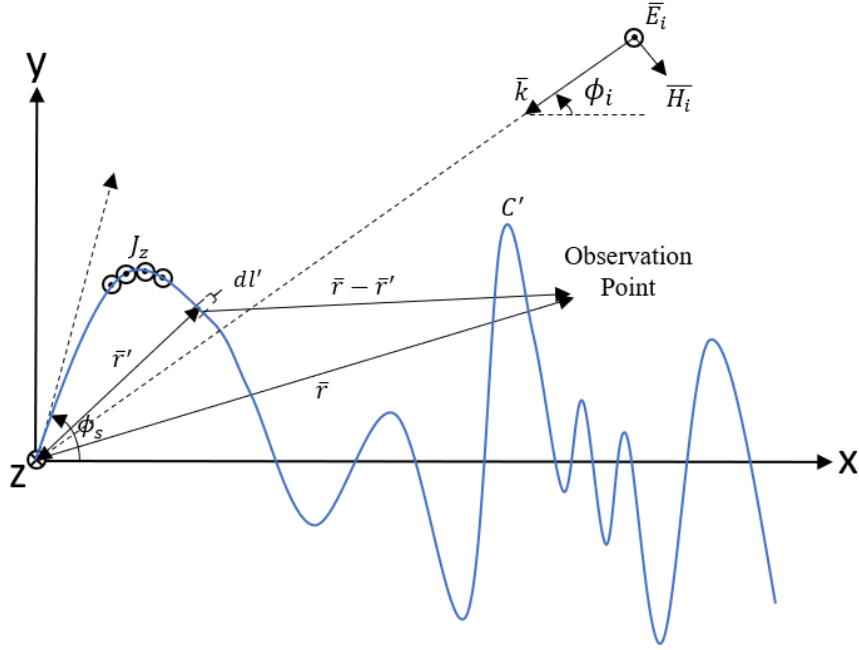


Figure 3.4.  $TM_z$  case sea surface scattering

From Equation 3.37, the tangential total electric field on the surface of PEC is equal to zero and  $E_z$  is already tangential to the PEC surface. Thus, Equation 3.37 can be rearranged by moving the observation point on the surface of the PEC.

$$E_z^s + E_z^i = 0 \text{ or } E_z^i = -E_z^s \text{ on } C' \quad (3.39)$$

Hence, combining Equation 3.38 and 3.39, TM-EFIE can be obtained given in Equation 3.40.

$$\frac{k\eta_0}{4} \int_{C'} J_z(\vec{r}') H_0^{(2)}(k|\vec{r} - \vec{r}'|) dl' = E_z^i(\vec{r}) \quad (3.40)$$

$$\mathcal{L}_{TM-EFIE} J_z = E_z^i \quad (3.41)$$

where  $E_z^i$  is the known incident field,  $J_z$  is the unknown surface current density and  $\mathcal{L}_{TM-EFIE}$  is the TM-EFIE operator.

Moreover,  $E_z^i$  can be written in terms of incidence angle  $\phi_i$  and wave number  $k$  from Figure 3.4.

$$E_z^i = e^{-j\vec{k}\cdot\vec{r}} = e^{jk(x\cos\phi_i + y\sin\phi_i)} \quad (3.42)$$

### 3.5.2 Transverse Electric Magnetic Field Integral Equation (TE-MFIE)

TE-MFIE formulation is based on the boundary condition on the surface of the PEC specified in Equation 3.36. Contrary to TM-EFIE derivation, TE-MFIE is derived by using magnetic vector potential. To achieve this, scattered magnetic field is formulated by combining Equation 3.28 and Equation 3.35.

$$\hat{a}_z H_z^t(x, y) = \frac{1}{\mu} \nabla \times \bar{A} = \frac{1}{\mu} \left( \frac{\partial A_y}{\partial x} - \frac{\partial A_x}{\partial y} \right) \hat{a}_z \quad (3.43)$$

$TE_z$  case scattering problem as sea surface scattering problem is depicted in Figure 3.5 as shown below.

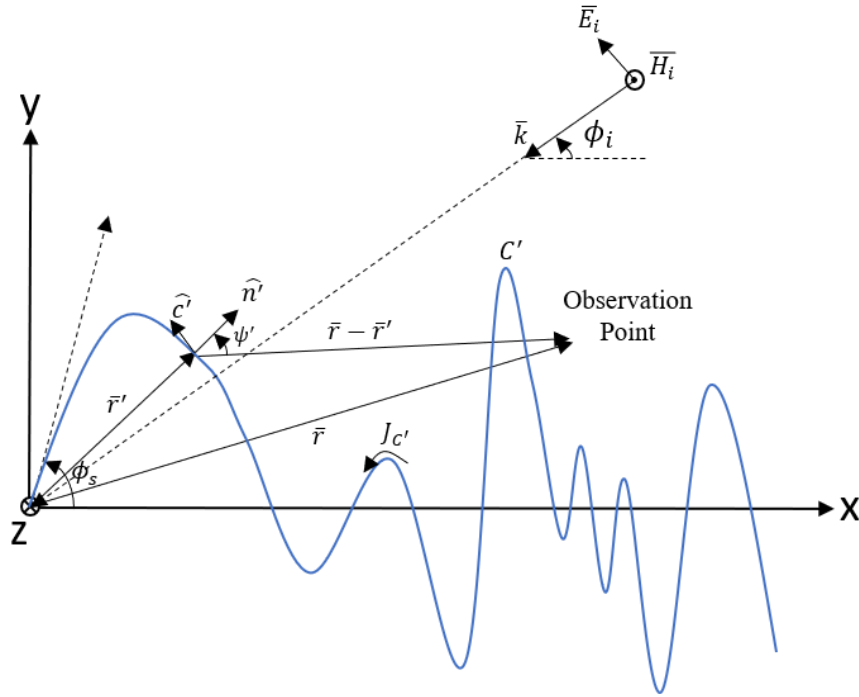


Figure 3.5.  $TE_z$  case sea surface scattering

Since the incident magnetic field has only the z component in  $TE_z$  case, the scattered magnetic field has also only the z component in Equation 3.43. For the same reason, current induced on the surface of the PEC should be tangent to the surface [34]. Thus, the surface current density in Equation 3.36 can be rewritten as,

$$\bar{J}_s = \hat{c}' J_{c'}(\bar{r}') \quad (3.44)$$

where  $\hat{c}' = \hat{a}_x \cos \theta' + \hat{a}_y \sin \theta'$  indicates the tangent vector to the surface and  $J_{C'}(\bar{r}')$  is the induced current density.

Imposing the boundary condition in Equation 3.36 on the surface and combining Equation 3.44 with it yields Equation 3.45.

$$\hat{c}' J_{C'}(\bar{r}')|_{C'} = \hat{n}' \times (\hat{a}_z H_z^i + \hat{a}_z H_z^s)|_{C'} \quad (3.45)$$

By using the geometry in Figure 3.5, Equation 3.45 can be rearranged as

$$\hat{c}' J_{C'}(\bar{r}')|_{C'} = -\hat{c}' H_z^i|_{C'} - \hat{c}' H_z^s|_{C'} \quad (3.46)$$

Using Equation 3.43 and Equation 3.46, a scalar formulation is obtained below.

$$J_{C'}(\bar{r}') + \frac{1}{\mu} \left( \frac{\partial A_y}{\partial x} - \frac{\partial A_x}{\partial y} \right) = -H_z^i \quad (3.47)$$

where  $A_y$  and  $A_x$  are the y and x components of the vector magnetic field and they can be expressed as,

$$A_x = \frac{-j\mu}{4} \int_{S'} J_{C'}(\bar{r}') \cos \theta' H_0^{(2)}(k|\bar{r} - \bar{r}'|) d\bar{l}' \quad (3.48)$$

$$A_y = \frac{-j\mu}{4} \int_{S'} J_{C'}(\bar{r}') \sin \theta' H_0^{(2)}(k|\bar{r} - \bar{r}'|) d\bar{l}' \quad (3.49)$$

To simplify Equation 3.47, derivatives of Hankel function with respect to x and y are required. [34]

$$\frac{d}{dx} H_p^{(2)}(x) = -H_{p+1}^{(2)}(x) + \frac{p}{x} H_p^{(2)}(x) \quad (3.50)$$

$$\frac{\partial}{\partial x} H_0^{(2)}(kR) = -H_1^{(2)}(kR) \frac{\partial(kR)}{\partial x} \quad (3.51)$$

$$\frac{\partial}{\partial y} H_0^{(2)}(kR) = -H_1^{(2)}(kR) \frac{\partial(kR)}{\partial y} \quad (3.52)$$

Finally, TE-MFIE is obtained with the combination of Equations 3.47, 3.48, 3.49, 3.51 and 3.52.

$$J_{C'}(\bar{r}') + \frac{jk}{4} \int_{C'} J_{C'}(\bar{r}') H_1^{(2)}(kR) \left( \sin \theta' \frac{(x-x')}{R} - \cos \theta' \frac{(y-y')}{R} \right) dl' = -H_z^i \quad (3.53)$$

By using the geometric parameters in Figure 3.5, another form of the TE-MFIE can be written as

$$J_{C'}(\bar{r}') + \frac{jk}{4} \int_{C'} J_{C'}(\bar{r}') H_1^{(2)}(kR) \cos(\psi') dl' = -H_z^i \quad (3.54)$$

where  $\psi'$  is the angle between surface normal vector  $\hat{n}'$  and the vector  $\bar{r} - \bar{r}'$ .

Moreover, TE-MFIE can be written in the form of linear operator form shown below.

$$\mathcal{L}_{TE-MFIE} J_{C'} = -H_z^i \quad (3.55)$$

where  $\mathcal{L}_{TE-MFIE}$  is the linear TE-MFIE operator.

### 3.6 Method of Moments

In the previous section, TM-EFIE and TE-MFIE are derived. Although they are different kinds of Fredholm integral equations, they can be denoted by using the inhomogeneous operator form shown below. [36]

$$\mathcal{L}(f) = g \quad (3.56)$$

where  $\mathcal{L}$  is a linear integral operator,  $g$  is the known function and  $f$  is the unknown function.  $f$  can be represented a weighted sum of known functions approximately in Equation 3.57. By substituting this expression in 3.56, Equation 3.56 is discretized.

$$f \cong \sum_{j=1}^N c_j f_j \quad (3.57)$$

where  $c_j$ 's are unknown coefficients and  $f_j$ 's are basis functions. Basis function is also called approximating, expansion, trial, or shape function. Substituting Equation 3.57 into operator form and using linearity yields Equation 3.58.

$$\sum_{j=1}^N c_j \mathcal{L}f_j \cong g \quad (3.58)$$

Since unknown function  $f$  is approximated and inserted into the integral equation, residual or error function can be defined as,

$$R = g - \sum_{j=1}^N c_j \mathcal{L}f_j \quad (3.59)$$

In order to minimize the residual function, inner product  $\langle ., . \rangle$  of the residual with a weighting function is evaluated and equated to zero. By this way, a matrix system can be obtained with  $N$  equations with  $N$  unknowns. Resulting matrix system is shown in Equation 3.60-3.64.

$$\langle R, w_i \rangle = 0 \quad (3.60)$$

$$\left\langle g - \sum_{j=1}^N c_j \mathcal{L}f_j, w_i \right\rangle = 0 \quad (3.61)$$

$$\left\langle \sum_{j=1}^N c_j \mathcal{L}f_j, w_i \right\rangle = \langle g, w_i \rangle \quad (3.62)$$

$$\sum_{j=1}^N c_j \langle \mathcal{L}f_j, w_i \rangle = \langle g, w_i \rangle \quad (3.63)$$

$$[Z_{ij}][c_j] = [g_i] \quad (3.64)$$

where  $w_i$  is the weighting function,  $[Z_{ij}]$  is the  $N \times N$  impedance matrix,  $[g_i]$  is the  $N \times 1$  voltage vector and  $[c_j]$  is the  $N \times 1$  unknown current vector. The elements of the matrix system in Equation 3.64 is shown below.

$$[c_j] = [c_1 c_2 \dots c_N]^T \quad j = 1, 2, 3, \dots, N \quad (3.65)$$

$$[g_i] = \langle g, w_i \rangle = \int_C w_i g dl \quad i = 1, 2, 3, \dots, N \quad (3.66)$$

$$[Z_{ij}] = \langle \mathcal{L}f_j, w_i \rangle = \int_C w_i \mathcal{L}f_j dl \quad i, j = 1, 2, 3, \dots, N \quad (3.67)$$

By using Equations 3.65-3.67, the matrix system in Equation 3.64 can be expressed as Equation 3.68.

$$\begin{bmatrix} \langle \mathcal{L}f_1, w_1 \rangle & \cdots & \langle \mathcal{L}f_N, w_1 \rangle \\ \vdots & \ddots & \vdots \\ \langle \mathcal{L}f_1, w_N \rangle & \cdots & \langle \mathcal{L}f_N, w_N \rangle \end{bmatrix} \begin{bmatrix} c_1 \\ \vdots \\ c_N \end{bmatrix} = \begin{bmatrix} \langle g, w_1 \rangle \\ \vdots \\ \langle g, w_N \rangle \end{bmatrix} \quad (3.68)$$

In the MoM matrix equation, each unknown interacts with the others and Equation 3.68 results in a full matrix system. Thus, each entry in the matrix must be stored in memory and computational load increases for larger problems.

### 3.6.1 Pulse basis function

Basis functions are classified as entire domain basis functions and subdomain basis functions by means of the region over which they are defined. Subdomain basis functions are more flexible and convenient for rough surface geometries. Moreover, they reduce the numerical implementation time because of the smaller integration domain. In this study, the basis functions are chosen as pulses or piecewise constant functions defined by

$$f_j(x') = \begin{cases} 1 & x'_{j-1} \leq x' \leq x'_j \\ 0 & \text{elsewhere} \end{cases} \quad (3.69)$$

Moreover, this subdomain approach is illustrated in Figure 3.6.

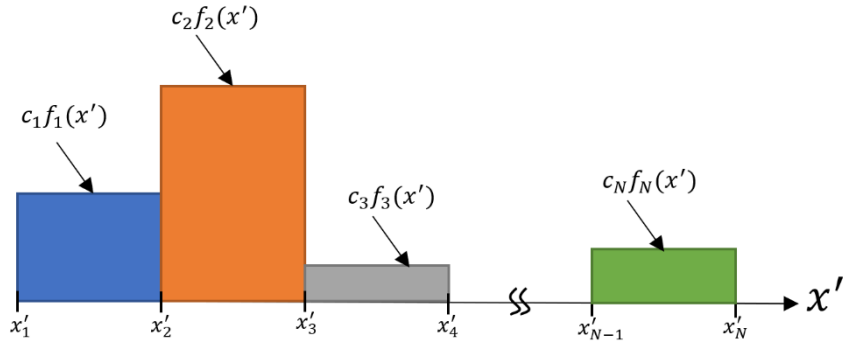


Figure 3.6. Pulse Basis Function

### 3.6.2 Point Matching

If the weighting function is chosen as Dirac Delta function (i.e., impulse function) the approach is called point matching or collocation method.

$$w_i(x) = \delta(x - x_i) \quad i = 1, 2, 3, \dots, N \quad (3.70)$$

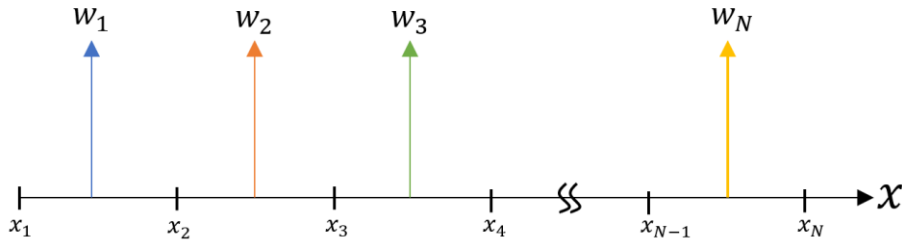


Figure 3.7. Point Matching Function

By using this method, one of the integrations is eliminated. Thus, this approach is preferred to decrease computational load of the sea surface scattering problem.

Applying point matching on the matrix elements  $[Z_{ij}]$ ,  $[g_i]$ , Equation 3.66 and Equation 3.67 are reorganized as,

$$[g_i] = \int_x \delta(x - x_i) g dx = g(x_i) \quad i = 1, 2, 3, \dots, N \quad (3.71)$$

$$[Z_{ij}] = \int_x \delta(x - x_i) \mathcal{L}f_j dx = \mathcal{L}f_j|_{x=x_i} \quad i, j = 1, 2, 3, \dots, N \quad (3.72)$$

### 3.7 Solutions of surface integral equations by using Method of Moments

In this section, MoM with pulse basis function and point matching is implemented to solve TM-EFIE and TE-MFIE that were previously derived. Then, by using the far field expressions, RCS and NRCS are evaluated in the post processing phase.

Before applying MoM to integral equations, the specified domain, which is sea surface in this case, should be discretized. Assume that the sea surface is discretized into  $N$  segments.

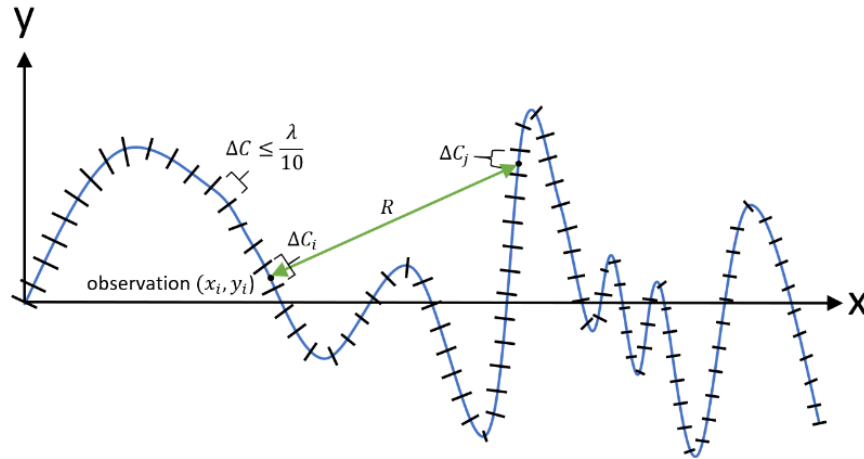


Figure 3.8. Sea surface domain discretization

Increasing the number of segments increases the resolution and accuracy of the numerical solution. However, the computational load increases in the order of  $O(N)$ [35]. Therefore, for a reasonable computational time and accuracy, segment size is chosen to be less than  $\lambda/20$ , which is less than  $\lambda/10$  which is the “crudest” segment size in the literature.

Moreover, segment sizes need not to be equal. In this study, the segment size is defined in Equation 2.19. Although the length  $\Delta x$  is the same for each segment, the

surface height difference  $\Delta y$  is changing randomly. Consequently, segment sizes differ from each other.

### 3.7.1 MoM solution of TM-EFIE and Postprocessing

The current density  $J_z(\bar{r}')$  in Equation 3.40 is approximated as a sum of pulse basis functions yielding Equation 3.73.

$$J_z(\bar{r}') \approx \sum_{j=1}^N c_j f_j(\bar{r}') \quad (3.73)$$

Then inserting Equation 3.73 into Equation 3.40, we get

$$\sum_{j=1}^N c_j \frac{k\eta_0}{4} \int_{\bar{r}' \in \Delta C'_j} f_j(\bar{r}') H_0^{(2)}(k|\bar{r} - \bar{r}'|) dl' = E_z^i(\bar{r}) \quad (3.74)$$

Since basis function  $f_j$  is pulse basis function over  $\Delta C'$ , Equation 3.74 can be modified as,

$$\sum_{j=1}^N c_j \frac{k\eta_0}{4} \int_{r'_{j-1}}^{r'_j} H_0^{(2)}(k|\bar{r} - \bar{r}'|) dl' = E_z^i(\bar{r}) \quad (3.75)$$

Then using the Dirac Delta function defined at the center point of each observation segment in Equation 3.76, N equations are obtained below.

$$\delta(\bar{r}_i) = \delta(x - x_i)\delta(y - y_i) \quad (3.76)$$

$$\sum_{j=1}^N c_j \frac{k\eta_0}{4} \int_{r'_{j-\frac{1}{2}}}^{r'_{j+\frac{1}{2}}} H_0^{(2)}(k|\bar{r}_i - \bar{r}'|) dl' = E_z^i(\bar{r}_i) \quad (3.77)$$

where  $\bar{r}_i(x_i, y_i)$  and  $\bar{r}_j(x_j, y_j)$  are the center points of each observation segment and source segment, respectively.

Moreover, inserting incident electric field defined in Equation 3.40 into Equation 3.77, the  $N \times N$  matrix system for MoM is formed.

$$\sum_{j=1}^N c_j \frac{k\eta_0}{4} \int_{r'_j - \frac{1}{2}}^{r'_j + \frac{1}{2}} H_0^{(2)}(k|\bar{r}_i - \bar{r}'|) dl' = e^{jk(x_i \cos\phi_i + y_i \sin\phi_i)} \quad (3.78)$$

The integration in Equation 3.78 can be handled by using numerical integration. In this case, 3-Point Simpson's Rule is used. A general description of this method is presented below.

$$\int_a^b f(x) dx = \frac{1}{6(b-a)} \left( f(a) + 4f\left(\frac{b-a}{2}\right) + f(b) \right) \quad (3.79)$$

Afterwards, Equation 3.78 can be rewritten by using the defined numerical integration method in Equation 3.79.

$$\sum_{j=1}^N c_j \frac{k\eta_0}{24\Delta C_j} \left[ H_0^{(2)}(kR_1) + 4H_0^{(2)}(kR_2) + H_0^{(2)}(kR_3) \right] = e^{jk(x_i \cos\phi_i + y_i \sin\phi_i)} \quad (3.80)$$

where  $R_1 = |\bar{r}_i - \bar{r}'_{j-1/2}|$ ,  $R_2 = |\bar{r}_i - \bar{r}'_j|$ , and  $R_3 = |\bar{r}_i - \bar{r}'_{j+1/2}|$  are depicted in Figure 3.9. Moreover, the entries of the matrix system  $[Z_{ij}][c_j] = [g_i]$  are described below.

$$[Z_{ij}] = \frac{k\eta_0}{24\Delta C_j} \left[ H_0^{(2)}(kR_1) + 4H_0^{(2)}(kR_2) + H_0^{(2)}(kR_3) \right] \text{ for } i \neq j \quad (3.81)$$

$$[g_i] = e^{jk(x_i \cos\phi_i + y_i \sin\phi_i)} \quad (3.82)$$

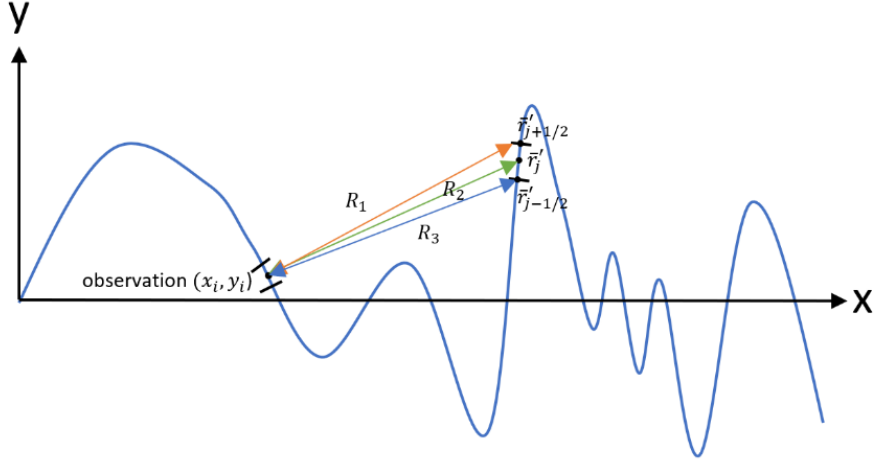


Figure 3.9. Representation of 3-Point Simpson's rule on sea surface

Equation 3.80 is only applicable to off-diagonal terms i.e.,  $i \neq j$ , since diagonal terms of impedance matrix  $[Z_{ij}]$  have an integrable singularity. To get rid of the singularity of Hankel function for  $i = j$  the following approximations are applied. From [34], Hankel Function in terms of Bessel functions of the first and second kinds and their approximate values for  $R \rightarrow 0$ , are given below.

$$H_0^{(2)}(kR) = J_0(kR) - jY_0(kR) \quad (3.83)$$

$$H_0^{(2)}(kR) \approx 1 - j \frac{2}{\pi} \ln\left(\frac{\gamma kR}{2}\right) \quad R \rightarrow 0 \quad (3.84)$$

Then the integral in Equation 3.78 for  $i = j$ , is obtained as

$$[Z_{jj}] \approx \frac{k\eta_0}{4} \int_{r'_{j-\frac{1}{2}}}^{r'_{j+\frac{1}{2}}} 1 - j \frac{2}{\pi} \ln\left(\frac{\gamma kR}{2}\right) dR = \frac{k\eta_0}{2} \int_0^{\frac{\Delta C_j}{2}} 1 - j \frac{2}{\pi} \ln\left(\frac{\gamma kR}{2}\right) dR \quad (3.85)$$

$$[Z_{jj}] \approx \frac{k\eta_0}{4} \Delta C_j \left\{ 1 - j \frac{2}{\pi} \left[ \ln\left(\frac{\gamma kR}{4e}\right) \right] \right\} \quad (3.86)$$

After finding the unknown coefficients  $[c_j]$ , the corresponding induced current density on the surface is evaluated. In the postprocessing part, far field radiation

integrals can be found by using Equation 3.38 and moving the observation point to the far field where far field distance is given by [37],

$$r \geq \frac{2D^2}{\lambda} \quad (3.87)$$

where  $D$  is the largest dimension of antenna.

Moreover, far field approximation [34] can be applied to the Hankel function.

$$H_0^{(2)}(kR) \approx \sqrt{\frac{2}{\pi kR}} e^{-j[kR - \frac{\pi}{4}]} \quad kR \rightarrow \infty \quad (3.88)$$

Then the amplitude and phase terms in Equation 3.88, can be written as follows,

$$R \approx r \quad (\text{in amplitude}) \quad (3.89)$$

$$R = r - x' \cos \phi_{obs} - y' \sin \phi_{obs} \quad (\text{in phase}) \quad (3.90)$$

where  $\phi_{obs}$  is the observation angle with respect to the x axis at the far field.

Inserting Equations 3.88-3.90 into Equation 3.38, scattered field at the far field is found.

$$E_z^S(\vec{r}) = \frac{-k\eta_0}{4} \int_{C'} J_z(\vec{r}') \sqrt{\frac{2}{\pi kr}} e^{-j[k(r - x' \cos \phi_{obs} - y' \sin \phi_{obs}) - \frac{\pi}{4}]} dl' \quad kR \rightarrow \infty \quad (3.91)$$

Since, the surface current density is already found from Equation 3.73, scattered electric field in Equation 3.91 can be rewritten as,

$$E_z^S(\vec{r}) = \frac{k\eta_0}{\sqrt{8\pi kr}} e^{-j(kr + \frac{3\pi}{4})} \left[ \sum_{j=1}^N c_j e^{jk(x_j \cos \phi_{obs} + y_j \sin \phi_{obs})} \Delta C_j \right] \quad kR \rightarrow \infty \quad (3.92)$$

Furthermore, RCS and NRCS can be derived by using the far field electric field expression as follows.

$$\sigma = 2\pi r \frac{|\Psi_{far}^s|^2}{|\Psi_i|^2} \quad (3.93)$$

$$\sigma^0 = \frac{2\pi r}{L} \frac{|\Psi_{far}^s|^2}{|\Psi_i|^2} \quad (3.94)$$

where  $\Psi$  is the  $E_z$  for  $TM_z$  case and  $H_z$  for  $TE_z$  case.

Since sea clutter is a backscattering problem,  $\phi_i = \phi_{obs}$ , and substituting Equation 3.92 into Equation 3.94, with incident field which has unity magnitude, yields

$$\sigma_{TM}^0 = \frac{k\eta_0^2}{4L} \left| \sum_{j=1}^N c_j e^{jk(x_j \cos\phi_i + y_j \sin\phi_i)} \Delta C_j \right|^2 \quad (3.95)$$

### 3.7.2 MoM solution of TE-MFIE and Postprocessing

Similar to the approach given in the previous section, pulse basis functions and point matching will be applied to TE-MFIE in Equation 3.54.

First, consider the pulse basis implementation,

$$J_{C'}(\bar{r}') \approx \sum_{j=1}^N c_j f_j(\bar{r}') \quad (3.96)$$

where  $f_j$  is the pulse basis function defined over each segment. Then, approximated surface current density is substituted into Equation 3.54 to obtain

$$\sum_{j=1}^N c_j + \left\{ \sum_{j=1}^N c_j \frac{jk}{4} \int_{\bar{r}' \in \Delta C_j'} H_1^{(2)}(k|\bar{r} - \bar{r}'|) \cos(\psi_j') dl' \right\} = -H_z^i(\bar{r}) \quad (3.97)$$

Second, we can apply Dirac Delta weighting function at the middle point of each observation segment in Equation 3.76 to both sides of Equation 3.97.

$$\sum_{j=1}^N c_j \delta(x - x_i) \delta(y - y_i) + \left\{ \sum_{j=1}^N c_j \frac{jk}{4} \int_{\bar{r}' \in \Delta C_j'} H_1^{(2)}(k|\bar{r}_i - \bar{r}'|) \cos(\psi'_{ij}) dl' \right\} = -H_z^i(\bar{r}_i) \quad (3.98)$$

Consider that the incident magnetic field has unity magnitude

$$H_z^i(\bar{r}_i) = e^{-j\bar{k} \cdot \bar{r}_i} = e^{jk(x \cos \phi_i + y \sin \phi_i)} \quad (3.99)$$

Then  $N \times N$  matrix system for TE-MFIE is obtained below.

$$\sum_{j=1}^N c_j \delta(x - x_i) \delta(y - y_i) + \left\{ \sum_{j=1}^N c_j \frac{jk}{4} \int_{\bar{r}' \in \Delta C_j'} H_1^{(2)}(k|\bar{r}_i - \bar{r}'|) \cos(\psi'_{ij}) dl' \right\} = -e^{jk(x_i \cos \phi_i + y_i \sin \phi_i)} \quad (3.100)$$

The off diagonal ( $i \neq j$ ) term of the impedance matrix is

$$[Z_{ij}] = \frac{jk}{4} \int_{\bar{r}' \in \Delta C_j'} H_1^{(2)}(k|\bar{r}_i - \bar{r}'|) \cos(\psi'_{ij}) dl' \quad (3.101)$$

Since each segment is represented by a straight line, the scattering problem is illustrated within a thin rectangular box in Figure 3.10. [34]

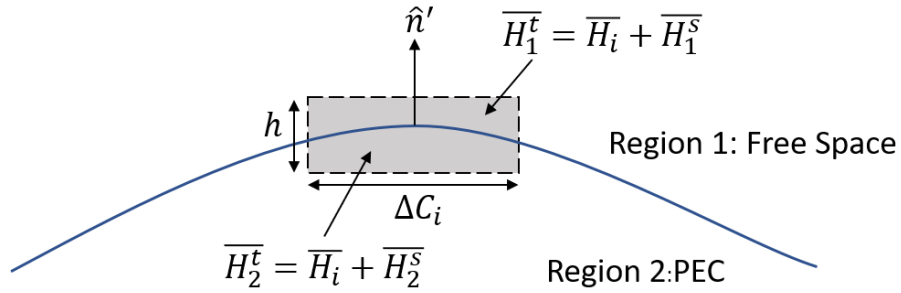


Figure 3.10. The geometry and the fields along the scattering surface

In Figure 3.10, the total field in both regions is written as the sum of incident and scattered fields and the scattered field is considered in terms of diagonal and off-diagonal segments. Then, the total magnetic fields are written as,

$$\overline{H}_1^t = \overline{H}_i + \overline{H}_{1a}^s + \overline{H}_{1b}^s \text{ and } \overline{H}_2^t = \overline{H}_i + \overline{H}_{2a}^s + \overline{H}_{2b}^s = 0 \quad (3.102)$$

where  $\overline{H}_{1a}^s$  and  $\overline{H}_{2a}^s$  are scattered magnetic fields due to the surface current density in off-diagonal segments and  $\overline{H}_{1b}^s$  and  $\overline{H}_{2b}^s$  are scattered magnetic field due to the surface current density in diagonal segment. The total magnetic field should be zero inside the PEC, and outside the PEC it should be non-zero. Moreover, because of the surface current density induced within the box, discontinuity in total magnetic field is occurred. Consequently,  $\overline{H}_{1a}^s = \overline{H}_{2a}^s$  are continuous fields and  $\overline{H}_{1b}^s = -\overline{H}_{2b}^s$  are discontinuous terms.

As the thickness of rectangular box in Figure 3.10 goes to zero ( $h \rightarrow 0$ ), boundary condition in Equation 3.10 can be applied by using Equation 3.102 as,

$$\begin{aligned} \hat{c}' J_{C'} &= \hat{n}' \times (\overline{H}_1^t - \overline{H}_2^t) = \hat{n}' \times (\overline{H}_i + \overline{H}_{1a}^s + \overline{H}_{1b}^s - \overline{H}_i - \overline{H}_{2a}^s - \overline{H}_{2b}^s) \\ &= 2\hat{n}' \times \overline{H}_{2b}^s \end{aligned} \quad (3.103)$$

Alternatively, the scattered magnetic field is written in terms of the surface current density shown below.

$$\hat{c}' J_{C'} = -2\hat{c}' H_{2b}^s \Rightarrow H_{2b}^s = \frac{-J_{C'}}{2} \quad (3.104)$$

Therefore, the diagonal term is formulated as,

$$[Z_{jj}] = 1 - \frac{1}{2} = \frac{1}{2} \quad (3.105)$$

After solving the matrix system for the unknown surface current density, postprocessing can be applied in a similar manner with the TM case. First, the far field scattered magnetic field should be found by using the far field approximations.

$$\lim_{kR \rightarrow \infty} H_1^{(2)}(kR) \approx \sqrt{\frac{2}{\pi kR}} e^{-j(kR - \frac{\pi}{2} - \frac{\pi}{4})} \quad kR \rightarrow \infty \quad (3.106)$$

$$\frac{-jk}{4} \int_{c'} J_{c'}(\bar{r}') H_1^{(2)}(kR) \left( \sin \theta' \frac{(x - x')}{R} - \cos \theta' \frac{(y - y')}{R} \right) dl' \quad kR \rightarrow \infty \quad (3.107)$$

$$H_z^s(\bar{r}) = \frac{-jk}{4} \sqrt{\frac{2}{\pi kR}} e^{-j(kR - \frac{3\pi}{4})} \times \sum_{j=1}^N c_j e^{jk(x_j \cos(\phi) + y_j \sin(\phi))} (\sin(\theta_j) \cos(\phi_{obs}) - \cos(\theta_j) \sin(\phi_{obs})) \Delta C_j \quad (3.108)$$

Then, RCS and NRCS for TE case are formulated by inserting Equation 3.108 into Equation 3.94 where  $\phi_{obs} = \phi_{inc}$  and  $|H_z^i|^2 = 1$ .

$$\sigma_{TE}^0 = \frac{k}{4L} \times \left| \sum_{j=1}^N c_j e^{jk(x_j \cos(\phi_{inc}) + y_j \sin(\phi_{inc}))} (\sin(\theta_j) \cos(\phi_{inc}) - \cos(\theta_j) \sin(\phi_{inc})) \Delta C_j \right|^2 \quad (3.109)$$

### 3.8 Incident Field Tapering

Since the integral equation is solved over a finite surface, edge effects must be handled properly. In order to avoid the unwanted edge diffraction, incident field tapering is applied.

In the formulation of EFIE-TM and MFIE-TE, incident field is considered in the form of a plane wave  $e^{jk(x_i \cos \phi_i + y_i \sin \phi_i)}$  which has a unity amplitude. These incident fields can be multiplied with a window function to achieve decay close to

the edges. To illustrate incident field tapering on the surface of the scatterer, Figure 3.11 is given

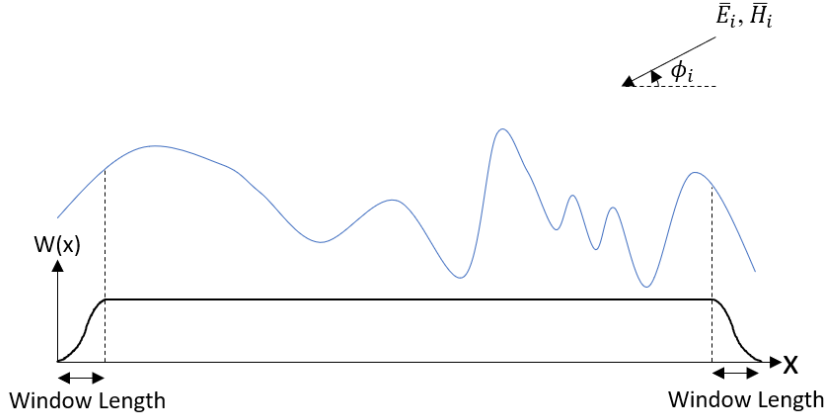


Figure 3.11. Illustration of incident field tapering

In this work, Hanning window [38] is used. Formulation of Hanning window is given in Equation 3.110.

$$w(n) = 0.5 \left( 1 - \cos \left( 2\pi \frac{n}{N} \right) \right) \quad 0 \leq n \leq N \quad (3.110)$$

where window length is  $L = N + 1$  and physical window length in Figure 3.11 is described as,

$$Window\ length = \sum_{n=1}^N \Delta x_n \quad (3.111)$$

Size of the window length does not much affect the results by choosing the length in between  $1\lambda$  and  $2\lambda$ , providing a smooth decay in the fields [24]. In this work, the window length is chosen as  $1.5\lambda$ .

## CHAPTER 4

### EMPIRICAL AND STATISTICAL SEA CLUTTER MODELS

Because of the random nature of the sea clutter, amplitude characterization of sea clutter could be time consuming relative to electromagnetic analysis. For this reason, researchers have developed empirical models by using the measurement results. These models have been developed either to handle the average value of NRCS and of evaluate the probability distribution of NRCS from many measurement results. In this chapter, first empirical models are presented which focus on the average NRCS for low grazing angles. Then, some of the statistical distributions to model sea clutter are given.

#### 4.1 Empirical Sea Clutter Models

Since, NRCS depends on wind velocity, grazing angle, polarization and radar frequency, empirical sea clutter models are developed with respect to these parameters. Nathanson et. al. tabulated the mean value of NRCS from the results corresponding to 60 different sources [2]. These tables are widely used for NRCS calculation, and they are still including the most complete database in literature. However, they lack information below 500MHz and grazing angles except those for which measurements are taken. In this study, sea clutter is modeled for RADAR frequencies up to 500MHz. In this sense, Nathanson table is shown below for 500MHz in Table 4.1.

Table 4.1 NRCS in dB for 500MHz (UHF) from Nathanson Tables

Sea State	Polarization	Grazing angle					
		0.1°	0.3°	1.0°	3.0°	10°	30°
0	Vertical						
	Horizontal			-86	-75		
1	Vertical			-70	-60	-38	-38
	Horizontal			-84	-70		
2	Vertical	-90	-80	-63	-53	-35	-30
	Horizontal	-95	-78	-82	-66	-54	-42
3	Vertical	-88	-78	-58	-43	-34	-28
	Horizontal	-90		-73	-61	-50	-40
4	Vertical	-85	-75	-58	-38	-32	-28
	Horizontal			-63	-54	-48	-38
5	Vertical	-80	-73		-40	-30	-28
	Horizontal			-60	-53	-46	-35
6	Vertical					-30	-25
	Horizontal					-44	-33

As the grazing angle increases measurement error decreases from 8dB to 3dB. The measurements are taken from a monostatic Radar with 0.5 to 10 us pulse lengths. Assuming that rectangular pulses are used, illuminated length is calculated in between 75m and 1732.1 m by using Equation 1.5.

From Table 4.1, following conclusions can be drawn,

- As the grazing angle increases, sea clutter reflectivity increases
- As the sea state increases, sea clutter reflectivity increases

- At the same sea state and grazing angle, vertical polarization has greater NRCS than the horizontal polarization.

In addition to Nathanson's Tables, empirical models developed for low grazing angles are presented in this chapter. Then, these models are compared to each other and a relatively new one among them which is the Modified NRL model is used in the rest of the study.

In this chapter formulation of these models are given for lower frequencies for the sake of simplicity.

#### 4.1.1 GIT Model

Horst et. al. proposed an empirical sea clutter model [3] which is called Georgia Institute of Technology (GIT) model covering 1GHz to 100GHz and angles in between  $0.1^\circ$  and  $10^\circ$ . It is based on the observations obtained under non-ducting conditions. The GIT model consists of three terms, sea state term  $A_w$ , a multipath term  $A_i$ , and sea direction term  $A_u$  which are given below.

$$A_w = \left[ \frac{1.94 V_w}{1 + \frac{V_w}{15.4}} \right]^{1.1(\lambda + 0.015)^{-0.4}} \quad (4.1)$$

$$A_i = \frac{\sigma_\phi^4}{1 + \sigma_\phi^4} \quad (4.2)$$

where  $\sigma_\phi$  is the surface roughness parameter formulated in Equation 4.3.

$$\sigma_\phi = (14.4\lambda + 5.5) \frac{\phi_{gr} h_a}{\lambda} \quad (4.3)$$

where  $\phi_{gr}$  is grazing angle in radians. Sea direction term is formulated for Horizontal polarization as shown below.

$$A_u = \exp [0.2 \cos \varphi (1 - 2.8\phi_{gr})(\lambda + 0.015)^{-0.4}] \quad (4.4)$$

where  $\varphi$  is the angle between Radar boresight and wind direction. For  $\varphi = 0$ , Radar is looking in upwind direction. Then, by using combination of three components described above, average NRCS for Horizontal polarization can be written as,

$$\sigma_0^H = 3.9 \times 10^{-6} \lambda \phi_{gr}^{0.4} A_i A_u A_w \quad (4.5)$$

where  $\phi_{gr}^{0.4}$  term stands for compensating the shadowing effect.

Then, vertical polarization NRCS is formulated in terms of horizontal polarization NRCS as,

$$\sigma_0^V = 9.33 (h_a + 0.015)^{-0.24} \lambda^{0.25} (\phi_{gr} + 0.0001)^{0.29} \sigma_0^H \quad f \geq 3 \text{ GHz} \quad (4.6)$$

#### 4.1.2 The Hybrid Model

Hybrid model is developed by Reilly and Dockery [4] and it agrees with GIT model and Nathanson's data. It can be used for Radar frequencies from 0.5GHz to 35 GHz and grazing angles in between  $0.1^\circ$  and  $30^\circ$ . In this model, evaporation duct effect is included. Hybrid model formulation is expressed below [1].

$$\sigma_0 = \sigma_0(ref) + K_g + K_s + K_p + K_d \quad (4.7)$$

Where  $\sigma_0(ref)$  is a reference reflectivity applying to sea state 5, grazing angle  $0.1^\circ$ , look direction upwind ( $\varphi = 0^\circ$ ), and vertical polarization.  $K_g, K_s, K_p, K_d$  are adjustment factors for grazing angle, sea state, polarization, and wind direction respectively. The reference reflectivity defined as a function of frequency  $f$  in Hertz shown below.

$$\sigma_0(ref) = 22.4 \log f - 266.8 \quad f \leq 12.5 \text{ GHz} \quad (4.8)$$

$K_g$  is adjustment factor changing with grazing angle  $\phi_{gr}$  and formulated in terms of reference grazing angle  $\phi_{gr}(ref) = 0.1^\circ$ , grazing angle  $\phi_{gr}$  and transition angle  $\phi_{tr} = \sin^{-1}(0.66\lambda/h_{RMS})$

- For  $\phi_{tr} \geq \phi_{gr}(ref)$

$$K_g = \begin{cases} 0 & \text{for } \phi_{gr} < \phi_{gr}(ref) \\ 20 \log \left( \frac{\phi_{gr}}{\phi_{gr}(ref)} \right) & \text{for } \phi_{gr}(ref) < \phi_{gr} < \phi_{tr} \\ 20 \log(\phi_{tr}/\phi_{gr}(ref)) + 10 \log(\phi_{gr}/\phi_{tr}) & \text{for } \phi_{tr} < \phi_{gr} < 30^\circ \end{cases} \quad (4.9)$$

- For  $\phi_{tr} < \phi_{gr}(ref)$

$$K_g = \begin{cases} 0 & \text{for } \phi_{gr} \leq \phi_{gr}(ref) \\ 10 \log \left( \frac{\phi_{gr}}{\phi_{gr}(ref)} \right) & \text{for } \phi_{gr} > \phi_{gr}(ref) \end{cases} \quad (4.10)$$

Sea state adjustment term  $K_s$  is defined as,

$$K_s = 5(SS - 5) \quad (4.11)$$

For sea states 1 and 2 and horizontal polarization case  $K_s$  is corrected as,

$$K_s = 5(SS - 5) + \frac{(SS - 5)^3}{10} \quad (4.12)$$

Polarization adjustment  $K_p$  is only valid for horizontal polarization given below.

$$K_p = 1.7 \ln(h_{av} + 0.015) - 3.8 \ln \lambda - 2.5 \ln(\phi_{gr} + 0.0001) - 22.2 \quad f < 3 \text{ GHz} \quad (4.13)$$

The wind adjustment factor is given as,

$$K_d = \left( 2 + 1.7 \log \left( \frac{0.1}{\lambda} \right) \right) (\cos \varphi - 1) \quad (4.14)$$

### 4.1.3 The TSC Model

The TSC model is based on Nathanson's Data and this model includes the ducting conditions. It is valid in between 0.5GHz and 35GHz and grazing angles from 0° to 10°. Formulation of TSC is presented below [5].

$$\sigma_0^H = 10 \log \left( \frac{1.7 \times 10^{-5} \phi_{gr}^{0.5} G_u G_W G_A}{(3.2808\lambda + 0.05)^{1.8}} \right) \quad (4.15)$$

For vertical polarization NRCS can be written in terms of horizontal polarization NRCS for frequencies less than 2GHz.

$$\sigma_0^V = \sigma_0^H - 1.73 \ln(8.225\sigma_z + 0.05) + 3.76 \ln \lambda + 2.46 \ln(\sin \phi_{gr} + 0.0001) + 24.2672 \quad (4.16)$$

The parameters defined in Equation 4.15 and 4.16 are given below.

$$\begin{aligned} \sigma_z &= 0.03505 SS^{1.95}, \sigma_a = 4.5416 \phi_{gr} (3.2808\sigma_z + 0.25)/\lambda, G_A = \frac{\sigma_a^{1.5}}{1+\sigma_a^{1.5}}, \\ Q &= \phi_{gr}^{0.8}, A_1 = \left(1 + \left(\frac{\lambda}{0.00914}\right)^3\right)^{0.1}, A_2 = \left(1 + \left(\frac{\lambda}{0.00305}\right)^3\right)^{0.1}, \\ A_3 &= \left(1 + \left(\frac{\lambda}{0.00914}\right)^3\right)^{Q/3} \\ A_4 &= 1 + 0.35Q, A = 2.63A_1/(A_2A_3A_4), G_W = \left[\frac{1.9438V_w+4}{15}\right]^A \\ G_u &= \exp\left(0.3\cos\varphi \left(\frac{\exp\left(\frac{-\phi_{gr}}{0.17}\right)}{(10.7636\lambda^2 + 0.005)^{0.2}}\right)\right) \end{aligned} \quad (4.17)$$

#### 4.1.4 The NRL Model

Since GIT Model, Hybrid Model and TSC Model have large average error compared to Nathanson's Data, Gregers-Hansen and Mital [6] proposed NRL model. This model is valid between 0.5GHz and 35GHz and grazing angles from 0° to 10°. The optimized NRCS calculation according to the Nathanson's Data is shown below.

$$\sigma_0^{dB} = c_1 + c_2 \log(\sin(\phi_{gr})) + \frac{(c_3 + c_4 \phi_{gr}) \log f}{1 + c_5 \phi_{gr} + c_6 SS} + c_7 (1 + SS)^{\frac{1}{2+c_8 \phi_{gr}+c_9 SS}} \quad (4.18)$$

where  $f$  is the Radar frequency in GHz,  $\phi_{gr}$  grazing angle in degrees and constants given in Equation 4.18 are tabulated for both polarizations below.

Table 4.2 Parameters for the NRL clutter model

Parameter	Horizontal Polarization	Vertical Polarization
$c_1$	-72.76	-48.56
$c_2$	21.11	26.30
$c_3$	24.78	29.05
$c_4$	281.7	-29.70
$c_5$	35.62	60.56
$c_6$	-0.02949	0.04839
$c_7$	26.19	21.37
$c_8$	5.354	4.278
$c_9$	0.05031	0.04623

The main advantage of this model over the GIT model is that it provides more agreement with Nathanson's Data for low sea states. The GIT model underestimates the NRCS for lower sea states.

Moreover, a comparison between GIT model, Hybrid Model, TSC model and NRL model in terms of Average Absolute Error with respect to Nathanson's Data for  $0.3^\circ$  grazing angle is given below.[6]

Table 4.3 Comparison of Models for  $0.3^\circ$  grazing angle

Model	Polarization	
	Horizontal	Vertical
GIT Model	13.7dB	14.1dB
Hybrid Model	14.5dB	8.7dB
TSC Model	7.92dB	10.1dB
NRL Model	2.1dB	2.0dB

According to Table 4.3 NRL model is superior to the other models for both polarizations.

#### 4.1.5 Modified NRL Model

The NRL model is modified [7] by Gregers-Hansen and Mital, one year after the original model. This model covers frequencies between 100MHz and 35GHz and grazing angles up to 60°. Thus, it provides more information about frequency and grazing angle range than the original work.

$$\sigma_0^{dB} = c_1 + c_2 \log(\sin(\phi_{gr})) + \frac{(27.5 + c_3 \phi_{gr}) \log(f)}{1 + 0.95 \phi_{gr}} + c_4 (1 + SS)^{\frac{1}{2+0.085\phi_{gr}+0.033SS}} + c_5 \phi_{gr}^2 \quad (4.19)$$

Table 4.4 Parameters for the Modified NRL clutter model

Parameter	Horizontal Polarization	Vertical Polarization
$c_1$	-73	-50.79
$c_2$	20.78	25.93
$c_3$	7.351	0.7093
$c_4$	25.65	21.58
$c_5$	0.0054	0.00211

Another comparison between GIT model, Hybrid Model, TSC model and NRL model in terms of Average Absolute Deviation Error with respect to Nathanson's Data is given below.[7]

Table 4.5 Comparison of Models for 10° grazing angle

Model	Polarization	
	Horizontal	Vertical
GIT Model	13.4dB	12dB
Hybrid Model	14.5dB	8.7dB
TSC Model	7.9dB	10.1dB
Modified NRL Model	2.3dB	2.2dB

Because both NRL models show better agreement with Nathanson's Data, and modified NRL model provides information the frequency range from 100MHz to

500MHz, modified NRL model is used in this thesis for comparison. NRCS vs. grazing angle graphs for both polarizations at 100MHz are given in Figure 4.1 and Figure 4.2, respectively.

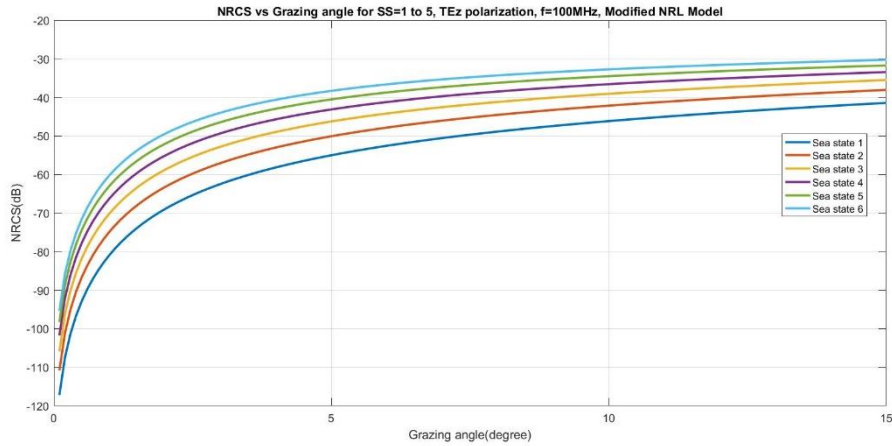


Figure 4.1. NRCS vs. Grazing angle graph for TEz polarization at 100MHz

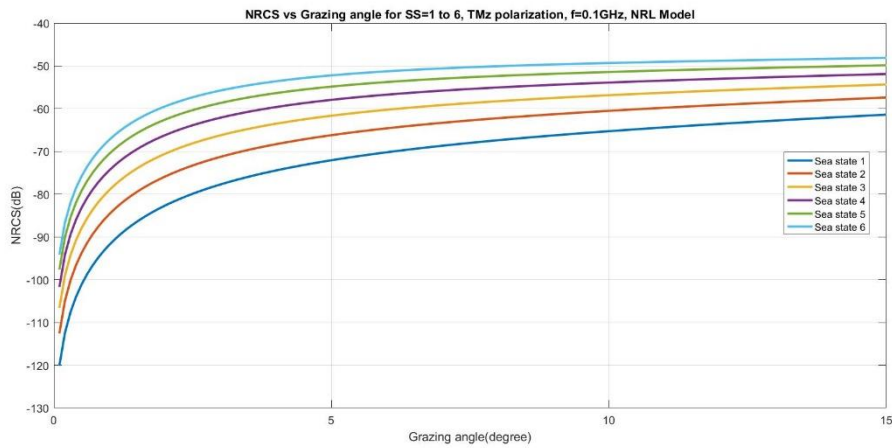


Figure 4.2. NRCS vs. Grazing angle graph for TMz polarization at 100MHz

## 4.2 Statistical Sea Clutter Models

Amplitude probability distribution of sea clutter has great importance for radar designers to estimate probability of detection and probability of false alarm accurately. For this reason, some of the amplitude distributions of sea clutter which

is specified with NRCS ( $\sigma_0$ ) in terms of probability density function (PDF) and their properties are given in this chapter.

#### 4.2.1 Rayleigh distribution

At the early stages of the modelling of amplitude distribution of sea clutter, Rayleigh distribution is widely used. However, this distribution is only valid for low resolution or coarse radars and grazing angles greater than  $10^\circ$ . Therefore, additional distribution models are required with increasing radar resolution and low grazing angles.

Assuming that backscattering from sea surface is modeled as the superposition of returns from independent, random scatterers, amplitude fluctuations of sea clutter can be described in terms of a gaussian probability density function [22]. Therefore, there are no sea spikes observed but speckle is the dominant component in amplitude distribution of sea clutter. PDF of sea clutter amplitude is given in Equation 4.20 in terms of Rayleigh distribution. [12]

$$p(v) = \frac{2v}{\mu} \exp\left(\frac{-v^2}{\mu}\right); \quad 0 \leq v \leq \infty \quad (4.20)$$

Where  $v$  is the envelope of the sea clutter detected from linear detector, the mean  $\langle v \rangle = \frac{\sqrt{\pi\mu}}{2}$  and the mean square  $\langle v^2 \rangle = \mu$  which is also clutter mean power. Consequently, the PDF of power of the returns, which is proportional with the NRCS, is given by exponential distribution function below.

$$p(\sigma_0) = \frac{1}{\mu} \exp\left(\frac{-\sigma_0}{\mu}\right); \quad 0 \leq \sigma_0 \leq \infty \quad (4.21)$$

where  $\sigma_0 = v^2$  and  $\langle \sigma_0 \rangle = \mu$ .

### 4.2.2 Log-Normal Distribution

To model high resolution radars working at low grazing angles, spiky sea clutter distributions with wide dynamic ranges are used. In such a case, Log-Normal distribution can be used to model sea clutter statistics. Compared to Rayleigh distribution, Log-Normal model tends to overestimate the actual dynamic range of the clutter distribution. Thus, Log-Normal model represents the worst-case scenario compared to Rayleigh distribution which is the best case from the detection point of view. [8]

For Non-Rayleigh distribution, Log-Normal PDF of clutter power can be described in Equation 4.22.[9]

$$p(\sigma_0) = \frac{1}{\sigma_0 \sqrt{2\pi\sigma^2}} \exp\left(-\frac{(\ln \sigma_0 - \mu)^2}{2\sigma^2}\right), \sigma_0 \geq 0. \quad (4.22)$$

where  $\sigma$  is standard deviation of  $\ln \sigma_0$ ,  $\mu$  is mean of  $\ln \sigma_0$ , and  $\sigma^2$  is the variance of  $\ln \sigma_0$ .

### 4.2.3 Weibull Distribution

Weibull Distribution lies between Rayleigh and Log-Normal distributions. It is a two parameter PDF, which are the shape parameter  $c$  and scale parameter  $a$ . Choosing proper values of these parameters provides an accurate simulation of amplitude distribution. Moreover, similar results to Rayleigh and Log-Normal distributions can be obtained by adjusting Weibull parameters accordingly. Weibull PDF of NRCS is given in Equation 4.23.[10]

$$p(\sigma_0) = \frac{c}{a} \left(\frac{\sigma_0}{a}\right)^{c-1} \exp\left(-\left(\frac{\sigma_0}{a}\right)^c\right), \sigma_0 \geq 0. \quad (4.23)$$

For  $c = 2$ , Weibull distribution turns into a Rayleigh distribution. In addition, decreasing the shape parameter  $c$ , results in a spiky distribution and, Weibull distribution approaches to the Log-Normal distribution.

Because Weibull distribution is much more flexible compared to the Log-Normal and Rayleigh distributions, for modeling amplitude distribution of sea clutter Weibull distribution is fitted to the simulation results obtained from the MoM simulations.

## CHAPTER 5

### PROPOSED SEA CLUTTER MODEL AND SIMULATION RESULTS

In this chapter, the Monte Carlo approach is used for the statistical analysis of sea clutter. A set of random rough surfaces are generated from the Pierson-Moskowitz and Elfouhaily spectrum given in Chapter 2. After solving the scattering problem for each surface, NRCS results are formed as a random field by using MoM described in Chapter 3. Then, from these results, statistical behavior of sea clutter in terms of NRCS is extracted and compared with the empirical models discussed in Chapter 4. The algorithm used in the proposed model can be seen in Figure 5.1.

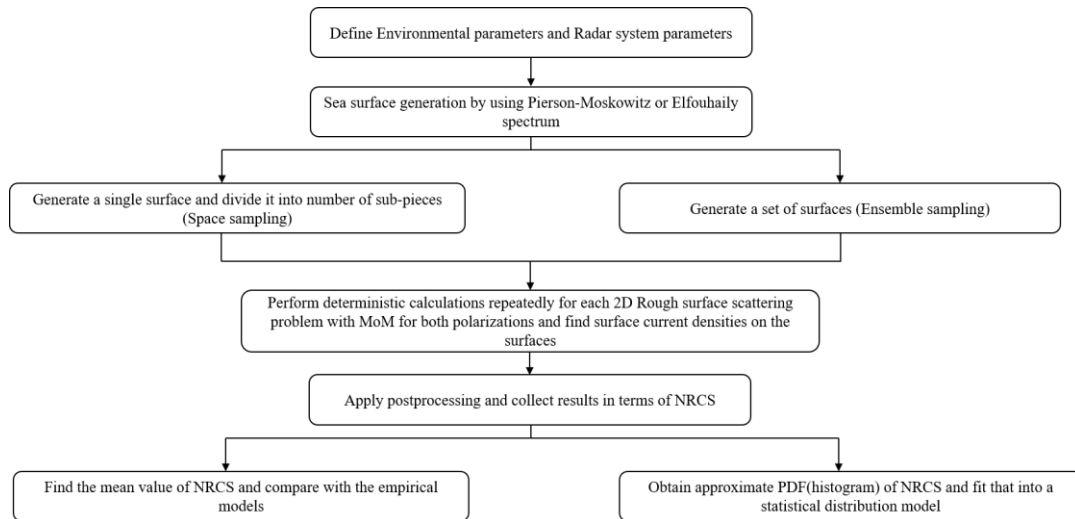


Figure 5.1. Algorithm of the proposed model

In Figure 5.1. detailed explanation of random field analysis with Monte Carlo method is explained [20]. Assume that  $M$  number of surfaces are generated randomly with either space or ensemble sampling. The problem is solved for each surface  $M$  times by using MoM. Consequently, a set of NRCS for  $N$  samples of low grazing angles in between  $0.1^\circ$  and  $15^\circ$  is obtained and expressed as a stochastic field as follows.

$$\begin{aligned}
\sigma_{0_1} &= [\sigma_{0_1^1}, \sigma_{0_2^1}, \dots, \sigma_{0_N^1}] \\
\sigma_{0_2} &= [\sigma_{0_1^2}, \sigma_{0_2^2}, \dots, \sigma_{0_N^2}] \\
&\vdots \\
\sigma_{0_M} &= [\sigma_{0_1^M}, \sigma_{0_2^M}, \dots, \sigma_{0_N^M}]
\end{aligned} \tag{5.1}$$

where the subscript represents the number of sample angle and the superscript represents the number of surfaces.

From the stochastic field defined in Equation 5.1., statistical parameters like mean ( $\mu_{\sigma_0}$ ) and standard deviation ( $\sigma_{\sigma_0}$ ), which is also called incoherent component, can be computed from set of NRCS at a specific angle (i-th sample) by using Equation 5.3 and 5.4, respectively.

$$\sigma_{0_i} = [\sigma_{0_i^1}, \sigma_{0_i^2}, \dots, \sigma_{0_i^M}] \tag{5.2}$$

$$\mu_{\sigma_0}(i) = \frac{1}{M} \sum_{j=1}^M \sigma_{0_i^j}, \quad i = 1, 2, \dots, N \tag{5.3}$$

$$\sigma_{\sigma_0} = \left[ \frac{1}{M} \sum_{j=1}^M (\sigma_{0_i^j} - \mu_{\sigma_0}(i))^2 \right]^{\frac{1}{2}}, \quad i = 1, 2, \dots, N \tag{5.4}$$

In this work, the mean value of NRCS is considered as magnitude of the clutter return power and it is evaluated to compare with the Empirical sea clutter models in Chapter 4.1. For this purpose, grazing angle vs. NRCS graphs for different Sea State conditions are plotted. Furthermore, approximate probability distributions are obtained from Equation 5.2 by using histograms. Then these approximate PDFs are fitted to the statistical sea clutter models given in Chapter 4.2. To form the histograms, the data collected at the Grazing angle vs. NRCS simulations at a specific grazing angle is used.

In this chapter, by using MoM given in Chapter 4, amplitude characterization of sea clutter is handled. Due to low grazing angles, sea surface is considered as PEC and

the region above the sea surface is considered as free space. Ducting effect is not included in calculations.

For horizontal polarization, EFIE-TM formulation given in Chapter 3.5.1 and for vertical polarization MFIE-TE formulation is used to solve 2D scattering problems and compute NRCS by using MoM.

MATLAB (MathWorks Inc.) R2016a is used to implement the proposed model algorithm with a computer including Windows 10-64Bit OS, AMD Ryzen 3 Pro Processor, and 16GB RAM. Because of the lack of processing speed and RAM storage, simulations are executed only for sub 500MHz radar frequencies.

### 5.1 Simulation results for $TM_z$ case with ensemble sampling

In this section, first 100 sea surfaces are generated by using Elfouhaily spectrum for NRCS calculation. Lengths of the generated surfaces and radar frequencies are specified as  $150m = 50\lambda$  for 100MHz,  $100m = 100\lambda$  for 300MHz and  $60m = 100\lambda$  for 500MHz. The number of points for FFT is chosen as  $N=1024$ . Thus, at least  $\frac{\lambda}{10}$  spatial grid resolution is satisfied for all three cases for the sake of accuracy of the MoM. To increase the accuracy of the simulations, incident field tapering is applied with a window length  $1.5\lambda$  for each case.

From Equation 1.5, the RADAR pulse bandwidths can be extracted by taking the pulse shape parameter as  $\alpha = 1$ , and  $\sec(\phi_{gr}) \cong 1$  for LGA,

$$B = \frac{c}{2L_c} \quad (5.5)$$

Thus, the resulting bandwidths for 150m, 100m and 60m are 1MHz, 1.5MHz and 2.5MHz, respectively.

Second, NRCS are calculated for each single surface realization for sea states 1 to 6 and grazing angles  $0.1^\circ$  to  $15^\circ$ . To increase the accuracy of the simulations, incident

field tapering is applied. Unless otherwise stated, all simulations are performed with these configurations.

### 5.1.1 $TM_z$ case simulation results for the mean amplitude of sea clutter with ensemble sampling

The results obtained from these simulations are used to form the average or mean value of NRCS to compare with Nathanson Tables and the modified NRL model. The comparative simulation results for this case are presented below.

For 500MHz and 60 meters length the mean NRCS vs. grazing angle graph is shown below.

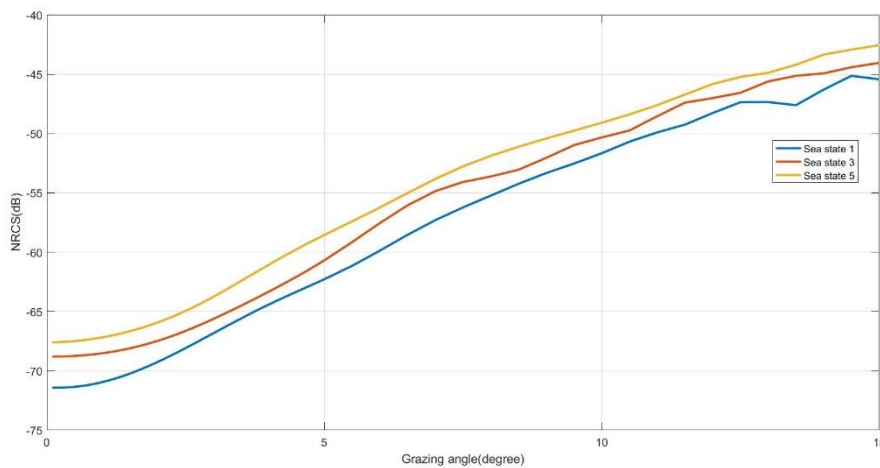


Figure 5.2.  $TM_z$  case mean NRCS vs. grazing angle graph for 500MHz, 60 meters length and sea states 1,3 and 5 by using Elfouhaily spectrum with Ensemble sampling

In Figure 5.2, as the sea state and wind speed increase the mean NRCS also increases. It is an expected result due to the increasing surface roughness with wind speed. Moreover, mean NRCS is also increasing with the grazing angle. Since LGA is at the interference region, sharp increase in NRCS in this region is observed.

Moreover, simulation results for sea state 2, 500MHz, and 60m length is compared with the modified NRL model and Nathanson table shown below.

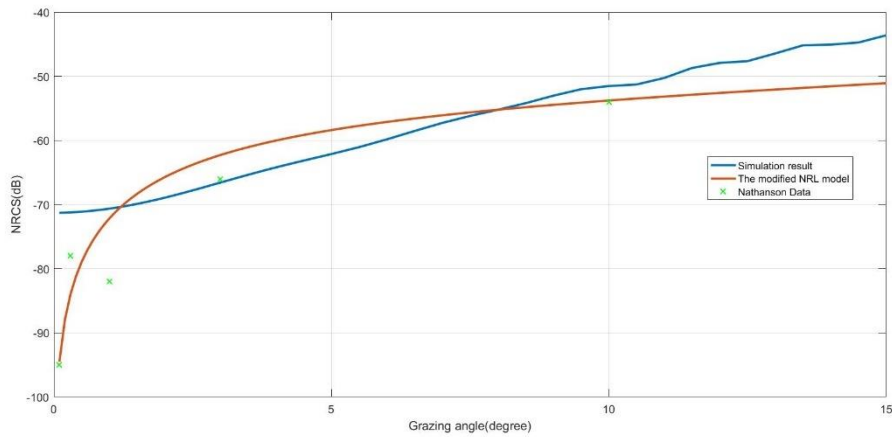


Figure 5.3.  $TM_z$  case mean NRCS vs. grazing angle graphs of simulation results, the modified NRL model and Nathanson's Table for 500 MHz, 60 meter length, Sea State 2 by using Elfouhaily spectrum with Ensemble sampling

Simulation results show a good agreement with the modified NRL model and Nathanson table for this case except the grazing angles below  $1^\circ$  and above  $10^\circ$ . Simulation result is overestimating the mean NRCS in these angles. However, the tendency with the changing grazing angle is similar to both models.

In addition, simulation results for 100MHz, 300MHz and 500MHz at sea state 4 are given below.

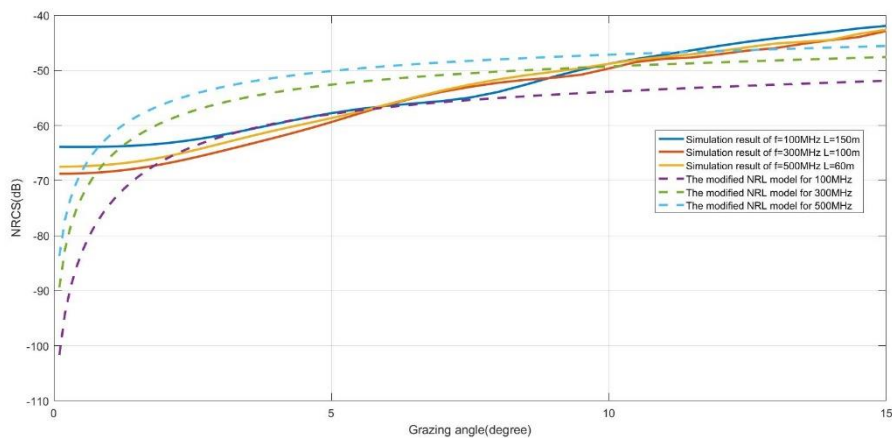


Figure 5.4.  $TM_z$  case mean NRCS vs. Grazing angle graph for 100MHz, 300MHz and 500MHz at Sea State 4 by using Elfouhaily spectrum with Ensemble sampling

According to the simulation results, increasing the frequency does not affect the mean NRCS significantly. However, according to the Nathanson's Tables [2], as the frequency increases the mean NRCS should also increase. Thus, there is a discrepancy between simulation results and modified NRL model.

As a final discussion on the mean amplitude of the sea clutter, Monte Carlo simulation is also applied by using the Pierson-Moskowitz spectrum in this section. Resulting NRCS vs. grazing angles for these simulations are given below. Note that, all other parameters like radar frequency, window length are unchanged.

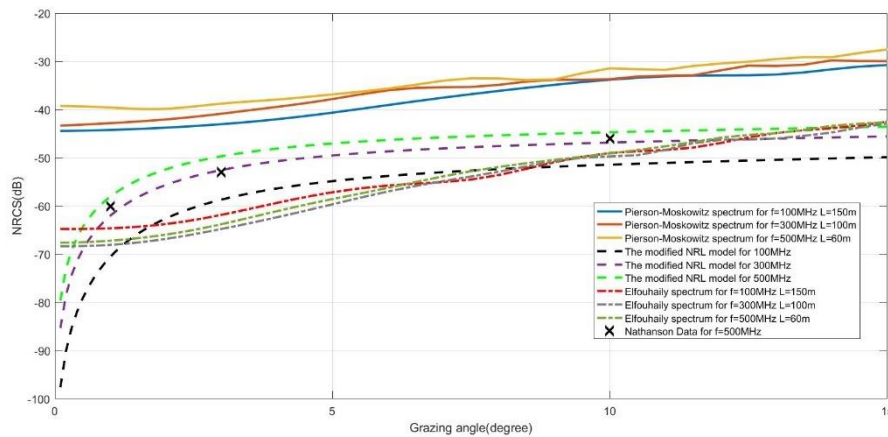


Figure 5.5  $TM_z$  case mean NRCS vs. grazing angle graph for Sea State 5 by using Pierson-Moskowitz spectrum and Elfouhaily spectrum with Ensemble sampling

Since PM spectrum is obtained in between 10m/s and 20m/s wind speeds, it is applied only for Sea States 5 and 6. Moreover, simulation results are not close to the results obtained from Nathanson Table, Modified NRL model and Elfouhaily spectrum. Consequently, Elfouhaily spectrum has a better agreement with the empirical models.

### 5.1.2 $TM_z$ case simulation results for amplitude distribution of sea clutter with ensemble sampling

In this section, the distribution of these amplitudes for a fixed grazing angle will be investigated. In addition, NRCS values are all calculated in units of m/m. Therefore, it is dimensionless.

First, Histograms and Weibull distributions of NRCS are given in Figure 5.6 for  $TM_z$  case 500MHz at Sea State 1 for several grazing angles. These distributions are obtained from surfaces generated by using Elfouhaily spectrum.

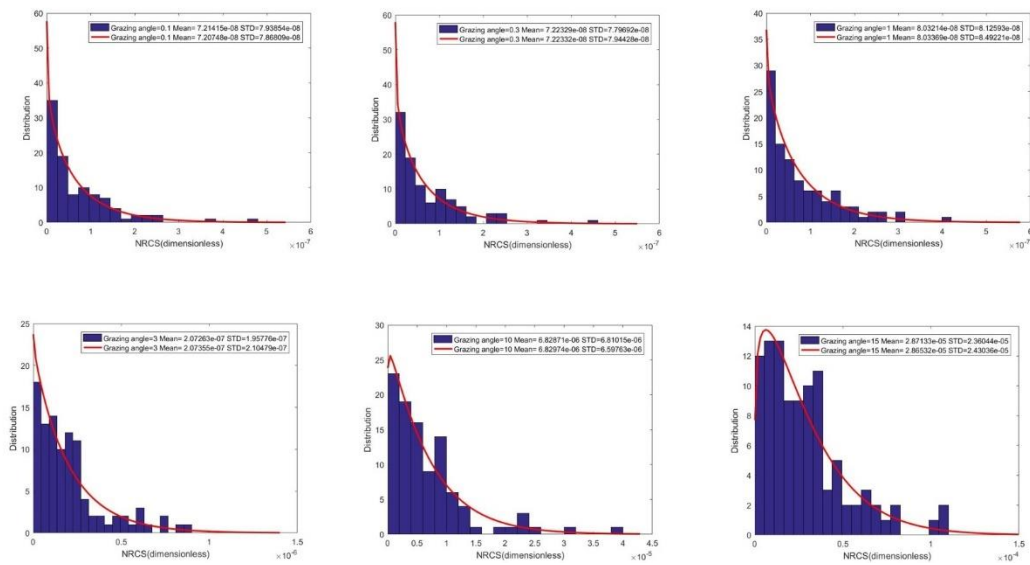


Figure 5.6.  $TM_z$  case Elfouhaily spectrum Histograms and Weibull distributions of NRCS at 500MHz for Sea State 1 with Ensemble sampling

In Figure 5.6, amplitude distribution of sea clutter is investigated with respect to grazing angle. Considering the standard deviations for each angle, the amount of fluctuation in NRCS increases with increasing grazing angle. This means NRCS has wider range of variation around the mean value of distribution. Also, as it was discussed in previous section, mean value of NRCS is increasing with increasing grazing angle. Furthermore, statistical simulation results for Sea State 6 are given below.

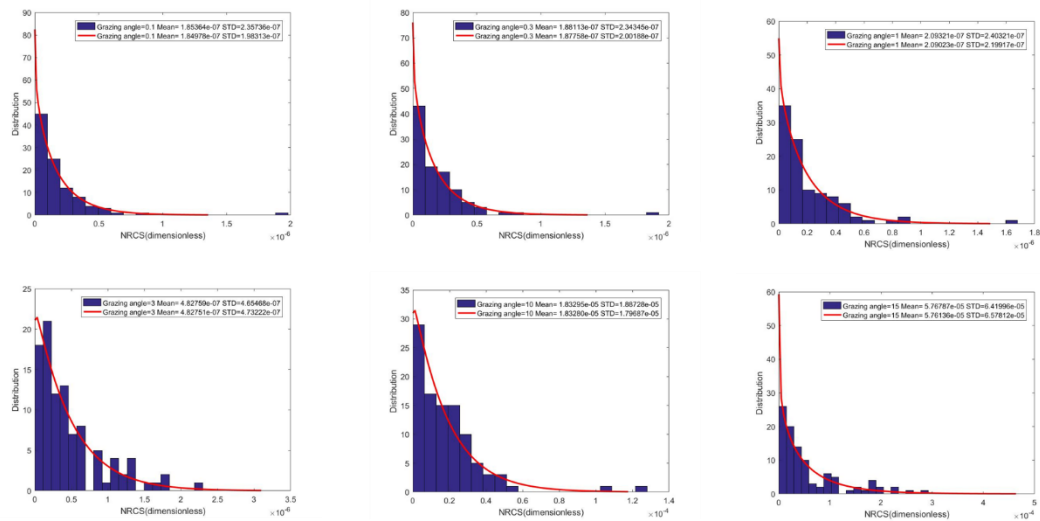


Figure 5.7.  $TM_z$  case Elfouhaily spectrum Histograms and Weibull distributions of NRCS at 500MHz for Sea State 6 with Ensemble sampling

In Figure 5.7, standard deviation and mean NRCS parameters are greater than those in sea state 1 for each corresponding grazing angle. Since surface roughness is increased, NRCS distribution becomes spikier and it has higher backscatter power. Consequently, Weibull distributions in Figure 5.7 approach to Log-normal distribution. In addition to surface roughness discussion, simulation results of 300MHz, grazing angle of  $10^\circ$  and sea states 1 to 6 are given in Figure 5.8.

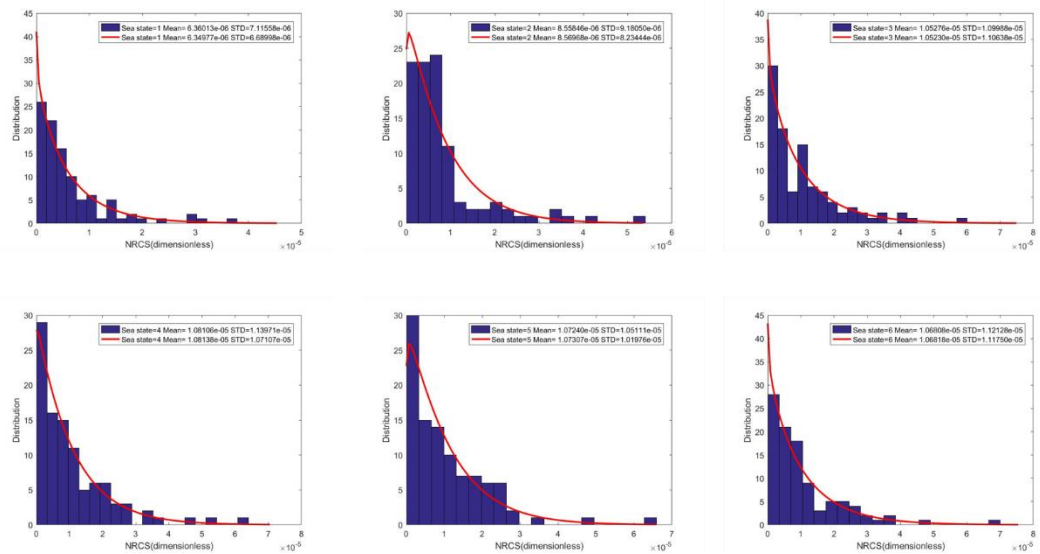


Figure 5.8.  $TM_z$  case Elfouhaily spectrum Histograms and Weibull distributions of NRCS at 300MHz and  $10^\circ$  grazing angle for Sea States 1 to 6 with Ensemble sampling

In Figure 5.8, it can be stated that increasing surface roughness increases both mean and standard deviation of NRCS.

Moreover, simulations for the distribution of NRCS are performed for surfaces generated by using Pierson-Moskowitz spectrum and shown in Figure 5.9.

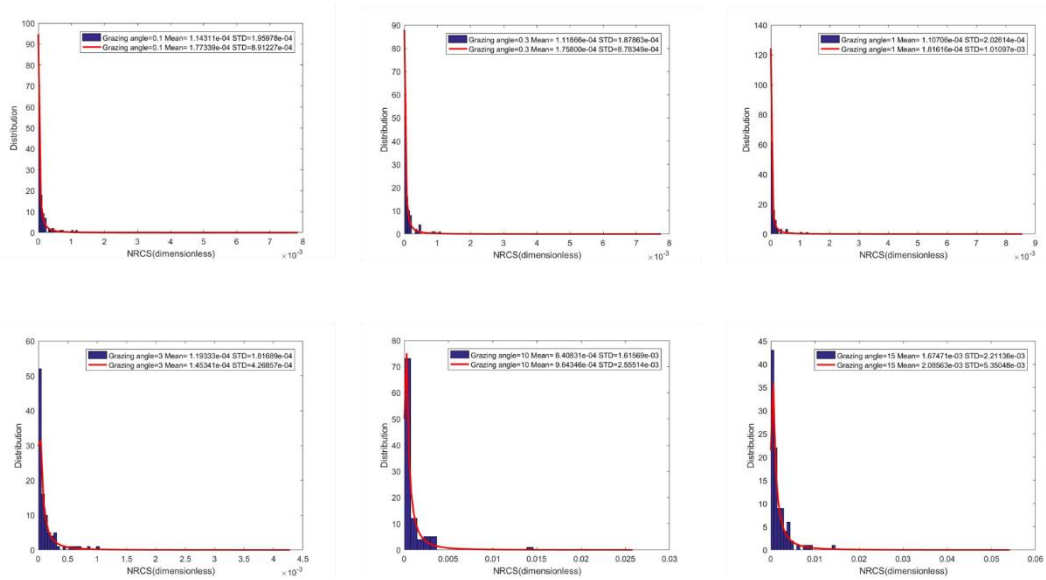


Figure 5.9.  $TM_z$  case PM spectrum Histograms and Log-normal distributions of NRCS at 500MHz for Sea State 6 with Ensemble sampling

Histograms in Figure 5.9 are fitted to Log-normal distributions. Because of higher wind speeds for PM spectrum, capillary waves are neglected. Thus, the mean amplitude and fluctuations in power returns become much higher than the Elfouhaily spectrum case.

## 5.2 Simulation results for $TM_z$ case with space sampling

To make a comparative analysis with ensemble sampling, only the surface generation and space partitioning part is different from the approach in the previous section. For space sampling, a single surface is generated and divided into 64 subdomains for this case. Therefore, total lengths of the single surfaces are 9600m, 6400m, and 3840m for radar frequencies 100MHz, 300MHz and 500MHz, respectively. Then, Monte Carlo technique is applied over 64 samples and mean amplitude and amplitude distribution analysis is performed.

### 5.2.1 $TM_z$ case simulation results for the mean amplitude of sea clutter with space sampling

First, to compare space sampling with ensemble sampling and modified NRL model, the case in Figure 5.2 is performed with space sampling with 64 samples. Simulation results for this case are shown in terms of mean NRCS vs. grazing angle graphs for Sea states 1, 3 and 5 at 500MHz.

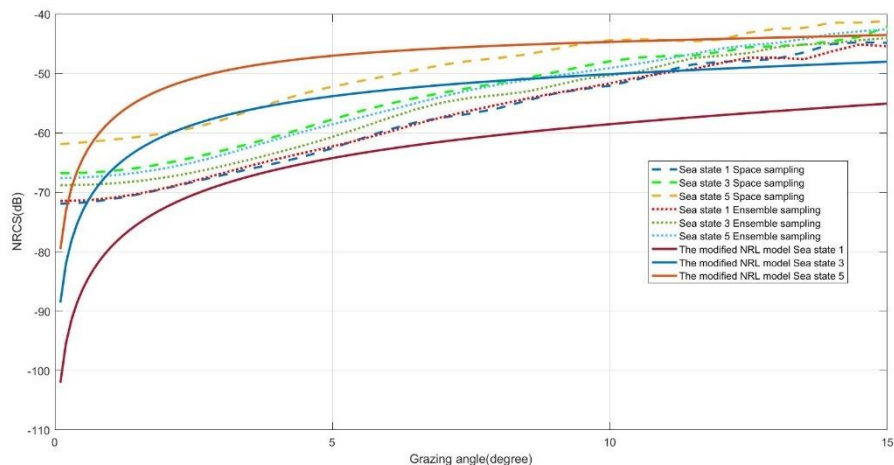


Figure 5.10.  $TM_z$  case mean NRCS vs. grazing angle graph for 500MHz, 60meter length and sea states 1,3 and 5 by using Elfouhaily spectrum with Space sampling, Ensemble sampling and the Modified NRL model

In Figure 5.10., space sampling shows better agreement with the modified NRL model than ensemble sampling. The main reason of this result is that spatial sampling ranges of Elfouhaily spectrum are different for the two techniques. For space sampling, the total length is 3840m resulting the spatial step size of wavenumber in Elfouhaily spectrum as,  $k_{s,min} = 2\pi/3840$  rad/m. And for  $N=65536$  number of points is chosen for IFFT, resulting the largest spatial wavenumber of space sampling as,  $k_{s,max} = Nk_{s,min} = 107.233$  rad/m. For ensemble sampling  $k_{s,min} = \frac{2\pi}{60}$  rad/m,  $N = 1024$  and  $k_{s,max} = 107.233$ rad/m. Therefore, for space sampling the Elfouhaily spectrum is sampled with higher resolution and space sampling starting from the lower wavenumber.

In Figure 5.11, a further discussion on space sampling is carried out as follows.

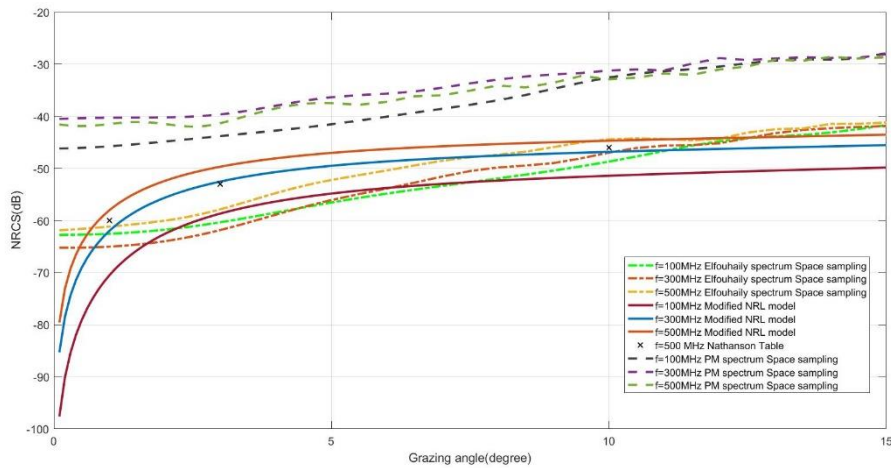


Figure 5.11.  $TM_z$  case mean NRCS vs. grazing angle graph for Sea State 5 by using Pierson-Moskowitz spectrum and Elfouhaily spectrum with Space sampling

For space sampling case, Elfouhaily spectrum yields more realistic results compared to the PM spectrum in terms of mean NRCS vs grazing angle, as in the case of the ensemble sampling.

To sum up, using space sampling and Elfouhaily spectrum yields the best accuracy for mean NRCS vs. grazing angle calculations in the light of the simulation results. The reason is that generated sea surfaces by using these two techniques include both

low and high spatial frequency components and higher spatial wavenumber resolution. Therefore, more realistic sea surfaces are generated and sampled compared to the observed nature resulting a better agreement with the other models.

### 5.2.2 $TM_z$ case simulation results for amplitude distribution of sea clutter with space sampling

This section is devoted to space sampling simulations for the amplitude distribution of sea clutter. The following simulations use the same parameters given in Section 5.1.2 to compare the results with ensemble sampling.

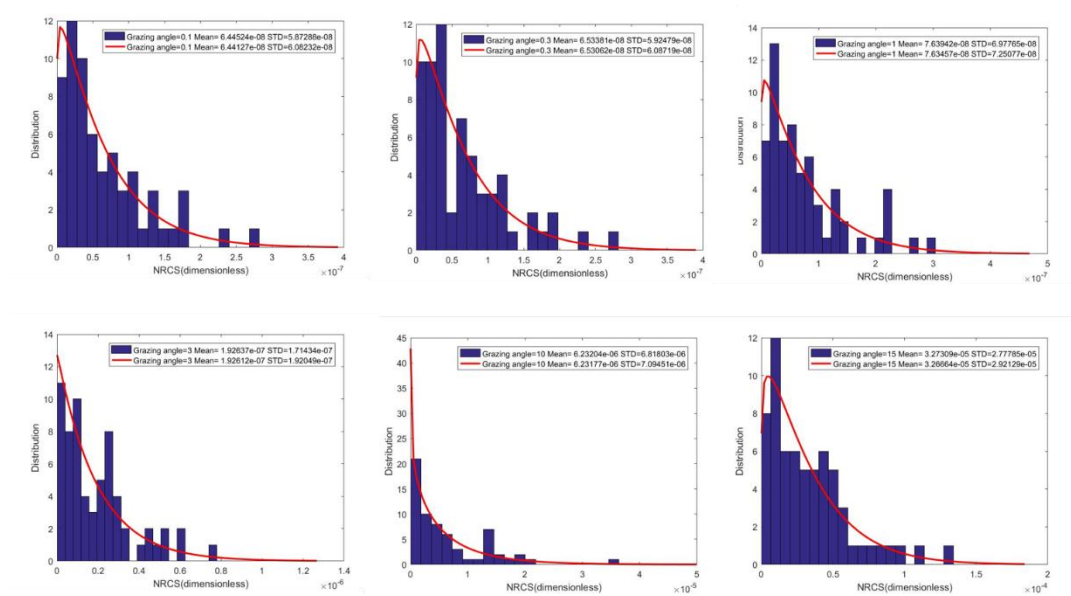


Figure 5.12.  $TM_z$  case Elfouhaily spectrum Histograms and Weibull distributions of NRCS at 500MHz for Sea State 1 with Space sampling

In space sampling case, grazing angle dependence of the distribution is similar to that of the ensemble sampling case. However, there is a difference in terms of the surface roughness between the two cases. In Figure 5.6, mean and STD values are greater than the values in Figure 5.12 up to  $10^\circ$  and at  $15^\circ$ , vice a versa. Thus, the surface roughness for the generated sea surfaces with space sampling is less than the ones generated with ensemble sampling. However, at sea state 6, this situation is

opposite of the case for sea state 1. In this case, mean and STD values for space sampling are much higher than the ensemble sampling case. Consequently, space sampling results in a spiky distribution.

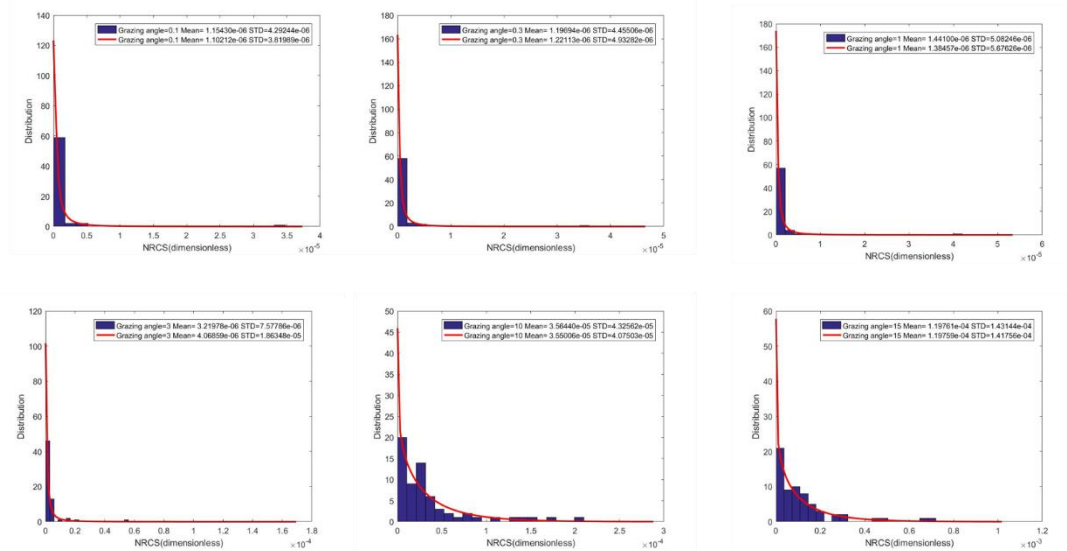


Figure 5.13.  $TM_z$  case Elfouhaily spectrum Histograms and Weibull and Lognormal distributions of NRCS at 500MHz for Sea State 6 with Space sampling. For grazing angles 3, 1, 0.3 and 0.1 degrees in Figure 5.13, Log-normal distribution fits better than the Weibull distribution. From this result, it can be said that increasing the wind speed is increasing the spikiness of the distribution especially at low grazing angles.

Following discussion is related to the sea state dependence of the amplitude distribution. Simulations are performed for a fixed frequency and grazing angle at sea states 1 to 6, as shown in Figure 5.14

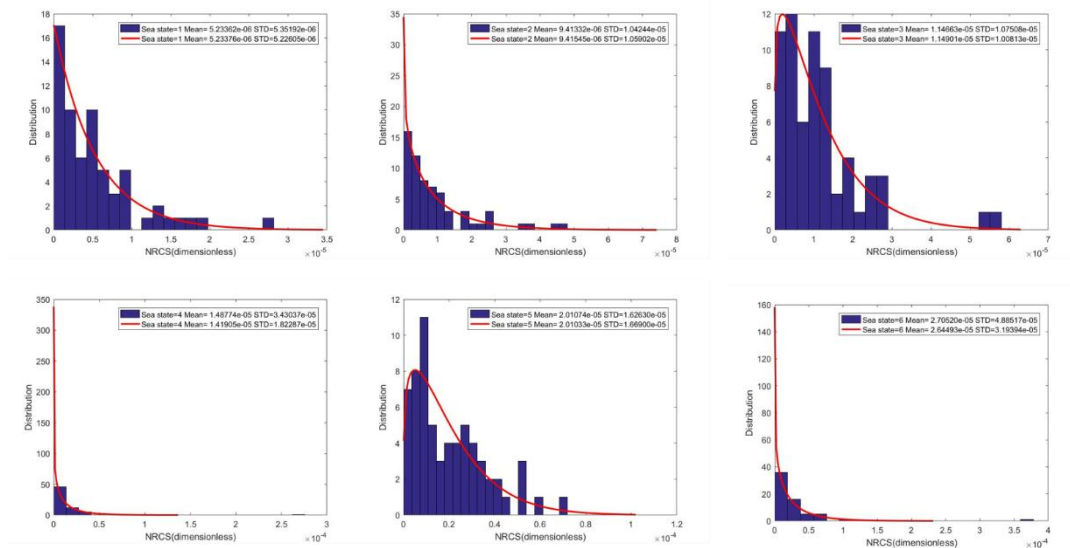


Figure 5.14.  $TM_z$  case Elfouhaily spectrum Histograms and Weibull distributions of NRCS at 300MHz and  $10^\circ$  grazing angle for Sea States 1 to 6 with Space sampling

In Figure 5.14., sea state dependence of the NRCS distribution is similar to the results in Figure 5.8. However, as the sea state increases space sampling has the wider range of fluctuations in NRCS and greater mean amplitudes. This is because of the range of sea surface spectrum sampling which is explained in Section 5.2.1. Using space sampling includes lower part of the Elfouhaily spectrum which has the peak value in this region resulting higher surface roughness and fluctuations in surface height.

Finally, PM spectrum is used for space sampling at 500MHz and Sea state 6 and resulting histograms are shown below.

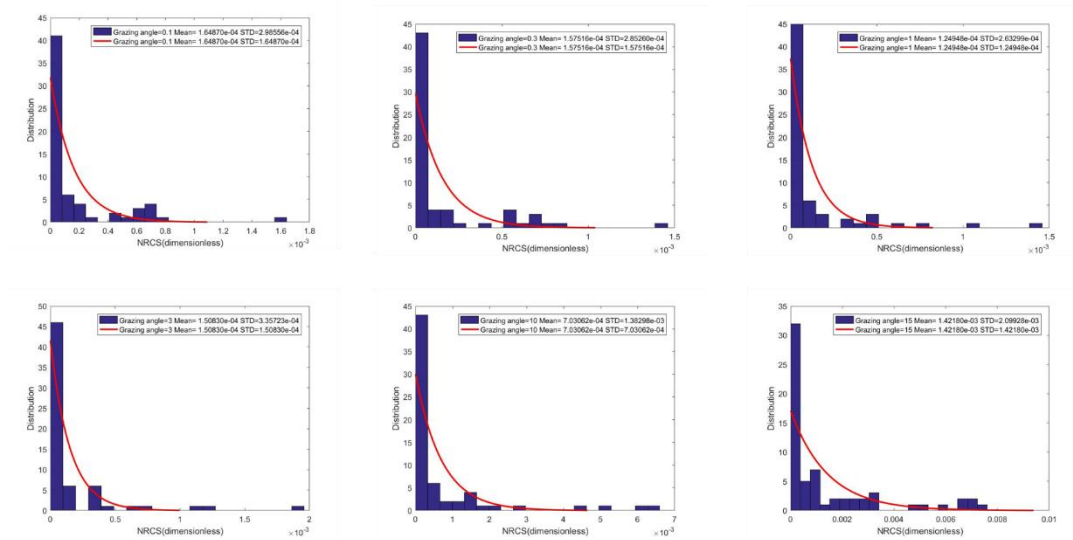


Figure 5.15.  $TM_z$  case PM spectrum Histograms and Log-normal distributions of NRCS at 500MHz for Sea State 6 with Space sampling

In Figure 5.15 PM spectrum with space sampling has longer tails than all other distributions presented before. Since space sampling increases the sampling range of the PM spectrum, peak values in PM spectrum contributed to the surface height profile substantially. Therefore, high scale surface height components i.e., gravity waves cause fluctuations of amplitude around the mean value. As a result, In Figure 5.16, exponential distribution which has longer tail is used to fit histograms obtained from PM spectrum with space sampling.

### 5.3 Simulation results for $TE_z$ case with ensemble sampling

In this section,  $TE_z$  case simulations are performed in a similar manner to those in  $TM_z$  case in Section 5.1. Simulations are performed with the same frequencies and the corresponding sea surface lengths. By doing this, simulation results of  $TE_z$  case are compared both with the empirical and statistical models and the simulation results of the  $TM_z$  case. After 100 simulations are performed for randomly generated sea surfaces for  $TE_z$  case, first mean amplitude vs grazing angle graphs are obtained

in Section 5.3.1. Then, In Section 5.3.2 amplitude distribution over 100 successive simulations are investigated by using histograms.

Note that grazing angle, sea state, surface length, frequency and number of simulations are the same as those given in Section 5.1 unless otherwise is stated.

### 5.3.1 $TE_z$ case simulation results for the mean amplitude of sea clutter with ensemble sampling

First, mean amplitude vs. grazing angle graph of sea clutter for 100MHz frequency and 150 meters surface length with different sea states, namely wind speeds, for both  $TE_z$  case and  $TM_z$  case is shown below.

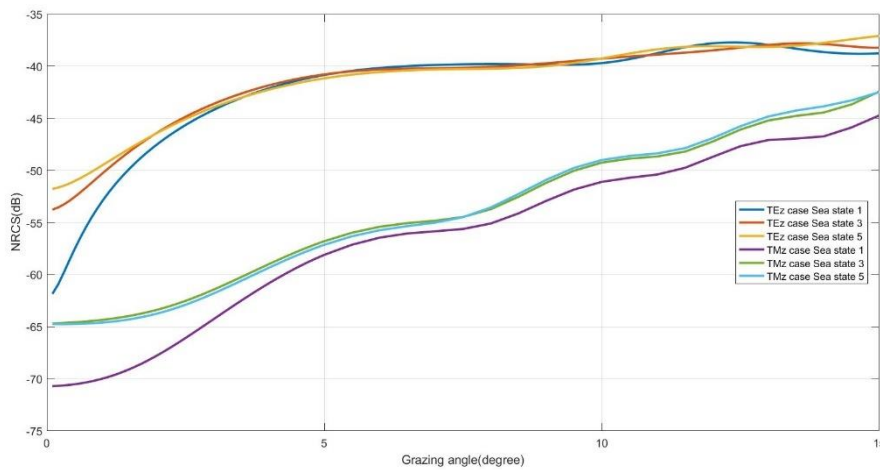


Figure 5.16.  $TE_z$  case and  $TM_z$  case mean NRCS vs. grazing angle graph for 100MHz, 150 meters length and sea states 1,3 and 5 by using Elfouhaily spectrum with Ensemble sampling

In Figure 5.16 the mean amplitude of sea clutter is increasing with the grazing angle sharply until 5 degrees. Then the grazing angle dependence of amplitude distribution decreases between 5 and 15 degrees. In addition, as the wind speed increases mean amplitude is increasing, as expected.

It can also be seen from Figure 5.16 that the mean amplitude for two polarization case is comparable in between 10 to 15 degrees. The main difference between these two cases is mostly observable under the 10 degrees.

Second, Nathanson Data vs. The Modified NRL model vs. Simulation result for sea state 4, 500MHz, 60meters and  $TE_z$  case by using Elfouhaily spectrum is shown below.

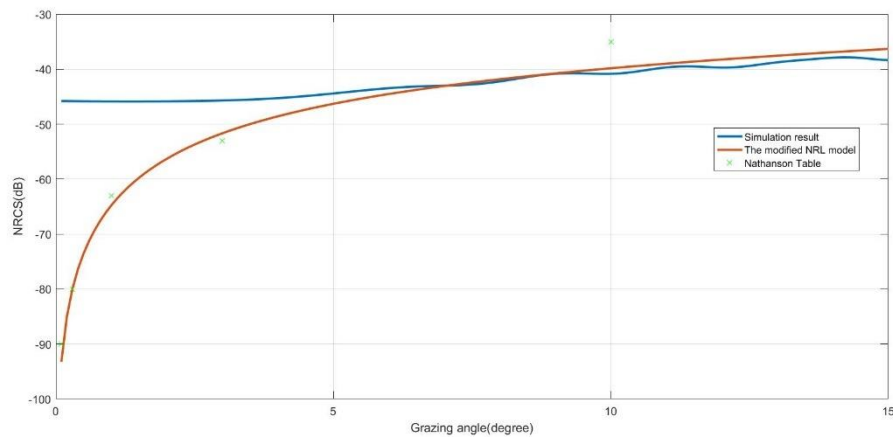


Figure 5.17.  $TE_z$  case mean NRCS vs. grazing angle graphs of simulation results, the modified NRL model and Nathanson's Table for 500MHz, 60meter length, Sea State 2 by using Elfouhaily spectrum with Ensemble sampling

In Figure 5.17, the simulation results are well met with both Nathanson Data and the modified NRL model for grazing angles greater than 5 degrees. This result is similar to the  $TM_z$  case. Therefore, simulation results show that the model given in this thesis may not be applicable for below 5 degrees in the case of calculation of mean backscattered power of sea surface.

Another comparison is given in between different frequencies for a fixed wind speed. For this purpose, grazing angle vs. NRCS graph is shown below.

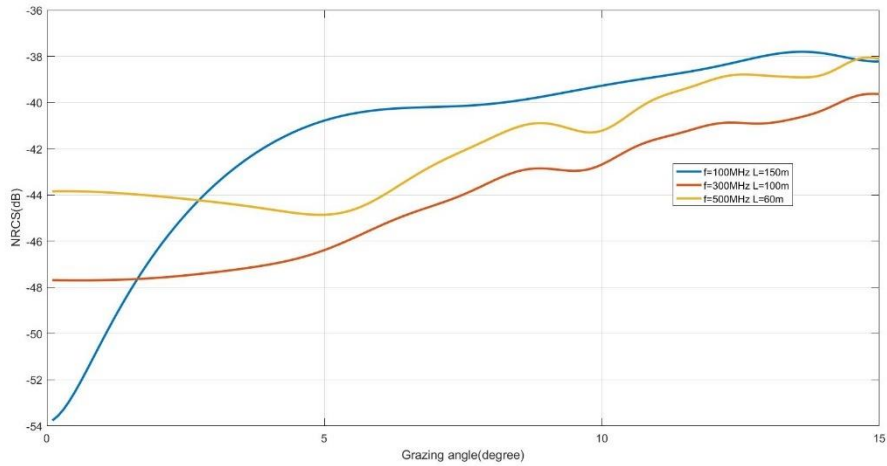


Figure 5.18.  $TE_z$  case mean NRCS vs. Grazing angle graph for 100MHz, 300MHz and 500MHz at Sea State 3 by using Elfouhaily spectrum with Ensemble sampling

In Figure 5.4 and Figure 5.18 there are some inconsistencies in terms of the frequency comparison for both polarizations. As it was discussed before, NRCS is increasing with increasing frequency. However, in these graphs results in 100MHz case are greater than those obtained for the other two frequencies. This might be due to the electrical length difference in between 100MHz ( $50\lambda$ ) and other two frequencies which are 300MHz and 500MHz ( $100\lambda$ ). This is resulting in a finer resolution for 100MHz case.

To sum up, a final graph is drawn to compare simulation results by using Pierson-Moskowitz and Elfouhaily spectrums with the modified NRL model and the Nathanson Table.

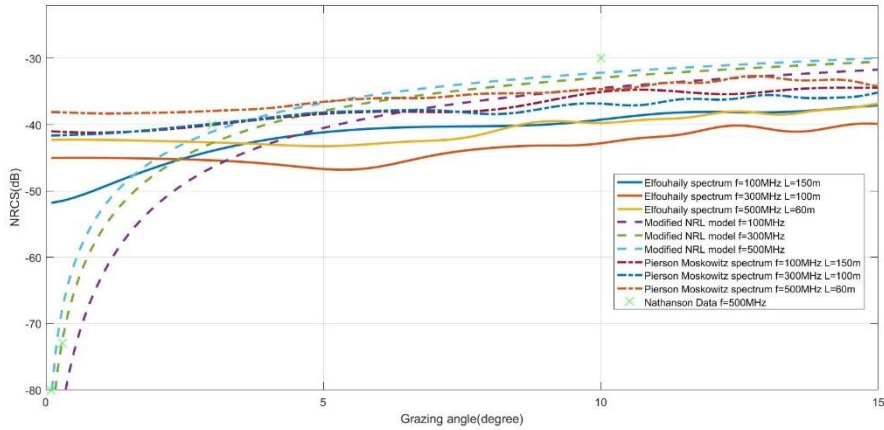


Figure 5.19.  $TE_z$  case mean NRCS vs. grazing angle graph for Sea State 5 by using Pierson-Moskowitz spectrum and Elfouhaily spectrum with Ensemble sampling

In Figure 5.19, simulation results of Pierson Moskowitz spectrum and Elfouhaily spectrums are almost identical except the region below 5 degrees. This might be due to the low frequency components of the sea spectrum being more effective for low grazing angles below 5 degrees. As it was discussed before, Elfouhaily spectrum is more effective in realizing the sea surface compared to Pierson-Moskowitz spectrum when considering the low frequency components of sea surfaces. Otherwise, both spectrums show similar results with the modified NRL model and the Nathanson Table.

### 5.3.2 $TE_z$ case simulation results for amplitude distribution of sea clutter with ensemble sampling

In this section of this thesis, histograms are plotted and fitted to the statistical distributions which are given in Chapter 4.2. Therefore, the results are given for  $TE_z$  case in a similar manner to the ones in Section 5.1.2. First, histograms, and statistical parameters such as mean and standard deviation are given below at 500MHz, Sea state 1 by using Elfouhaily spectrum and ensemble sampling.

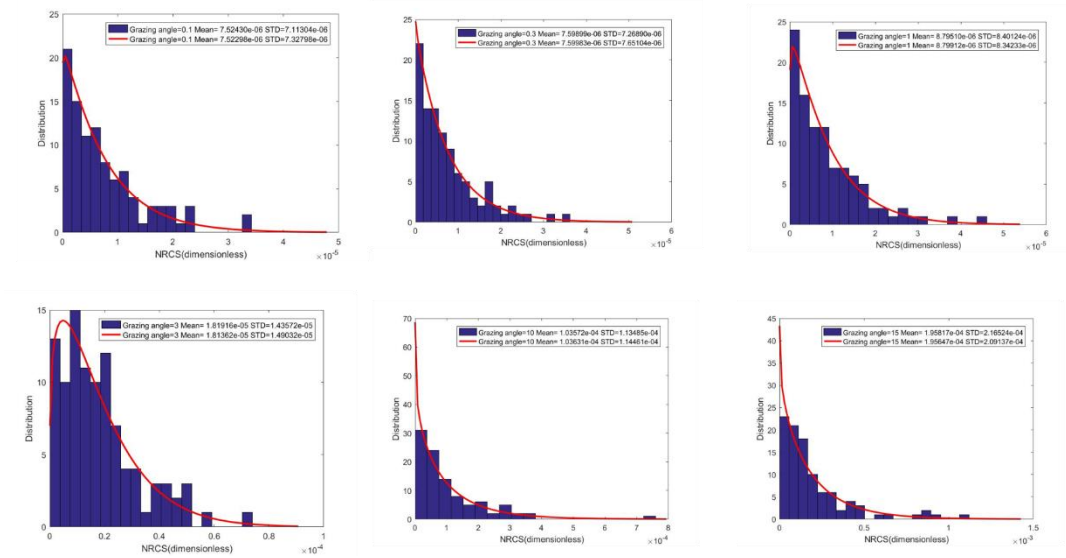


Figure 5.20.  $TE_z$  case Elfouhaily spectrum Histograms and Weibull distributions of NRCS at 500MHz for Sea State 1 with Ensemble sampling

In Figure 5.20, Weibull distributions are well fitted to the histograms by comparing the standard deviation and mean amplitudes of histogram and fitted distribution. As the grazing angle increases both mean amplitude and standard deviation of sea clutter increase similar to the  $TM_z$  case in Figure 5.6.

In addition, another set of histograms are given below with the same configurations in Figure 5.20 except Sea state which is defined as 6. In this case, mean and standard deviation increase compared to Sea state 1 due to the increasing surface roughness with increasing wind speeds. Consequently, both coherent and incoherent components of backscattered power are increasing with increasing wind speeds and grazing angle.

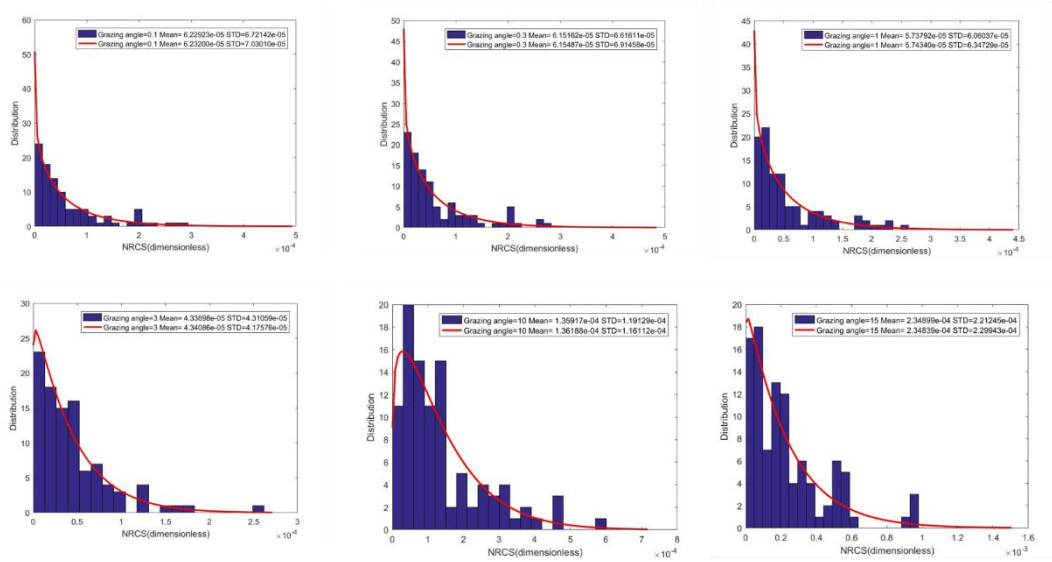


Figure 5.21.  $TE_z$  case Elfouhaily spectrum Histograms and Weibull distributions of NRCS at 500MHz for Sea State 6 with Ensemble sampling

In addition, to demonstrate the relation of wind speed vs. statistical distribution of sea clutter, a set of histograms at 300MHz and 0.3degrees for Sea states 1 to 6 are given below.

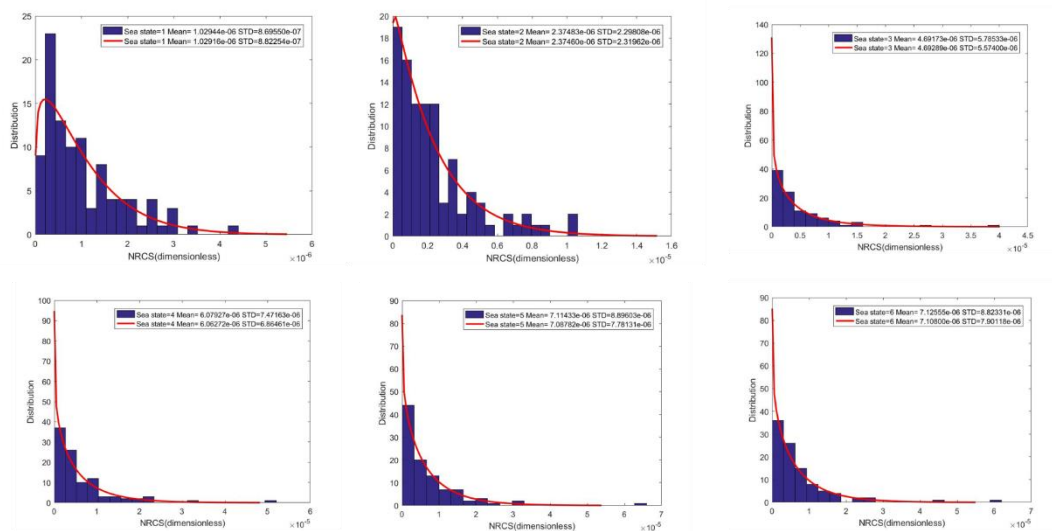


Figure 5.22.  $TE_z$  case Elfouhaily spectrum Histograms and Weibull distributions of NRCS at 300MHz and 0.3° grazing angle for Sea States 1 to 6 with Ensemble sampling

In Figure 5.22, increasing the sea state and wind speed yield a greater backscatter power and fluctuations of power which means roughness and randomness of sea surface increase with increasing wind speeds. Although there are high standard deviations at Sea state 5 and 6, they still fit into the Weibull distributions with a reasonable accuracy in terms of mean and variance.

A final discussion in this chapter is related to the spectrums that are used to obtain random sea surfaces. For this purpose, a set of histograms are plotted with the same configurations in Figure 5.22 by using the Pierson Moskowitz spectrum.

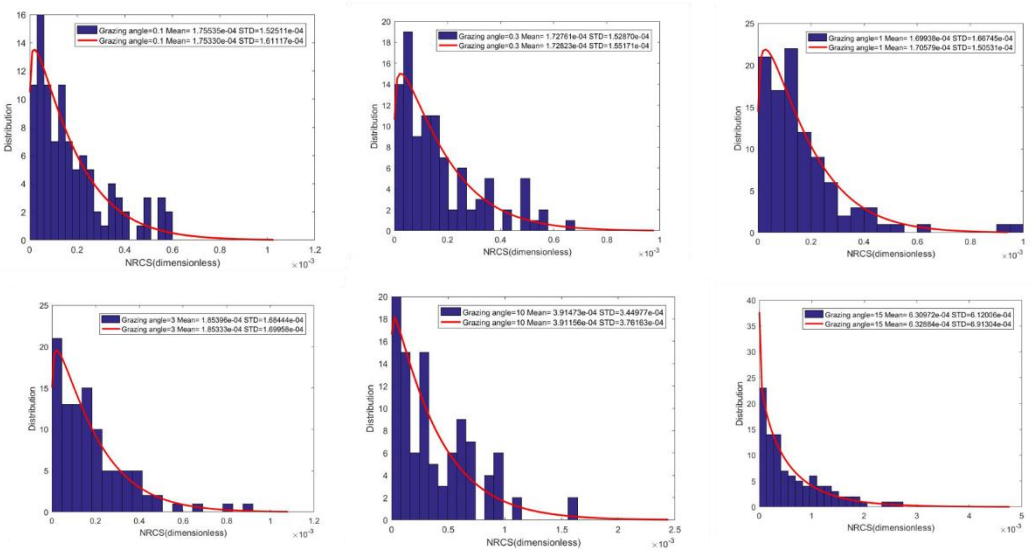


Figure 5.23.  $TE_z$  case Pierson Moskowitz spectrum Histograms and Weibull distributions of NRCS at 500MHz for Sea State 6 with Ensemble sampling

In Figure 5.23, all the histograms are fitted to Weibull distributions. However, it can be said that error in terms of variance is higher compared to Figure 5.21. Moreover, mean and variance are also higher in Figure 5.23 than those in Figure 5.21. Therefore, Pierson Moskowitz spectrum creates a spikier response than the one obtained by Elfouhaily spectrum. However, in  $TE_z$  case they are all fitted into Weibull distribution unlike the  $TM_z$  case in Figure 5.9. Consequently, neglecting the capillary waves in Pierson Moskowitz spectrum has less contribution in  $TE_z$  case than  $TM_z$  case in terms of statistical distribution.

## 5.4 Simulation results for $TE_z$ case with space sampling

In this section of the simulation results, simulations are performed with the same parameters given in Sec. 5.2. Therefore, 9600m, 6400m, and 3840m length sea surfaces are generated for radar frequencies 100MHz, 300MHz and 500MHz, respectively. Then, Monte Carlo technique is applied for 64 samples. In the first section of this chapter, mean amplitude vs. grazing angle graphs will be discussed. Next, the amplitude distribution of NRCS for each surface realization will be investigated.

### 5.4.1 $TE_z$ case simulation results for the mean amplitude of sea clutter with space sampling

As a first comparison of this section, ensemble sampling and space sampling simulation results are given at 100MHz for sea state 1,3 and 5 below.

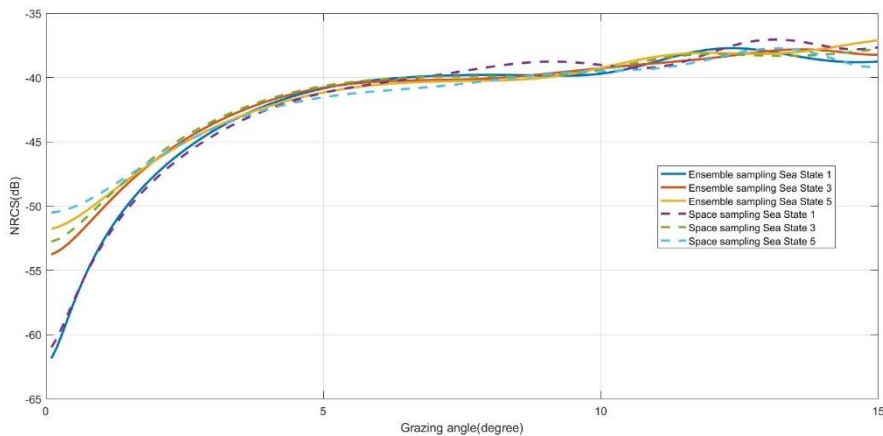


Figure 5.24.  $TE_z$  case mean NRCS vs. grazing angle graph for 100MHz, 150meter length and sea states 1,3 and 5 by using Elfouhaily spectrum with Space sampling and Ensemble sampling

In Figure 5.24, ensemble sampling and space sampling results are almost identical. Thus, sampling range in Elfouhaily spectrum does not change the response of the  $TE_z$  case.

Moreover, PM and Elfouhaily spectrums by using space sampling are compared with the Modified NRL model and Nathanson Table. Resulting grazing angle vs. NRCS is shown below.

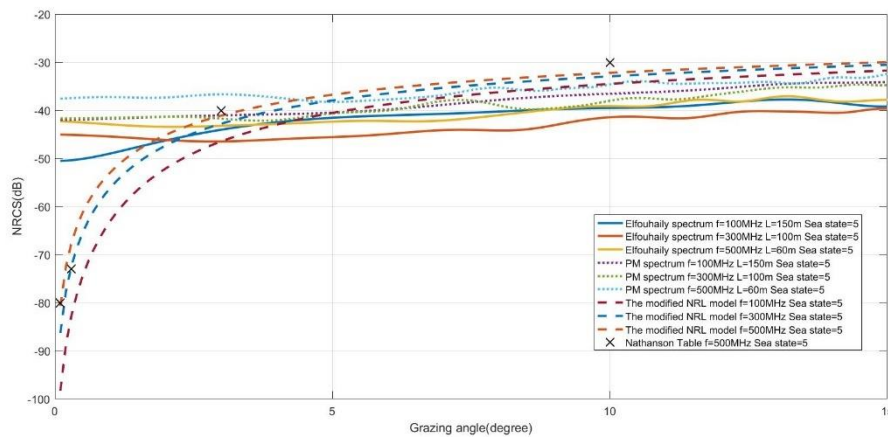


Figure 5.25.  $TE_z$  case mean NRCS vs. grazing angle graph for Sea State 5 by using Pierson-Moskowitz spectrum and Elfouhaily spectrum with Space sampling

In Figure 5.25 PM spectrum gives higher mean backscatter power in all angles than Elfouhaily spectrum, which results in a better agreement with the empirical models at grazing angles greater than 5 degrees. However, at low grazing angles, Elfouhaily spectrum has lower backscatter power due to the capillary waves in spectrum which shows a better agreement with empirical models than PM spectrum.

Although there are minor differences in Figure 5.24 and Figure 5.25, it is worth to investigate their properties in terms of statistical distribution in the following section.

## 5.4.2 $TE_z$ case simulation results for amplitude distribution of sea clutter with space sampling

In this section, there are plots of several amplitude distributions of sea clutter over 64 surface realizations and resulting NRCS values. To make a comparison between space and ensemble sampling in detail, a set of histograms for different angles at 500MHz, Sea State 1 and Elfouhaily spectrum are given below.

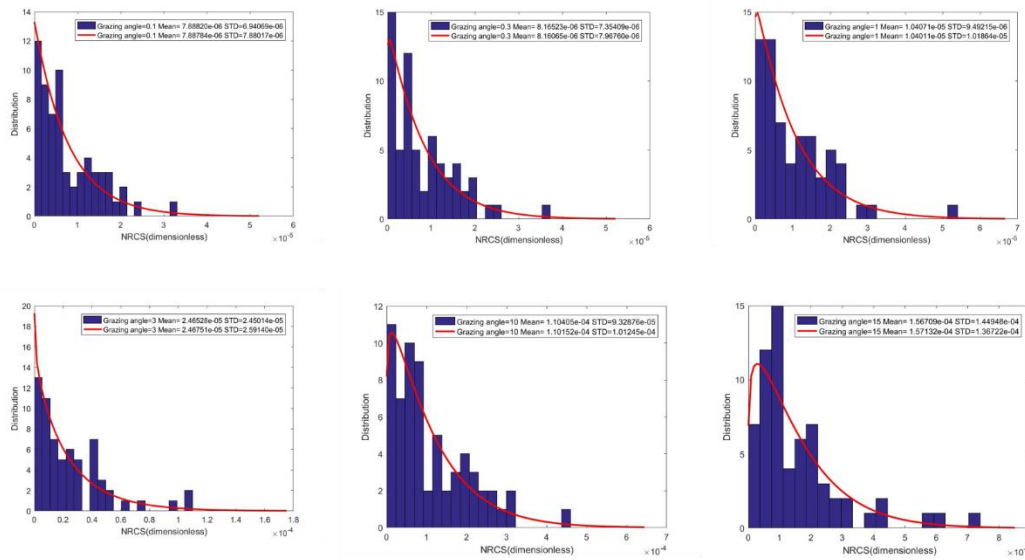


Figure 5.26.  $TE_z$  case Elfouhaily spectrum Histograms and Weibull distributions of NRCS at 500MHz for Sea State 1 with Space sampling

In Figure 5.26 as the grazing angle increases, both coherent and non-coherent component of the sea clutter increase similar to the other cases. However, a main difference in Figure 5.26 compared to the ensemble sampling in Figure 5.20 is the error margin in fitted Weibull distribution. In space sampling case, due to the contribution of the low frequency portion of the Elfouhaily spectrum, histograms are distributed in wider range yielding a spiky distribution. Therefore, histograms in space sampling case are in between Weibull and Lognormal distribution.

In addition to Sea state 1, histograms for Sea state 6 are given below to demonstrate space sampling properties.

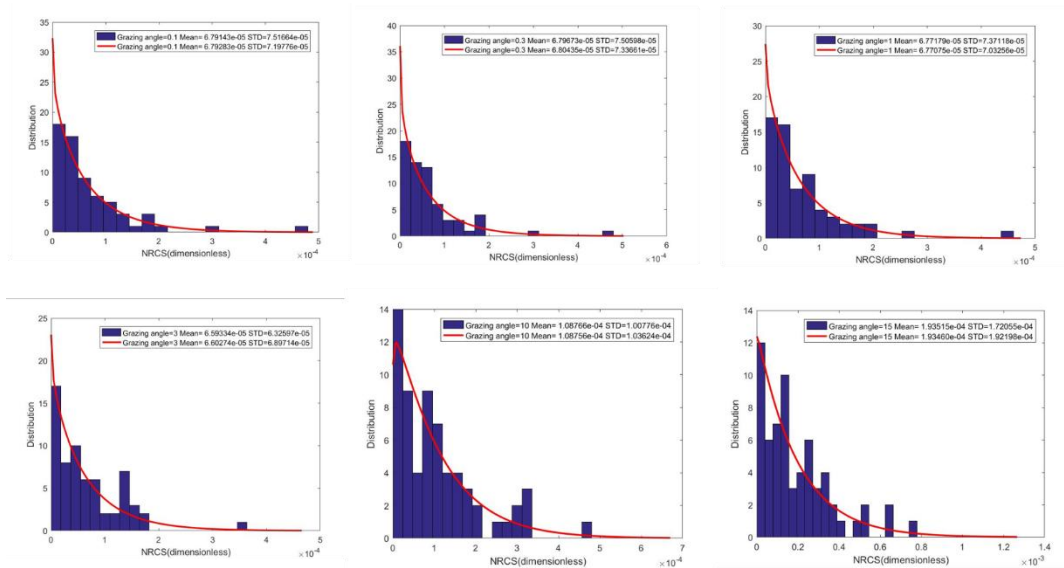


Figure 5.27.  $TE_z$  case Elfouhaily spectrum Histograms and Weibull distributions of NRCS at 500MHz for Sea State 6 with Space sampling

In Figure 5.27 in all angles, NRCS distributions have higher mean and STD than those in Figure 5.26 due to increasing surface roughness. However, it can be concluded that  $TE_z$  case is less sensitive to the increased surface roughness than the  $TM_z$  case in all simulation results in this thesis. To show wind speed dependence of  $TE_z$  case with space sampling, a set of histograms plotted for Sea state 1 to 6 at 300MHz and 0.3-degree grazing angle are shown below.

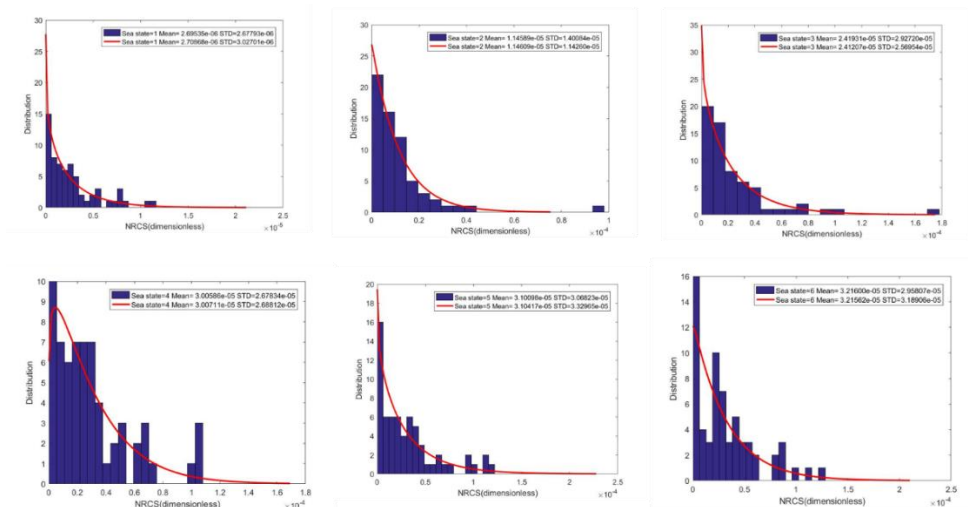


Figure 5.28.  $TE_z$  case Elfouhaily spectrum Histograms and Weibull distributions of NRCS at 300MHz and  $0.3^\circ$  grazing angle for Sea States 1 to 6 with Space sampling

In Figure 5.24, the wind speed dependence of sea clutter of  $TE_z$  case is higher below 3-degree grazing angle. Thus, to differentiate the distributions of sea states, 0.3degree grazing angle is used in Figure 5.28. As it can be seen in all graphs in Figure 5.28, the mean and STD increase with increasing surface roughness.

In addition to histograms obtained by using the Elfouhaily spectrum, a set of histograms for different angles by using PM spectrum with space sampling at 500MHz, Sea state 6 are given below.

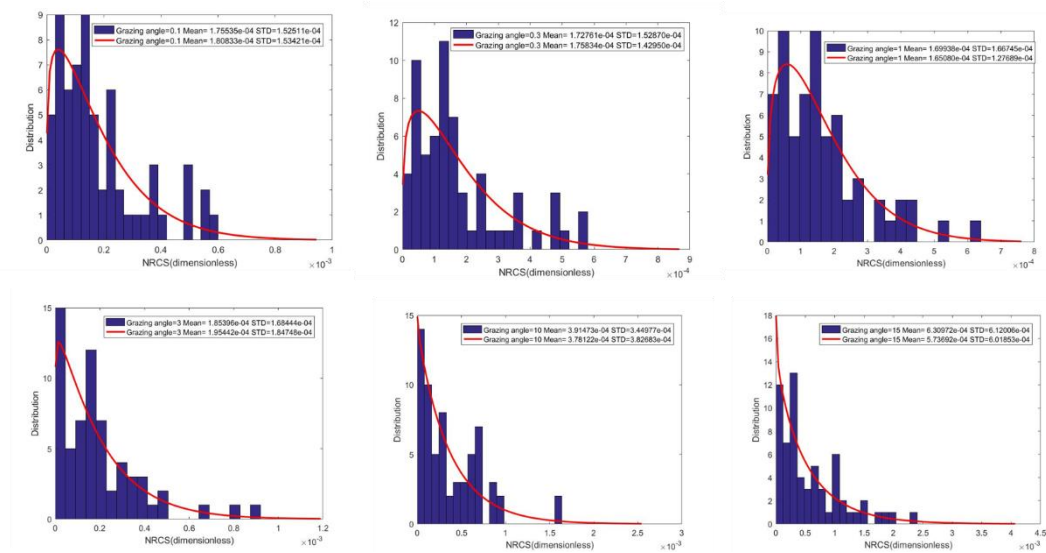


Figure 5.29.  $TE_z$  case Pierson Moskowitz spectrum Histograms and Weibull distributions of NRCS at 500MHz for Sea State 6 with Space sampling

In Figure 5.29, mean and variance of NRCS are greater in all angles than the results in Figure 5.27. This result is similar to the ensemble sampling case in section 5.3.2. However, space sampling results in a better fit of Weibull distribution in Figure 5.29 than ensemble sampling in Figure 5.24. Therefore, using the wider sampling range for both spectrums are giving consistent results with the Weibull distribution.



## CHAPTER 6

### CONCLUSIONS

For radar design engineers, sea clutter has been a serious problem and in many cases it is hard to discriminate it from the actual target. In order to handle this difficulty, characterization of the sea clutter properties is essential for a variety of environmental conditions. This problem has two aspects: amplitude characterization and frequency i.e., doppler shift characterization. In this thesis, a model is proposed to characterize only the amplitude of the sea clutter. In the literature there are many works devoted to this amplitude characterization issue such as measurement results, empirical and statistical models. However, they all have certain limitations such as frequency range, grazing angle range and environmental conditions. Furthermore, they tend to give the results over many measurements in terms of statistical parameters such as mean and variance. In addition, taking measurements from real sea surfaces or wave tanks is a time consuming and expensive method to model sea clutter.

In this thesis, a model is proposed to obtain sea clutter properties by using the power of Computational Electromagnetics and Oceanography. By doing that, several 2D instances of sea surfaces are realized and resulting backscattered field power is calculated and normalized. Hence, a more detailed information about sea clutter is obtained by using the Monte Carlo method. Then, the data obtained from the simulations are given in terms of mean, variance, and histograms.

To sum up, according to the simulation results and analysis given in Chapter 5, review of the proposed method is listed below.

- For below a certain degree in the grazing angles for both polarization cases, the proposed model is overestimating the mean NRCS.

- As it was indicated in the previous chapter, as the wind speed and surface roughness increase both the coherent and incoherent component of the clutter return also increase.
- There are some discrepancies in simulation results in terms of the relation between frequency and mean NRCS for both polarization cases.
- In general, the space sampling method gives more consistent results with the empirical and statistical models than ensemble sampling method. Main reason behind this result is the sampling range difference of the spectrum.
- Using the Elfouhaily spectrum gives an advantage in terms of wind speed range of the model. Moreover, it has an advantage over the PM spectrum because it is including both capillary and gravity waves. As a result of the simulation result obtained in Chapter 5, using Elfouhaily spectrum with space sampling is the most convenient way of modeling sea clutter.
- $TE_z$  case has greater NRCS than the  $TM_z$  case in all cases and it is less sensitive to the frequency, wind speed and grazing angle changes.

In addition to these conclusions, the major drawback of the proposed model is the computation time. Although empirical models are easy to use, the proposed model in this thesis is a flexible and powerful tool to encounter the sea clutter problem, since it can be optimized for a certain radar application unlike the other models. Moreover, reducing the problem into one dimension by assuming the sea surface as PEC at low grazing angles and Method of Moments provide agile and accurate simulation performance of the proposed model. By using the power of today's computers and the Method of Moments, sea clutter, which is a complex, time varying hydrodynamic problem can be analyzed.

## 6.1 Future Work

Since the proposed model is only applicable to 2D surfaces, more efficient computational methods can be used to model 3D surfaces. This may result in an enormous computational load but dividing the problem into small pieces and solving each of them might give a reasonable computation time. Due to this reason, maximum frequency is limited up to 500MHz in this thesis. Increasing the frequency range is possible either by using electrically small surfaces or increasing the efficiency of the computational method.

Instead of using incident field tapering given in Chapter 3.8., a more advanced method such as Thorsos tapered wave [40] can be used to avoid abrupt current changes at edges of the surface without violating Maxwell's Equations.

The grazing angle range can be extended to 90 degrees which results in a dielectric sea surface. Therefore, impedance boundary conditions [33] should be used instead of the boundary conditions on PEC. Moreover, for grazing angles below 5-degree, accuracy of the proposed model can be increased.

In addition, clutter calculations in 2D yield scalar formulations in MoM and therefore there is no cross-polarization component existing in the sea clutter. Cross-polarized component of the sea clutter can also be analyzed by using a 3D non-PEC sea surface modeling.



## REFERENCES

- [1] L. Whitrow, "A model of low grazing angle sea clutter for coherent RADAR performance analysis," DSTO Defense Sci. Technol. Org., Australia, Tech. Rep. DSTO-TR-2864, Jun. 2013
- [2] F. Nathanson, J. Reilly, and M. Cohen, *RADAR Design Principles: Signal Processing and the Environment*. Scitech Pub., 1999.
- [3] Horst, M.M., Dyer, F.B., and Tuley, M.T., "RADAR sea clutter model", International IEEE AP/S URSI Symposium, Maryland, 1978, pp 6-10
- [4] Reilly, J.P., "Clutter Models For Shipboard RADAR Applications: 0.5 to 70 GHz", Technical Report, Task 3-1-18, Multisensor Propagation Data and Clutter Modelling, NATO AAW System Program Office, NAAW-88-062R, June 10, 1988
- [5] Technology Service Corporation, 1990, Section 5.6.1: Backscatter from sea, *RADAR Workstation*, vol. 2, pp. 177–186, 1990
- [6] Gregers-Hansen, V., and Mital, R.. "An Empirical Sea Clutter Model for Low Grazing Angles", *IEEE RADAR Conference 2009*, pp 1-5
- [7] V. Gregers-Hansen and R. Mital, "An Improved Empirical Model for RADAR Sea Clutter Reflectivity," in *IEEE Transactions on Aerospace and Electronic Systems*, vol. 48, no. 4, pp. 3512-3524, October 2012
- [8] I. Antipov, 'Simulation of sea clutter returns', DSTO Electronic and Surveillance Research Laboratory, Salisbury, South Australia, DSTO-TR-0679, June 1998
- [9] G. V. Trunk and S. F. George, "Detection of Targets in Non-Gaussian Sea Clutter," in *IEEE Transactions on Aerospace and Electronic Systems*, vol. AES-6, no. 5, pp. 620-628, Sept. 1970
- [10] M. Sekine and Y. Mao, *Weibull RADAR Clutter*, (IEE RADAR Sonar and Navigation and Avionics). Stevenage, U.K.: IET, 1990.
- [11] D. Holliday, "Resolution of a controversy surrounding the Kirchhoff approach and the small perturbation method in rough surface scattering theory," in *IEEE Transactions on Antennas and Propagation*, vol. 35, no. 1, pp. 120-122, January 1987
- [12] K. Ward, S. Watts, R. Tough, I. of Engineering, Technology, and I. of Electrical Engineers, *Sea clutter: scattering, the K-distribution and RADAR performance* 2nd Edition. IET RADAR, sonar and navigation series, Institution of Engineering and Technology, 2013

- [13] O. Ozgun and M. Kuzuoglu, "Finite Element Domain Decomposition Method for Rough Sea Surface Scattering," 2019 IEEE International Symposium on Antennas and Propagation and USNC-URSI Radio Science Meeting, Atlanta, GA, USA, 2019, pp. 2091-2092
- [14] D. Holliday, L. L. DeRaad and G. J. St-Cyr, "Forward-backward: a new method for computing low-grazing angle scattering," in IEEE Transactions on Antennas and Propagation, vol. 44, no. 5, pp. 722-, May 1996
- [15] C. D. Moss, F. L. Teixeira, Y. E. Yang and Jin Au Kong, "Finite-difference time-domain simulation of scattering from objects in continuous random media," in IEEE Transactions on Geoscience and Remote Sensing, vol. 40, no. 1, pp. 178-186, Jan. 2002
- [16] C. Bourlier, S. Bellez, H. Li and G. Kubické, "Sub-Domain Decomposition Iterative Method Combined With ACA: An Efficient Technique for the Scattering From a Large Highly Conducting Rough Sea Surface," in IEEE Transactions on Antennas and Propagation, vol. 63, no. 2, pp. 659-666, Feb. 2015
- [17] Christophe, Bourlier & Pinel, Nicolas & Kubické, Gildas. (2013). Method of moments for 2D scattering problems: Basic concepts and applications.
- [18] Pierson, W. J., and Moskowitz, L. (1964), A proposed spectral form for fully developed wind seas based on the similarity theory of S. A. Kitaigorodskii, J. Geophys. Res., 69( 24), 5181– 5190
- [19] Elfouhaily, T., Chapron, B., Katsaros, K., and Vandemark, D. (1997), A unified directional spectrum for long and short wind-driven waves, J. Geophys. Res., 102( C7), 15781– 15796
- [20] O. Ozgun, and M. Kuzuoglu, MATLAB-based Finite Element Programming in Electromagnetic Modeling. CRC Press, 2018
- [21] M. S. Greco, "RADAR clutter modeling." [Online]. Available: [http://www.iet.unipi.it/m.greco/esami\\_lab/RADAR/Clutter\\_modeling.pdf](http://www.iet.unipi.it/m.greco/esami_lab/RADAR/Clutter_modeling.pdf). Accessed on 08/08/2020
- [22] M. Skolnik, Introduction to RADAR Systems. Electrical engineering series, McGraw-Hill, 2001.
- [23] L. Rosenberg, S. Watts and M. S. Greco, "Modeling the Statistics of Microwave RADAR Sea Clutter," in IEEE Aerospace and Electronic Systems Magazine, vol. 34, no. 10, pp. 44-75, 1 Oct. 2019

- [24] O. Ozgun and M. Kuzuoglu, "A Domain Decomposition Finite-Element Method for Modeling Electromagnetic Scattering From Rough Sea Surfaces With Emphasis on Near-Forward Scattering," in *IEEE Transactions on Antennas and Propagation*, vol. 67, no. 1, pp. 335-345, Jan. 2019
- [25] P. Xiradakis, "The refractive effects of laser propagation through the ocean and within the ocean," M.S. thesis, Naval Postgraduate School, Monterey, CA, USA, 2009
- [26] Mobley, C. D., 2014. Modeling Sea Surfaces: A Tutorial on Fourier Transform Techniques. Sequoia Scientific, Inc. [Online] Available: <http://www.oceanopticsbook.info/view/references/publications> Accessed on:08/08/2020
- [27] Rosson,N., Scaling the FFT and the IFFT, 2011,[Online] Available: <https://www.mathworks.com/matlabcentral/answers/15770-scaling-the-fft-and-the-iff> Accessed on:08/08/2020
- [28] Hasselmann, K., et al., Measurements of wind-wave growth and swell during the Joint North Sea Wave Project (JONSWAP), *Dtsch. Hydrogr.Z.*, 12, 95 pp., 1973.
- [29]Phillips, O. M., Spectral and statistical properties of the equilibrium range in the wind-generated gravity waves, *J. Fluid Mech.*, 156, 505-531, 1985.
- [30] Kitaigorodskii, S. A, The Physics of Air-Sea Interactions, pp. 9-73,Keter Press, Jerusalem, 1973.
- [31] Malcolm L Heron (2002) Applying a unified directional wave spectrum to the remote sensing of wind wave directional spreading, *Canadian Journal of Remote Sensing*, 28:3, 346-353
- [32] W. C. Gibson, The Method of Moments in Electromagnetics, , Chapman and Hall/CRC, 2007
- [33] A. F. Peterson, S. L. Ray, R. Mittra, Computational Methods for Electromagnetics, Wiley – IEEE Press, 1997.
- [34] C. A. Balanis, Advanced Engineering Electromagnetics. John Wiley and Sons, 1989
- [35] M. N. Sadiku, Elements of Electromagnetics, Fifth Edition, Oxford University Press, Inc., New York, 2010
- [36] R. F. Harrington, Time-Harmonic Electromagnetic Fields, McGraw-Hill, New York, 1961

[37] C. A. Balanis, *Antenna Theory: Analysis and Design*, 3rd Edition, John Wiley & Sons, New York, 2005

[38] Oppenheim, Alan V., Ronald W. Schafer, and John R. Buck. *Discrete-Time Signal Processing*. Upper Saddle River, NJ: Prentice Hall, 1999

[39] M. N. O. Sadiku and A. F. Peterson, "A comparison of numerical methods for computing electromagnetic fields," *IEEE Proceedings on Southeastcon*, New Orleans, LA, USA, 1990, pp. 42-47 vol.1

[40] E.I. Thorsos, "The validity of the Kirchhoff approximation for rough surface scattering using a Gaussian roughness spectrum" *The Journal of the Acoustical Society of America* 83, 78, 1988.

## APPENDICES

### A. Discrete Fourier Transform Theory

Suppose that surface height profiles are sampled at  $N$  points  $x_r, r = 0, 1, \dots, N - 1$  and Equation 2.5 becomes,

$$y(x_r) = \sum_{u=-\frac{N}{2}-1}^{\frac{N}{2}} c_u e^{jk_n x_r} \quad (\text{A.1})$$

Discrete Fourier Transform of  $y(x_r)$  can be described as,

$$\hat{y}(v_u) = \frac{1}{N} \sum_{r=0}^{N-1} y(x_r) e^{-j2\pi v_u x_r} \quad (\text{A.2})$$

where  $v_u = \frac{u}{L}$  is the discrete spatial frequency. The corresponding inverse discrete Fourier transform is given below.

$$y(x_r) = \sum_{u=0}^{N-1} \hat{y}(v_u) e^{j2\pi v_u x_r} \quad (\text{A.3})$$

Moreover, a relation between DFT pair which is called Parseval's relation can be written as follows,

$$\sum_{r=0}^{N-1} |y(x_r)|^2 = N \sum_{u=0}^{N-1} |\hat{y}(v_u)|^2 \quad (\text{A.4})$$

Furthermore, one sided power spectral density functions defined in PM and Elfouhaily spectrum can be written in terms of DFT of surface height as follows.

$$S_{1S}(v_u) = |\hat{y}(v_u)|^2 \quad (\text{A.5})$$

Or it can also be written in terms of spatial wave number  $k_u = 2\pi v_u$ ,

$$S_{1S}(k_u) = |\hat{y}(k_u)|^2 \quad (\text{A.6})$$



## B. Vector Identities

Some of the well-known vector identities that are used in this thesis are presented in this Appendix.

$$\bar{A} \times \bar{B} = -\bar{B} \times \bar{A} \quad (B.2)$$

$$\bar{A} \times (\bar{B} \times \bar{C}) = (\bar{A} \cdot \bar{C})\bar{B} - (\bar{A} \cdot \bar{B})\bar{C} \quad (B.3)$$

$$\nabla \cdot (\nabla \times \bar{A}) = 0 \quad (B.4)$$

$$\nabla \times \nabla \psi = 0 \quad (B.5)$$

$$\nabla(\psi\phi) = \phi\nabla\psi + \psi\nabla\phi \quad (B.6)$$

$$\nabla \cdot (\psi\bar{A}) = \bar{A} \cdot \nabla\psi + \psi\nabla \cdot \bar{A} \quad (B.7)$$

$$\nabla \times (\psi\bar{A}) = \nabla\psi \times \bar{A} + \psi\nabla \times \bar{A} \quad (B.8)$$

$$\nabla \times \nabla \times \bar{A} = \nabla(\nabla \cdot \bar{A}) - \nabla^2\bar{A} \quad (B.9)$$

$$\nabla \cdot (\bar{A} \times \bar{B}) = \bar{B} \cdot \nabla \times \bar{A} - \bar{A} \cdot \nabla \times \bar{B} \quad (B.10)$$

$$\oint_C \bar{A} \cdot d\mathbf{l} = \iint_S (\nabla \times \bar{A}) \cdot d\mathbf{S} \quad (\text{Stokes Theorem}) \quad (B.11)$$

$$\oiint_S \bar{A} \cdot d\mathbf{S} = \iiint_V (\nabla \cdot \bar{A}) dV \quad (\text{Divergence Theorem}) \quad (B.12)$$



### C. Two-Dimensional Green's Functions

Because of the Maxwell's Equations are linear, surface current density  $\bar{J}$  can be written superposition of point sources. If the response of a point source is found, total surface current density can be found integrating this response over the surface. Response of a point source over is called Green's Function or Kernel Function. A homogenous Helmholtz Equation for 2D can be written as follows.

$$\nabla^2 G(\bar{r}, \bar{r}') + k^2 G(\bar{r}, \bar{r}') = -\delta(\bar{r}, \bar{r}') \quad (C.1)$$

where  $G(\bar{r}, \bar{r}')$  is the 2D Green's Functions.

The solution of Equation C.1 is Hankel function of first and second kinds of zeroth order. Assuming the time harmonic term as  $e^{j\omega t}$  resulting with the second kind of Hankel Function as,

$$G(\bar{r}, \bar{r}') = AH_0^{(2)}(k|\bar{r} - \bar{r}'|) \quad (C.2)$$

In order to find the coefficient  $A$  in 2D Green's function, we can use the small argument approximation in Equation 3.84 and integrating Equation C.2 over a small circle with radius  $c$  centered at origin as follows.

$$A \iint [\nabla \cdot \nabla + k^2] \left[ 1 - j \frac{2}{\pi} \ln\left(\frac{\gamma k R}{2}\right) \right] dS = -1 \quad (C.3)$$

By using the divergence theorem in Appendix B, the first term can be converted to line integral as follows,

$$-j \frac{2}{\pi} \int_0^{2\pi} \nabla \left[ \ln\left(\frac{\gamma k R}{2}\right) \right] R d\phi = -4j \quad (C.4)$$

And the second term is described in Equation C.5.

$$k^2 \int_0^a \left[ 1 - j \frac{2}{\pi} \ln\left(\frac{\gamma k R}{2}\right) \right] 2\pi R dR \quad (C.5)$$

As the  $a \rightarrow 0$ , first part of the C.5 goes to zero and integrating the second part resulting,

$$4jk^2 \int_0^a \left[ \ln\left(\frac{\gamma k R}{2}\right) \right] R dR = \left[ \frac{R^2}{2} \ln\left(\frac{\gamma k R}{2}\right) - \frac{R^2}{4} \right]_0^a \quad (C.6)$$

Equation C.6 goes to zero because,

$$\lim_{R \rightarrow \infty} R^2 \ln(R) = 0 \quad (C.7)$$

Consequently,

$$A = \frac{-j}{4} \quad (C.8)$$

and 2D Green's function for Helmholtz Equation in C.1 can be written as,

$$G(\bar{r}, \bar{r}') = \frac{-j}{4} H_0^{(2)}(k|\bar{r} - \bar{r}'|) \quad (C.9)$$